Measurement of Branching Ratios of D^+ and D_s^+ Hadronic Decays to Four-Body Final States Containing a K_S^0

BY

Byeong Rok Ko

A Dissertation
Submitted to the Faculty of the Graduate
School of the
Korea University
in Partial Fulfillment of the Requirements
for the Degree of
Doctor of Philosophy

Seoul, December 2001

Abstract

We have studied hadronic four-body decays of D^+ and D_s^+ mesons with a K_S^0 in the final state using data recorded during the 1996-1997 fixed-target run at Fermilab high energy photoproduction experiment FOCUS. We report a new branching ratio of $\Gamma(D^+ \to K_S^0 K^- \pi^+ \pi^+)/\Gamma(D^+ \to K_S^0 \pi^+ \pi^+ \pi^-) = 0.0768 \pm 0.0041 \pm 0.0032$. We make the first observation of three new decay modes with branching ratios of the $\Gamma(D^+ \to K_S^0 K^+ \pi^+ \pi^-)/\Gamma(D^+ \to K_S^0 \pi^+ \pi^+ \pi^-) = 0.0562 \pm 0.0039 \pm 0.0040$, $\Gamma(D^+ \to K_S^0 K^+ K^- \pi^+)/\Gamma(D^+ \to K_S^0 \pi^+ \pi^+ \pi^-) = 0.0077 \pm 0.0015 \pm 0.0009$ and $\Gamma(D_s^+ \to K_S^0 K^+ \pi^+ \pi^-)/\Gamma(D_s^+ \to K_S^0 K^- \pi^+ \pi^+) = 0.586 \pm 0.052 \pm 0.043$, where in each case the first error is statistical and the second error is systematic.

To My Parents,
SoonYoung Ko and MoonJa Lee
for Their
Endless Love and Endurance

Acknowledgements

Undoubtedly, my first thank must go to all the FOCUS collaboration for their excellent work. It was my great pleasure to collaborate with them. I greatly appreciate to my advisor, Professor JooSang Kang. Without his noble lectures of general physics, mathematical physics and quantum physics, there was no my transfer to physics from geology. While Professor JooSang Kang have taught physics to me, I have been taught high energy physics from Professor Hwanbae Park. He deserves best of this thesis and I am always thanking for his cares for me. Dr. Peter H. Garbincius, Dr. Daniele Pedrini, Dr. Erik Gottschalk, Dr. Brian O'Reilly and Professor Kihyeon Cho were my paper committees. They scrutinized my paper many times and gave endless suggestions, comments and encouragements during almost two years. I must express my greatful thanks to them. Special thanks go to Professor Kihyeon Cho who was chair man of committees. He accepted all my complaints and prompted me positively always. Without his patience, I must have given up paper publishing. Mini-Monte Carlo from Peter, correction for split sample systematics from Daniele and endless comments and interests from excellent Irish, it is beyond my ability to arrange all their invaluable help. Many discussions with Dr. Soon Yung Jun and Dr. HyangKyu Park were essential to my analysis. My thanks have to go to them definitely. I also thanks to Professor John P. Cumalat and Dr. Harry W. K. Cheung for their good comments and caring for Korea University group. I am being indebted to Korea Group in FOCUS, Kyoung-Beom Lee, YeonSei Chung and Jungwon Kwak for their many help and co-work. With a big help from my friends, I could finish my graduate school course. Actually, nobody can express their parents's love. Neither can I. I would like to dedicate this thesis to them.

Contents

List of Figures

List of Tables

Chapter 1

Introduction

1.1 Elementary Particles and Interactions

The ultimate goal of particle physics is to understand the fundamental particles which compose the matter and also the fundamental interactions between them which make the matter behave the way they do. Currently prevalent description of fundamental particles and their interactions is the **Standard Model** though it requires a large number of free parameters and does not unify all the interactions within its framework.[1] In the Standard Model, the matter is made of 12 point-like elementary particles which are grouped into two categories, 6 **quarks** and 6 **leptons**. They are shown in Table 1.1 along with their properties. Each elementary particle has its counter part, anti-particle, which has equal but opposite sign of quantum numbers. Both quarks and leptons have spin $\frac{1}{2}$ and they are called **fermions**.[2] The six quarks are all massive, have fractional electric charge and are further characterized by a **color charge**, which has three different values, red, green and blue.[3] Quarks can not be isolated by themselves in nature, but are forced to combine into more complex structures called **hadrons**, which are color neutrals. Hadrons can be made of a quark and an anti-quark ($q\bar{q}$) called by **meson**, or of three quarks or three anti-quarks (qqq or $\bar{q}\bar{q}\bar{q}$) called by **baryon**. Mesons have integer spins, while baryons have half-integer spins. The three leptons e, μ, τ

[1] Masses of 6 quarks, 3 leptons, W and Z; 4 CKM parameters; the electromagnetic coupling constant α; the scale of the strong force $\Lambda_{\rm QCD}$; and the mass of Higgs particle.

[2] **Fermion** is a particle having a half-integer spin and **Boson** having an integer spin.

[3] **Color** has no relation to the real color in our daily life.

Quark	Charge ($\|e\|$)	Mass (GeV/c^2)	Lepton	Charge ($\|e\|$)	Mass (MeV/c^2)
u	$+\frac{2}{3}$	0.001∼0.005	e	-1	0.51
d	$-\frac{1}{3}$	0.003∼0.009	ν_e	0	< 0.000003
c	$+\frac{2}{3}$	1.15∼1.35	μ	-1	105.66
s	$-\frac{1}{3}$	0.075∼0.170	ν_μ	0	< 0.19
t	$+\frac{2}{3}$	174.3±5.1	τ	-1	1777.03
b	$-\frac{1}{3}$	4.0∼4.4	ν_τ	0	< 18.2

Table 1.1: Quarks and Leptons [1].

Interaction	Gauge Boson	Spin	Charge ($\|e\|$)	Mass (GeV/c^2)
Gravity	Graviton	2	0	0
Weak	$W^\pm$	1	± 1	80.4
	Z^0	1	0	91.2
Electromagnetic	Photon (γ)	1	0	0
Strong	Gluon (g)	1	0	0

Table 1.2: Fundamental interactions [1].

have unit electric charge and are massive, while the neutrinos ν_e, ν_μ, ν_τ have zero electric charge and are known to be had very small masses if they do have any. No color charge exists for leptons in Standard Model. Quarks and leptons interact by the exchange of various fundamental boson quanta. It is generally believed that there are four interactions: **gravitational**, **electromagnetic**, **weak** and **strong**. Table 1.2 lists the interactions and the related exchange particles known as **gauge bosons**. The gravitational interaction between particles with mass is responsible for the binding of matter on a planetary and universal scale, but it has negligible effects on high energy physics phenomena since it is too weak to give effects in the present energy scale. The weak interaction acting on all quarks and leptons can be noticed if the much faster strong and electromagnetic interactions are inhibited by conservation laws and it is demonstrated by some of the spontaneous transformation of particles into others with lower mass. Particles with electric charge interact through the electromagnetic force, which binds atoms and molecules together. To-

day, the electromagnetic interaction of particles are explained with the theory of Quantum ElectroDynamics (**QED**), which is a quantum gauge theory based on U(1) local gauge symmetry. The last interaction is the strong interaction between particles with color charge and is responsible for the confinement of quarks inside hadrons and the binding of hadrons in nucleus on larger scale. The theory that describes the strong interaction is known as Quantum ChromoDynamics (**QCD**) which is described by an SU(3) local symmetry. Equipped with the **Higgs Mechanism** [2], Weinberg [3] and Salam [4] proposed a gauge theory unifying the weak and electromagnetic interaction into one **electroweak** interaction in 1967-1968. The electroweak theory is based on the local gauge symmetry SU(2)×U(1). In the electroweak theory, the quarks and leptons are described as left handed weak-isospin doublets and right handed weak-isospin singlets under the SU(2) group:

Leptons

$$\begin{pmatrix}\nu_e\\ e\end{pmatrix}_{\rm L}, \quad \begin{pmatrix}\nu_\mu\\ \mu\end{pmatrix}_{\rm L}, \quad \begin{pmatrix}\nu_\tau\\ \tau\end{pmatrix}_{\rm L}$$
$$e_{\rm R}, \quad \mu_{\rm R}, \quad \tau_{\rm R}$$

Quarks

$$\begin{pmatrix}u\\ d'\end{pmatrix}_{\rm L}, \quad \begin{pmatrix}c\\ s'\end{pmatrix}_{\rm L}, \quad \begin{pmatrix}t\\ b'\end{pmatrix}_{\rm L}$$
$$u_{\rm R}, \quad c_{\rm R}, \quad t_{\rm R}, \quad d'_{\rm R}, \quad s'_{\rm R}, \quad b'_{\rm R}$$

The electroweak eigenstates of quarks (d', s', b') are linear combinations of the mass eigenstate of quarks (d, s, b), which enter the QCD Lagrangian.[4] This relation can be represented by means of the 3×3 matrix called as the Cabibbo-Kobayashi-Maskawa (CKM) matrix, $\mathbb{V}_{\rm CKM}$ [5]:

$$\begin{pmatrix}d'\\ s'\\ b'\end{pmatrix} = \begin{pmatrix}V_{ud} & V_{us} & V_{ub}\\ V_{cd} & V_{cs} & V_{cb}\\ V_{td} & V_{ts} & V_{tb}\end{pmatrix}\begin{pmatrix}d\\ s\\ b\end{pmatrix} = \mathbb{V}_{\rm CKM}\begin{pmatrix}d\\ s\\ b\end{pmatrix} \tag{1.1}$$

[4]This is just a convention; it could as well be formulated in the (u, c, t) sector or in both by redefining the phases of the quark fields

Requiring the unitarity of the CKM matrix, it can be described by four independent parameters θ_1, θ_2, θ_3 and δ:

$$\mathbb{V}_{\rm CKM} = \begin{pmatrix} c_1 & -c_3 s_1 & -s_1 s_3 \\ c_2 s_1 & c_1 c_2 c_3 - s_2 s_3 e^{i\delta} & c_1 c_2 c_3 + c_3 s_2 e^{i\delta} \\ s_1 s_2 & c_1 c_3 s_2 + c_2 s_3 e^{i\delta} & c_1 s_2 s_3 - c_2 c_3 e^{i\delta} \end{pmatrix} \tag{1.2}$$

where $c_i = \cos\theta_i$ and $s_i = \sin\theta_i$ for $i = 1, 2, 3$. Three θ_i are the mixing angles and δ implies a violation of CP invariance by the electroweak interaction within the framework of Standard Model. Finally the electroweak interactions can be described by the Lagrangian [6]:

$$\begin{aligned} -\mathcal{L}_{\rm int} &= e J^{\mu}_{\rm em} A_{\mu} \\ &+ \frac{g}{\sqrt{2}}(J^{+\mu}_{\rm L} W^{+}_{\mu} + J^{-\mu}_{\rm L} W^{-}_{\mu}) \\ &+ g_Z J^{\mu}_{Z} Z_{\mu}, \end{aligned} \tag{1.3}$$

where

$$\begin{aligned} J^{\mu}_{\rm em} &= \bar{\psi}\gamma^{\mu} Q \psi, \\ J^{\pm\mu}_{\rm L} &= \sqrt{2}\bar{\psi}\gamma^{\mu} T^{\pm}_{\rm L} \psi, \\ J^{\mu}_{Z} &= \bar{\psi}\gamma^{\mu}[T_{3\rm L} - \sin^2\theta_{\rm W} Q]\psi, \\ g &= \frac{e}{\sin\theta_{\rm W}}, \\ g_Z &= \frac{e}{\sin\theta_{\rm W}\cos\theta_{\rm W}}, \\ Q &= T_3 + \frac{Y}{2}, \\ T_i &= \frac{1}{2}\tau_i. \end{aligned} \tag{1.4}$$

First line of Eq. 1.4 represents the electromagnetic current, second one is flavor changing charged weak current and third is neutral weak current, where Q is the charge operator, Y is **weak hypercharge**, τ_i are the Pauli matrices and $\theta_{\rm W}$ is the electroweak mixing angle.

1.2 Charm Physics

The existence of the fourth quark was first suggested by Bjorken and Glashow [7] in 1964 to lead to a more symmetrical situation between quarks and leptons. In

1970, Glashow, Iliopoulos and Maiani proposed introduction of a new quark, the *charm quark* c, to solve the problem of the experimental nonexistence of strangeness changing neutral weak current which could otherwise occur if only up, down and strange quarks existed [8]. For example, the decay, shown in Fig. 1.1 $K^+ \to \pi^+ l\bar{l}$, where l is a lepton can be mediated by the strangeness changing elementary transition $\bar{s} \to \bar{d}l\bar{l}$ with a rate in excess of what was observed by now [9]. The existence of this new quark allows a cancellation of the flavor changing term in neutral weak current in the tree level diagram.[5] This method of suppressing the unwanted strangeness-changing currents is called the **GIM mechanism** and this new fourth quark was assigned the flavor of charm with charge of $+\frac{2}{3}|e|$. In November 1974, the J/ψ particle was detected simultaneously at Brookhaven and at SLAC [10]. J/ψ, a narrow resonance with a mass of about 3.1 GeV/c^2 was interpreted as a $c\bar{c}$ bound state. This hypothesis was confirmed with the discovery of *open* charm particles, the D^0 and D^+ mesons in 1976 [11].

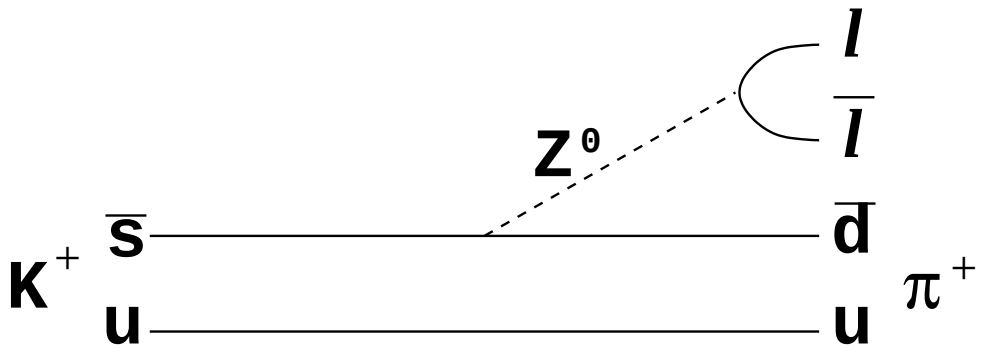

Figure 1.1: The tree level strangeness changing neutral current diagram.

1.2.1 Charm Photoproduction

Carlson [12] first suggested the possibility of charm photoproduction and Gailard [13] developed methodology based on the vector meson dominance model [14] and the naive quark model. By the late 1970's, the perturbative QCD approach was applied

[5]For example, it was shown that the mass of c could not exceed several GeV; otherwise the magnitude of the second-order neutral strangeness-changing currents would become too large. To set the GIM proposal in historical perspective it should be remembered that when it was offered there was no evidence for the charmed quark, nor had it even been proven that non-Abelian gauge theories were renormalizable so that it made sense to discuss perturbation theory for them.

to charm photoproduction mechanism. It has been known as **Photon-Gluon-Fusion** (PGF). Jones [15] has calculated the cross section of the PGF process. The two leading-order diagrams for this process are shown in Fig. 1.2.

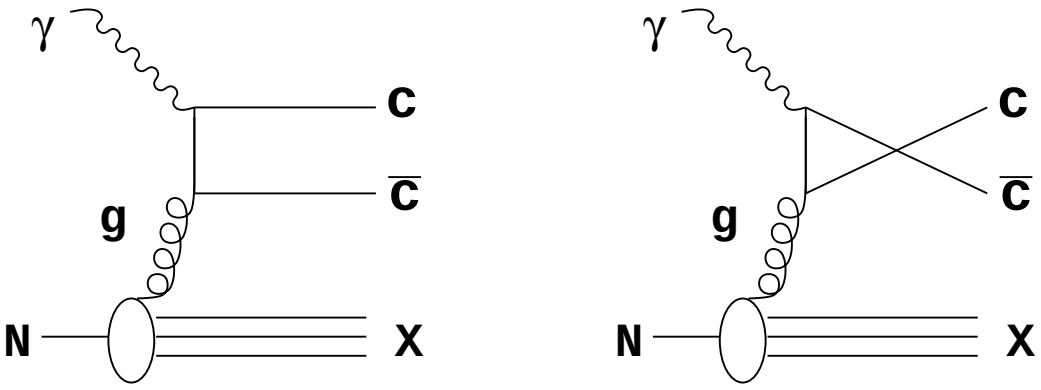

Figure 1.2: The leading order photon-gluon fusion diagrams.

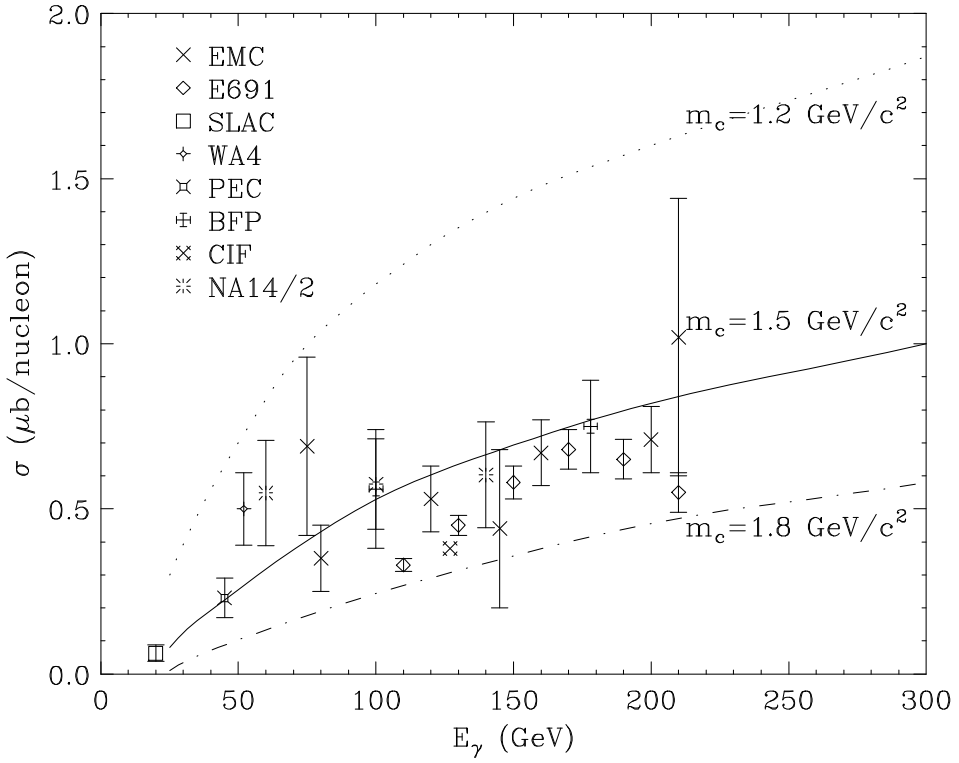

Figure 1.3: Total charm photoproduction cross section measurements.

In this model, $c\bar{c}$ pairs are produced from the interaction of photons with gluons from the target nucleon. The PGF model predicts a total charm cross section to rise gradually at high energy. The cross section measurement from several experiments shown in Fig. 1.3 indicates an apparent trend towards higher cross section at higher photon energies. After $c\bar{c}$ pair is produced, it undergoes fragmentation process to form the charm quark hadrons which are observed in the detectors. The fragmentation process is shown in Fig. 1.4. It involves the quarks composing the nucleus in addition to the quark pairs materialized from the vacuum since the $c\bar{c}$ pair is not color neutral in which retain the color of the exchanged gluon. Non-charm quark hadrons may be produced at the primary interaction point as a by-product. The fragmentation model predicts an excess of charmed baryons over anti-charmed baryons and consequently, an excess of anti-charmed meson over charmed mesons. It is due to the fact that the c quark coupling to light di-quarks is favored over the $\bar{c}$ quark coupling to anti-quark pairs which have to be created from the vacuum.

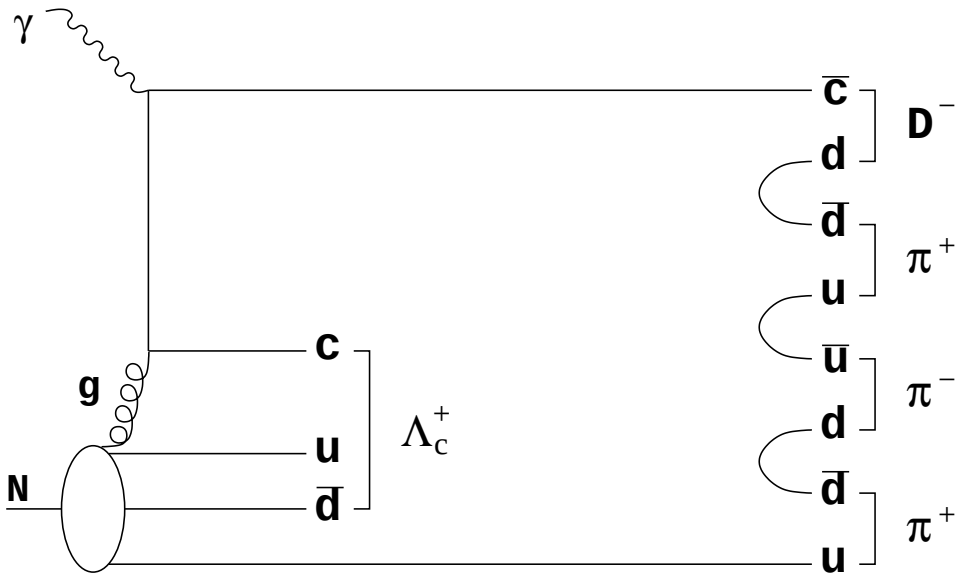

Figure 1.4: Schematic diagram of a fragmental process leading to associate production of a charmed baryon and an anti-charmed meson.

1.2.2 Charmed Mesons

Nearly all mesons are known to be bound states of a quark q and an anti-quark $\bar{q}'$ (the flavors of q and q' could be same). Given spin-$\frac{1}{2}$ for quarks and anti-quarks, we expect both spin triplet ($\uparrow\uparrow$) states of $S = 1$, called the **vector mesons**, and spin singlet ($\uparrow\downarrow$) states of $S = 0$, referred to as the **pseudoscalar mesons**. The total spin J of the composite meson is the vector sum of the spin S and the relative orbital angular momentum L between q and $\bar{q}'$. The 16 possible $q\bar{q}'$ combinations containing u, d, s and c quarks group themselves into the simultaneous eigenstates of three quantum numbers by invoking SU(4) flavor symmetry for the u, d, s and c quarks. The three quantum numbers are the isospin z-component (I_z), the charm quantum number (C) and the hypercharge (Y). Fig 1.5 exhibits two 16-plets for the ground state pseudoscalar and vector mesons. Each 16 meson is placed at the position specified by its three quantum numbers. The open charmed mesons are located in the first levels ($C = -1$) and the third levels ($C = +1$). The light mesons occupy the second levels, to which the $c\bar{c}$ bound states are added. The neutral mesons at the center of the levels are mixtures of $u\bar{u}$, $d\bar{d}$, $s\bar{s}$ and $c\bar{c}$ states. The lowest mass states of D mesons (D^0, D^+ and D_s^+) decay by the weak interactions only.

1.2.3 Charmed Baryons

All the established baryons appear to be three-quarks (qqq) bound states. In analogy with mesons, the flavor SU(4) decomposition of 64 possible qqq combinations of baryons containing u, d, s and c quarks leads to the four SU(4) multiplets. Each SU(4) multiplet has its own flavor symmetry. Unlike mesons, however, not all the SU(4) multiplets do not exist in nature. There should be additional requirements for baryons. Since the quarks are fermions, the state function for any baryon must be anti-symmetric under interchange of any two equal mass quarks (u, d and s quarks in the limit of SU(3) flavor symmetry). The state function of baryons is the products of the spatial part, the spin part, the flavor component and the color term. Given that the color wave function is always anti-symmetric, the product of spin and flavor wave functions is symmetric. Only two out of the four SU(4) multiplets combined with a particular spin symmetry form the required symmetric spin-flavor ground states. Fig. 1.6 shows the spin-$\frac{1}{2}$ and spin-$\frac{3}{2}$ ground state baryons in the

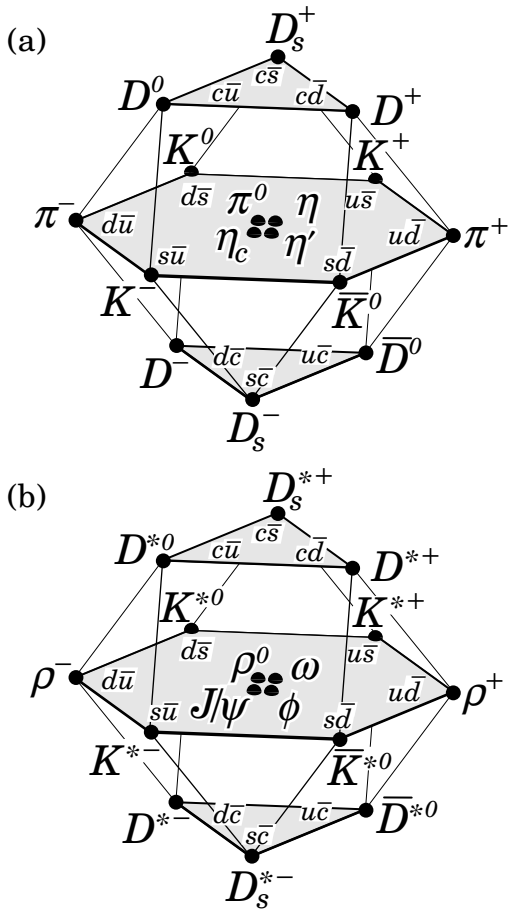

Figure 1.5: SU(4) 16-plets for the (a) pseudoscalar and (b) vector mesons made of u, d, s and c quarks.

two SU(4) multiplets. All the particles in a given SU(4) multiplet have the same spin and parity. The only known charmed baryons each contain one charm quark and thus belong to the second levels of the SU(4) classification.

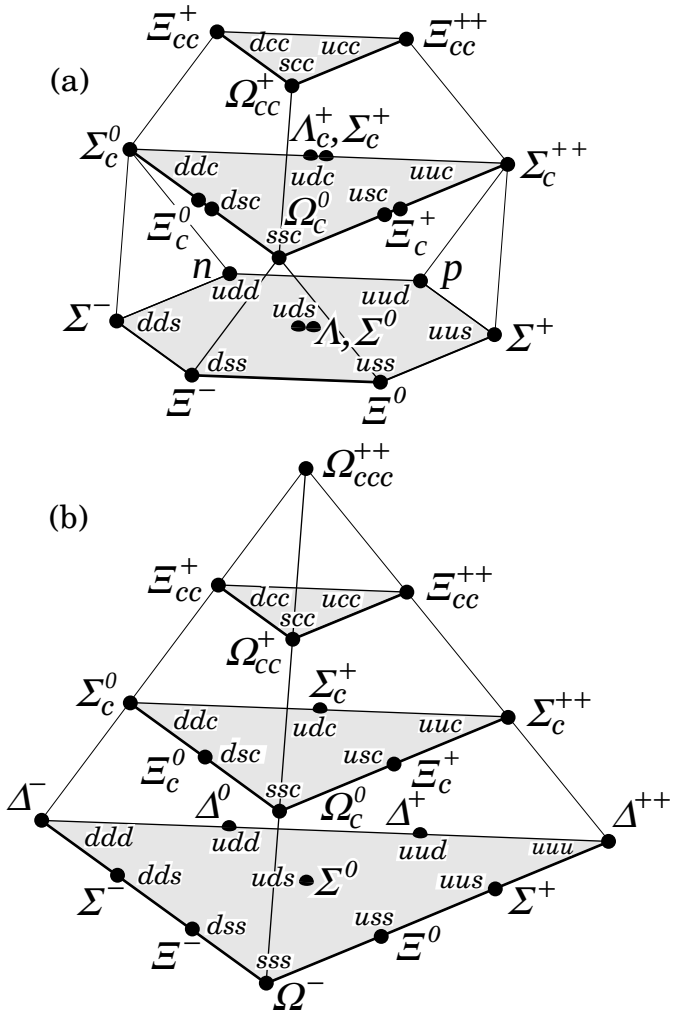

Figure 1.6: SU(4) 20 plets for the (a) spin-$\frac{1}{2}$ and (b) spin-$\frac{3}{2}$ baryons made of *u, d, s* and *c* quarks.

1.2.4 Charm Weak Decays

Weak Decay Mechanism of Charmed Hadrons In the limit where $s_2 = s_3 = 0$ in Eq. 1.2, the CKM matrix becomes:

$$\begin{pmatrix} \cos\theta_{\rm C} & -\sin\theta_{\rm C} \\ \sin\theta_{\rm C} & \cos\theta_{\rm C} \end{pmatrix}$$

which is called the **Cabibbo matrix** with only a single real parameter, Cabibbo mixing angle $\theta_{\rm C} \simeq 13^\circ$. The coupling constant associated with a quark electroweak vertex $Q \to qW^\pm$ is proportional to the CKM matrix element V_{Qq}, and thereby the transition rate is proportional to $|V_{Qq}|^2$. Since the diagonal elements of the matrix, V_{ud}, V_{cs} and V_{tb}, are close to 1, the most probable weak transitions between quarks are $t \to b$, $c \to s$, and $u \to d$. The off-diagonal elements are much smaller, therefore the corresponding transition $t \to s$, $b \to c$, $c \to d$ and $s \to u$ are much less likely to occur. As a consequence, hadrons containing b or s have a longer lifetime than would be predicted from the pure phase space considerations. On the other hand, the remaining two elements, V_{ub} and V_{td}, are close to zero, making the transitions $t \to d$ and $b \to u$ extremely unlikely. In the context of a four quark model, we expect $c \to s$ and $u \to d$ transitions ($\propto \cos^2\theta_{\rm C}$) to dominate over $s \to u$ and $c \to d$ transition ($\propto \sin^2\theta_{\rm C}$). The former is said to be **Cabibbo favored** and the latter **Cabibbo suppressed**. A weak decay which is Cabibbo-suppressed at both vertices is said to be **doubly Cabibbo suppressed** (see Fig. 1.7). The simplest decay mechanism of charmed hadrons would be the spectator model [13]. In this model charm quarks decay into lighter quarks by emitting a W boson and the remaining constituents of the hadron are assumed to be spectators and do not affect the process. The spectator diagram, as shown in Fig. 1.8 (a) and (b) for charmed mesons and (e) for charmed baryons, are believed to play a dominant role in most decays of charmed particles. In the external spectator mechanism, the decay rate into any $q'\bar{q}''$ pair is favored by a factor of three over the decay rate into a $l\bar{\nu}_l$ pair due to three color degrees of freedom. Since the color degree of freedom of the coupling quarks must match, the internal spectator decay rate is suppressed by a factor of three with respect to the external spectator. The final state for an internal spectator decay is always purely hadronic. In the exchange diagram for charmed mesons, shown in Fig. 1.8 (c), the decay rate is helicity-suppressed, while for charmed baryons, shown in Fig. 1.8 (f), helicity suppression

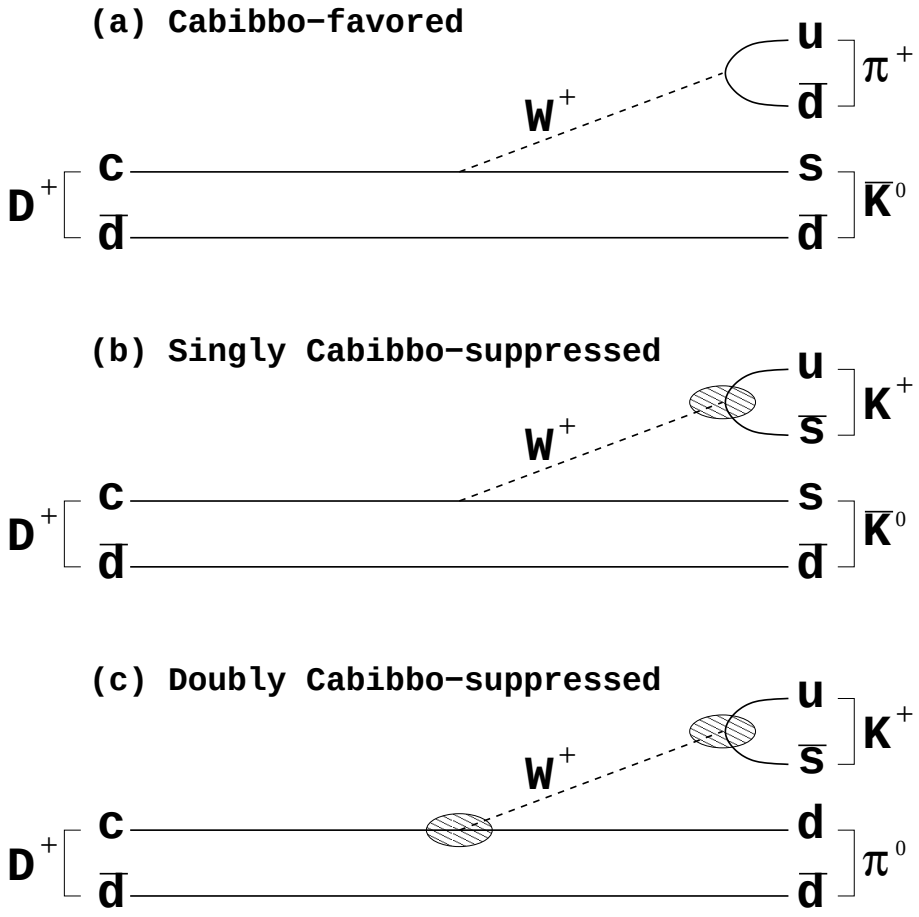

Figure 1.7: Decay diagrams for (a) $D^+ \to \overline{K}^0\pi^+$, (b) $D^+ \to \overline{K}^0K^+$, and (c) $D^+ \to K^+\pi^0$. Cabibbo-suppressed vertices are indicated by a hatched ellipse.

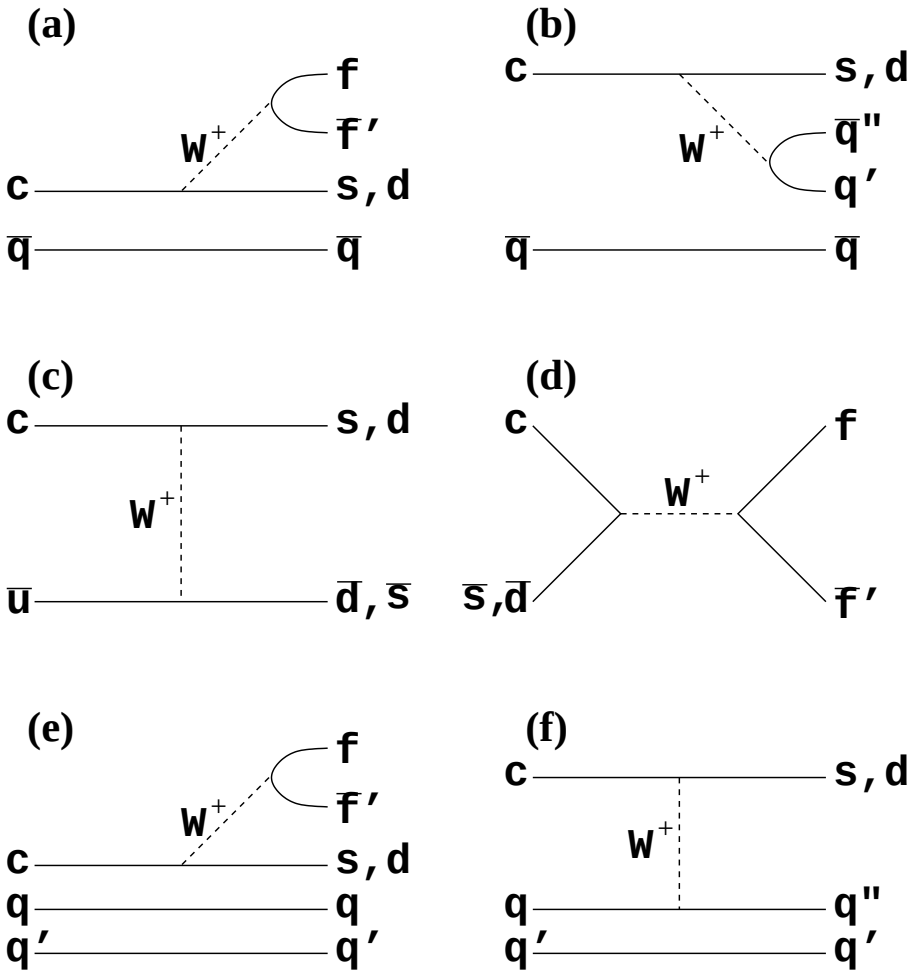

Figure 1.8: Tree level decay processes of charmed hadrons: (a) External spectator, (b) Internal spectator, (c) W-exchange and (d) Annihilation of charmed mesons. (e) Spectator and (f) W-exchange of charmed baryons.

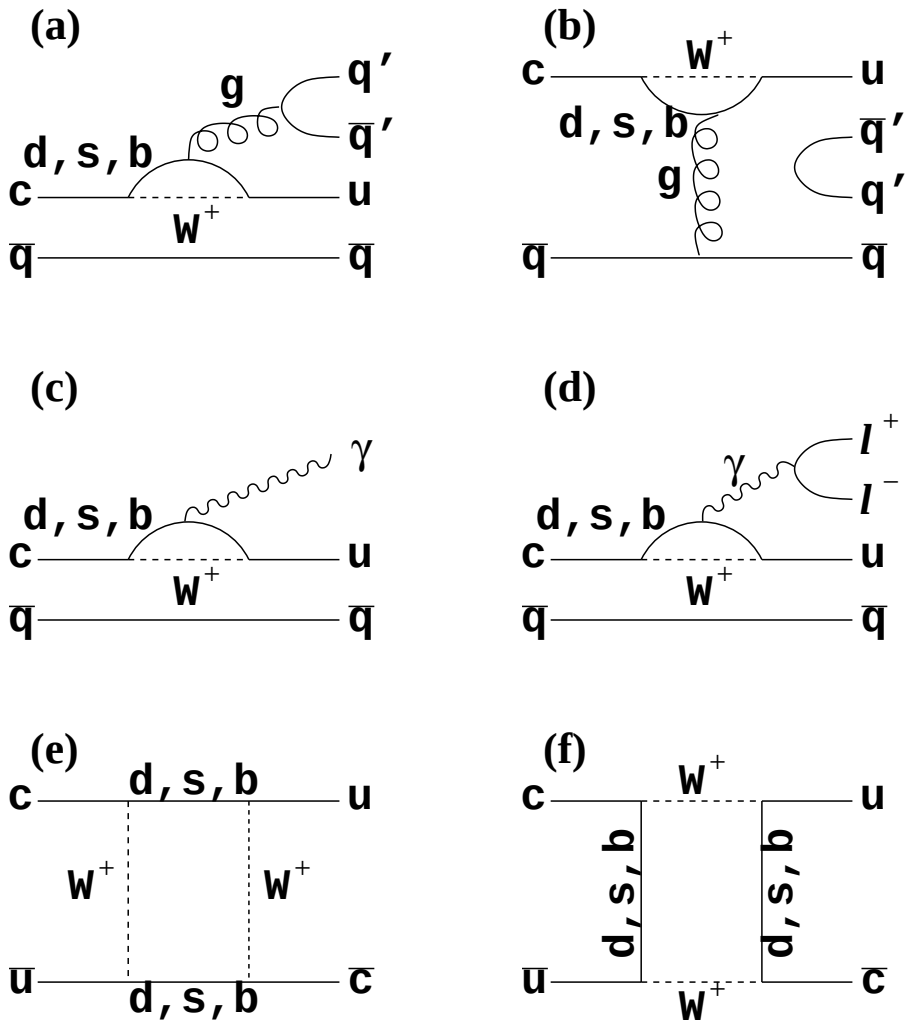

Figure 1.9: Higher order decay processes of charmed mesons: (a) and (b) Gluonic penguin, (c) and (d) Electromagnetic penguin, (e) and (f) Mixing diagrams.

is avoided by the presence of the additional light quark.[6] Therefore exchange diagrams may in principle contribute significantly to the total decay rate in case of charmed baryons besides spectator diagram. The final state of the exchange diagram is always hadronic. The annihilation diagram is also helicity suppressed and decays into a lepton-neutrino pair (purely leptonic decay) or a quark-anti-quark pair (hadronic decay). The hadronic modes are again favored by the color degrees of freedom with respect to the leptonic modes. No annihilation diagram is possible for baryons. Other more exotic possible decay mechanism are the penguin diagrams and the mixing diagrams shown in Fig. 1.9. In the loop diagrams, the heavier virtual quark produces the larger effects. In a charm decay, the heaviest possible virtual quark produced is the b quark, and the amplitude of the process is proportional to $|V_{cb}| \cdot |V_{bu}|$, which is very small. These exotic diagrams are not expected to be significant for charm quark decays.

Lifetime of Charm Quark From the universality of weak interactions, the lifetime of the charm quark can be deduced from the muon lifetime:

$$\tau_c \approx \frac{1}{5} \tau_\mu \left(\frac{m_\mu}{m_c}\right)^5 \approx 0.7 \times 10^{-12} \text{ s} \tag{1.5}$$

where τ_μ and m_μ are the lifetime and the mass of the muon, m_c is the charm quark mass. The factor, 1/5, accounts for the two leptons (electron and muon) and three quark colors which the charm quark can decay into. This naive formula (the spectator model) gives a good order of magnitude estimate for the charmed hadron lifetimes. However, it does not to explain the experimentally observed large lifetime differences among the various charmed hadron species as shown in

[6] In weak decays proceeding through the exchange or annihilation diagram, angular momentum conservation forces the two outcoming fermions to have the same helicity, both left-handed or both right-handed. Since in the Standard Model leptons are preferentially left-handed and anti-leptons are preferentially right-handed, one of the two daughters is forced in the wrong helicity state. As a result the decay is suppressed. The suppression is larger for smaller mass leptons, since in the limit of zero mass the lepton is expected to be rigorously left-handed and anti-lepton must be right-handed. This is the reason why the decay $\pi^- \to \mu^- \bar{\nu}_\mu$ has a branching ratio which is 10^4 times bigger than that of the decay $\pi^- \to e^- \bar{\nu}_e$, although the latter would be favored by phase space.

Fig. 1.10.[7] Clearly, the simple spectator picture alone is unable to explain charm decays. Addition of a non-spectator process, W-exchange and annihilation, into the decay rates may be included in the lifetime difference between the charmed mesons and baryons. But the addition of the W-exchange process does not explain the large difference between the D^+ and D^0, the annihilation process does not account for the large difference between D^+ and D_s^+ since the W-exchange and the annihilation process are strongly suppressed relative to the spectator process in the D^0 and D_s^+ decay rate.

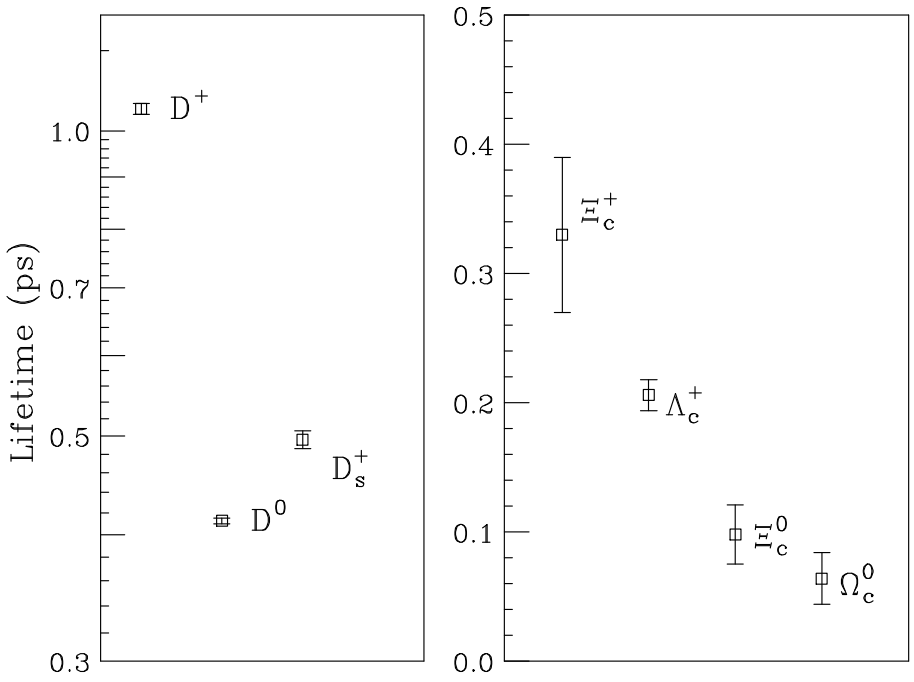

Figure 1.10: Lifetimes of weakly decaying charmed hadrons [1].

The relation:

$$\frac{\Gamma(D^0 \rightarrow e^+ X)}{\Gamma(D^+ \rightarrow e^+ X)} = 1.00 \pm 0.12 \text{ [1]} \tag{1.6}$$

reveals that the semi-leptonic decay rates of the D^0 and D^+ are nearly equal. Thus the difference in decay rates must be in the hadronic sector (the fully leptonic

[7] Recently, there are new measurements for Ξ_c^+ lifetime [16]. They report considerably longer lifetime of Ξ_c^+ comparing with current PDG value [1].

decays are suppressed and may be neglected). One explanation [17] on the D^0 and D^+ width difference lies in considering two possible spectator diagrams for D^+ decay shown in Fig. 1.11. Only in the case of D^+, and not D^0 or D_s^+, both diagrams give the same final state quark pairings. Therefore, these diagrams may interfere and a negative interference could explain a net decrease in the D^+ hadronic width. Since the D^0 and D_s^+ do not have the possibility for this kind of interference, this explanation seems quite plausible. But, we are not able to say what makes difference between D^0 and D_s^+ lifetime yet. More precise charm data is needed to extract the size of the matrix elements to control the weight of W-exchange and W-annihilation in D decays.

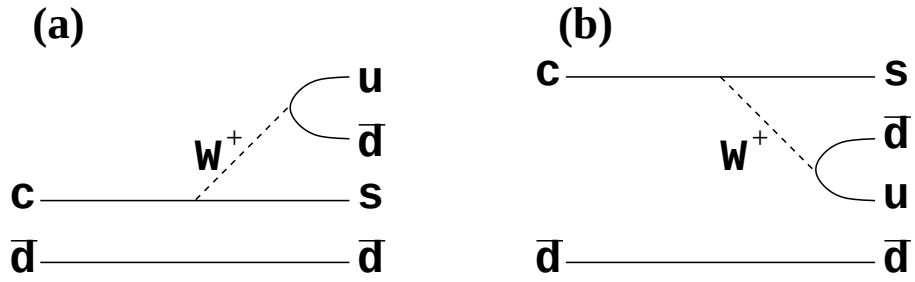

Figure 1.11: (a) Spectator and (b) color suppressed internal spectator diagrams for D^+ decay.

1.2.5 Hadronic Charm Decay

Perhaps the least understood aspect of charm decay physics is hadronic charm decay. Primarily this is due to the complexities of the strong interaction which makes it extremely difficult to calculate reliably the rate and properties of such decays. One of the clearest demonstrations underlying complexity of this subject is the rough order of magnitude difference among the lifetimes of the seven long-lived, singly charmed hadrons shown in Fig. 1.10. Significant disparity in lifetimes primarily reflects differences in the hadronic decay width as referred in previous section. There are several ways of studying hadronic charm decays. The most inclusive way is through the precise measurements of charm particle lifetime. One can study the partial decay widths of charm mesons into specific two-body hadronic final states. Much of the rich phenomenology of hadronic decays can be explained and organized by a model which we call **factorization**. The factorization model

concerns so-called spectator decays. Factorization models predict the partial decay widths of two-body decays of charmed mesons in the absence of Final State Interactions (**FSI**). It describes subsequent strong re-scattering of the final state mesons after they are produced from initial charm decay. Final state interaction effects become apparent in the interference between the various isospin amplitudes which contribute to different charged variants of a given final state which would have to have relatively real phases in the absence of such interactions. The factorization framework, in which hadronic charm decays have been traditionally analyzed, begins with an effective Hamiltonian such as given by Eq. 1.7 describing CKM allowed decays:

$$\mathcal{H} \;=\; \frac{G_f}{\sqrt{2}} V_{cs}^* V_{ud} \left(\frac{C_+ + C_-}{2} (\bar{u}d)(\bar{s}c) \;+\; \frac{C_+ - C_-}{2} (\bar{s}d)(\bar{u}c) \right) \tag{1.7}$$

The Hamiltonian of Eq. 1.7 incorporates QCD correction to the underlying weak decay process utilizing renormalization group methods. The coefficients $C_\pm$ are called **Willson coefficients**. In the absence of QCD corrections, $C_+ = C_-$ and one recovers single weak process corresponding to the familiar external W spectator diagram where a $c \to sW^+ \to su\bar{d}$. The Wilson coefficients depend on the scale of the QCD coupling constants. When taken at the charm quark mass, the Wilson coefficients have the values given by Eq. 1.8.

$$\frac{C_+(M_Q) + C_-(M_Q)}{2} \approx 1.25, \; \frac{C_+(M_Q) - C_-(M_Q)}{2} \approx -0.49 \text{ [18]} \tag{1.8}$$

Bauer, Stech and Wirbel (**BSW**) [19] combined these ideas into an explicit model applied two-body and quasi-two-body hadronic charmed meson decay. In the BSW model, the two terms of Eq. 1.7 are organized into an effective charged current and effective neutral current between the parent and daughter hadrons. The first term with an amplitude, $a_1 \approx (C_+ + C_-)/2$ (with a small color correction) describes the familiar spectator process. The effective neutral current process with an amplitude $a_2 \approx (C_+ - C_-)/2$ will decrease as $M_Q \to \infty$ gives rise to additional effects which are important in charm. If a given hadronic charm decay can only proceed through the effective charged current interaction, it is classified as a Class 1 process. Class 2 processes only proceed through the effective neutral current interactions. Class 3 processes have contribution from both interactions. In the process, $D^0 \to K^-\pi^+$, one has one neutral parent and two charged daughters and hence this must be a

Class 1 process.[8] In the Class 2 process, $D^0 \to \overline{K}^0\pi^0$, one has neutral parent D^0 decaying into two neutral daughters. The CKM allowed decays of the D^+ such as $D^+ \to \overline{K}^0\pi^+$ (shown in Fig. 1.11), are Class 3 processes.

Watson's Theorem According to the Watson's theorem, the weak amplitudes predicted in factorization models such as BSW must all be relatively real. However, the final state hadrons can continue to interact via long range strong interactions and acquire complex phases. These FSI can be accommodated by multiplying the bare (weak) amplitudes by the square root of a complex, unitary S matrix describing the strong rescattering. To illustrate the effects of FSI consider the isospin classification of three amplitudes related to $D \to \pi\pi$ decay:

$$\begin{aligned} A(D^0 \to \pi^+\pi^-) &= \frac{1}{\sqrt{3}}(\sqrt{2}a_0 + a_2), \\ A(D^0 \to \pi^0\pi^0) &= \frac{1}{\sqrt{3}}(-a_0 + \sqrt{2}a_2), \\ A(D^+ \to \pi^0\pi^+) &= \sqrt{\frac{3}{2}}a_2 \end{aligned} \tag{1.9}$$

The measured a_0 and a_2 amplitudes will acquire complex phases through the FSI S matrix as indicated in Eq. 1.10.

$$\begin{pmatrix} a_0 \\ a_2 \end{pmatrix} = \begin{pmatrix} \eta e^{2i\delta_0} & i\sqrt{1-\eta^2}e^{i(\delta_0+\delta_2)} \\ i\sqrt{1-\eta^2}e^{i(\delta_0+\delta_2)} & \eta e^{2i\delta_2} \end{pmatrix}^{\frac{1}{2}} \begin{pmatrix} a_0 \\ a_2 \end{pmatrix}_{\text{bare}} \tag{1.10}$$

Since QCD respects isospin symmetry, there should be no mixing between a_0 and a_2 which means the elasticity parameter in Eq. 1.10 should be $\eta = 1$. Even a purely elastic FSI can change the total width of charm decays into a particular final state by changing the value of $\cos(\delta_2 - \delta_0)$ when converting $A(D^0 \to \pi^+\pi^-)$ into $\Gamma(D^0 \to \pi^+\pi^-)$ via Eq. 1.11.

$$\Gamma(D^0 \to \pi^+\pi^-) = \frac{2}{3}|a_0|^2 + \frac{1}{3}|a_2|^2 + \frac{2\sqrt{2}}{3}|a_0||a_2|\cos(\delta_2 - \delta_0) \tag{1.11}$$

[8] In the BSW model the amplitude for this decay is written as $a_1 G_f 2^{-1/2} < \pi^+|(\bar{u}d)|0 >< K^-|(\bar{s}c|D^0 >= a_1 G_f 2^{-1/2}(-if_\pi P_\pi) \times f_+(m_\pi^2)$. The coupling of the π^+ with respect to the virtual W^+ involves the same current as the leptonic decay $\pi^+ \to l^+\nu$ which is proportional to the pion lepton decay constant. The CKM allowed current is the same current involved in the semileptonic decay process $D^0 \to K^- l^+ \nu$ which is described by the form factor $f_+(q^2)$.

The unexpectedly large branching ratio for the decay $\Gamma(D^0 \to K^+K^-)/\Gamma(D^0 \to \pi^+\pi^-)$ [20] provided an early example of the possible role of FSI affecting branching ratios. Although both processes are Cabibbo suppressed by the same amount and $D^0 \to \pi^+\pi^-$ is favored with a larger phase space, $D^0 \to K^+K^-$ occurs at roughly twice the rate as $D^0 \to \pi^+\pi^-$. In the context of the BSW model, both decays are Class 1 processes, since no effective neutral currents are possible between the parent and either daughter, and the BSW model makes the prediction $\Gamma(D^0 \to K^+K^-)/\Gamma(D^0 \to \pi^+\pi^-) \approx 1.4$ independent of the value of a_2/a_1. Conventional wisdom has it that discrepancy between the data and the BSW prediction is due to FSI changing the phase of interfering dipion or dikaon isospin amplitudes. A more direct way of observing the effects of final state interactions is to measure the widths into various isospin related channels and extract a_0, a_2 and $\cos(\delta_2 - \delta_0)$ by solving Eq. 1.11 and the two similar equations. Table 1.3 taken from the Annual Review article [21] summarizes the results of such isospin analyses for many two body and quasi-two body charm decays. Table 1.3 shows that more often that not, a considerable phase shift is observed between the two isospin amplitudes. Watson's theorem tells us that phase shifts between interfering isospin amplitudes where $\sin(\delta_{I'} - \delta_I) \neq 0$ cannot arise from the weak processes alone and thus constitutes direct evidence for FSI.

Mode	Amplitude ratio	$\delta = \delta_I - \delta_{I'}$
$K\pi$	$\lvert A_{1/2}\rvert/\lvert A_{3/2}\rvert = 3.86 \pm 0.20$	$90^\circ \pm 6^\circ$
$K^*\pi$	$\lvert A_{1/2}\rvert/\lvert A_{3/2}\rvert = 5.59 \pm 0.35$	$104^\circ \pm 14^\circ$
$K\rho$	$\lvert A_{1/2}\rvert/\lvert A_{3/2}\rvert = 3.59 \pm 0.75$	$0^\circ \pm 28^\circ$
$K^*\rho$	$\lvert A_{1/2}\rvert/\lvert A_{3/2}\rvert = 5.12 \pm 1.97$	$33^\circ \pm 57^\circ$
KK	$\lvert A_1\rvert/\lvert A_0\rvert = 0.57 \pm 0.06$	$51^\circ \pm 9^\circ$
$\pi\pi$	$\lvert A_2\rvert/\lvert A_0\rvert = 0.63 \pm 0.13$	$80^\circ \pm 10^\circ$

Table 1.3: Isospin amplitude ratios and phase shifts for two body charm decays.

Hadronic decay to Four-body Final states To improve our understanding of D hadronic decays two main issues need to be addressed by experiments. First, experiments should extend their measurements to cover the branching ratios of

all the hadronic decay modes to complete the picture and, at the end, enforce a unitarity constraint. Second, experiments must analyze the resonant substructures of the multi-body decays in order to understand the role of final state interactions in sharing the rates among different isospin connected modes. In the present thesis we address the former issue by providing two world's first measurements of branching ratios for D^+ and one for D_s^+. In the D_s^+ case, this new measurement is particularly important since a major portion of the D_s^+ hadronic width is still unmeasured.[9] In particular, this measurement accounts for about 2.5% of the total width, more than one half that of the $\phi\pi^+$ mode ($\Gamma(D_s^+ \to \phi\pi^+) = (3.6 \pm 0.9)\%$ [1]), which has been often used as D_s^+ normalization mode. In addition, we report on inclusive branching ratios of D^+ and D_s^+ decays into four-body final states involving a K_S^0. We measure the D^+ decay rates into $K_S^0 K^- \pi^+ \pi^+$, $K_S^0 K^+ \pi^+ \pi^-$ and $K_S^0 K^+ K^- \pi^+$ relative to $K_S^0 \pi^+ \pi^+ \pi^-$ and the decay rate of $D_s^+ \to K_S^0 K^+ \pi^+ \pi^-$ relative to $D_s^+ \to K_S^0 K^- \pi^+ \pi^+$.[10] Among these final states only the $K_S^0 K^- \pi^+ \pi^+$ final state has been observed previously [23].

[9] Poor evidence for this mode, $D_s^+ \to K_S^0 K^+ \pi^+ \pi^-$, was already reported [22] and was dropped from the PDG review.

[10] Throughout this thesis the charge conjugate state is implied.

Chapter 2

The FOCUS Apparatus

FOCUS (**Ph**otoproduction **O**f **C**harm with an **U**pgraded **S**pectrometer) is a fixed-target charm photoproduction experiment located at the Wideband area of Fermilab proton line. The use of a photon beam, instead of hadron beam as in other fixed-target experiments, has merits and demerits. The ratio of charm interactions to non-charm hadronic interactions is of more advantage in photoproduction ($\sim$ 0.6%) than in hadroproduction ($\sim$ 0.08%). This compensates disadvantage the absolute heavy quark production cross section is actually lower for a photon beam ($\sim$ 1 μb) than for a hadron beam (20 $\sim$ 30 μb). Also, photoproduced events have a lower average multiplicity than in hadroproduction, where the incident particle has an internal structure and is fragmented in the interaction process. Consequently, photoproduced events have less combinatoric and charm background than hadroproduced events. The major source of background in photoproduction is the electromagnetic events, $\gamma \rightarrow e^+e^-$, which can be greatly suppressed by the trigger system. However, photon beams have lower intensity than hadron beams. This requires the use of thicker production targets, which results in abundant Multiple Coulomb Scattering (MCS) and increased secondary interactions. Besides, it is more difficult to determine the location of primary interactions since traceless photons are not to be seeds for guide of the search for the primary interaction points and due to the lower track multiplicity per event. The experimental apparatus of the FOCUS consists of the beamline producing the high energy photons impinged on the experimental target, and the spectrometer detecting the products of the photon-nucleon interactions.

2.1 The Beamline

2.1.1 The Proton Beam

Protons are accelerated to a final energy of 800 GeV through a series of successive steps from the Fermilab accelerator complex. First, the ionized hydrogen gas, H^- is fed into a Cockcroft-Walton electrostatic accelerator and accelerated to 0.75 MeV. Next, the ion beam is then sent into the LINAC (LINear ACcelerator) and accelerated further to 400 MeV over a distance of approximately 146 m. The LINAC is composed of a series of metallic cavities to which a rapidly oscillating potential difference is applied, so that the electric field created between the cavities is repeatedly reversed in direction. The ions are then increasingly accelerated every time they traverse the space between two cavities, while they travel undisturbed within each cavity. On exiting the LINAC, the ions pass through a carbon foil, which strips off the electrons to leave only the protons. The protons then steer into the booster ring, a rapid cycling synchrotron of 500 m in circumference which accelerates them to 8 GeV. Inside the booster, the protons move in a circular path within a continuously increasing magnetic field, while being accelerated by a radio frequency electric field at each revolution. The protons are then injected into the main ring. The main ring has 1000 m radius and uses 774 dipole magnets to bend the beam and 240 quadrupole magnets to refocus it. The main ring is used to accelerate the protons to 150 GeV. Finally, the protons are injected into the Tevatron. The Tevatron is in the same tunnel as the main ring but uses the 1000 superconducting magnets of which magnetic field is about 4 tesla and operate at the temperature of 4.7 K and raised 5×10^{12} protons per bunch to energy of 800 GeV during 1996 and 1997 fixed-target run periods. The 800 GeV proton beam is extracted from the Tevatron and transported to the switchyard where the proton beam is distributed into three experimental areas which are the meson, neutrino and proton beamlines. The proton beam is divided into three lines: East, Center and West. The proton east beam is directed towards the Wideband photon beamline, where the FOCUS experimental hall is located (see Fig. 2.1).

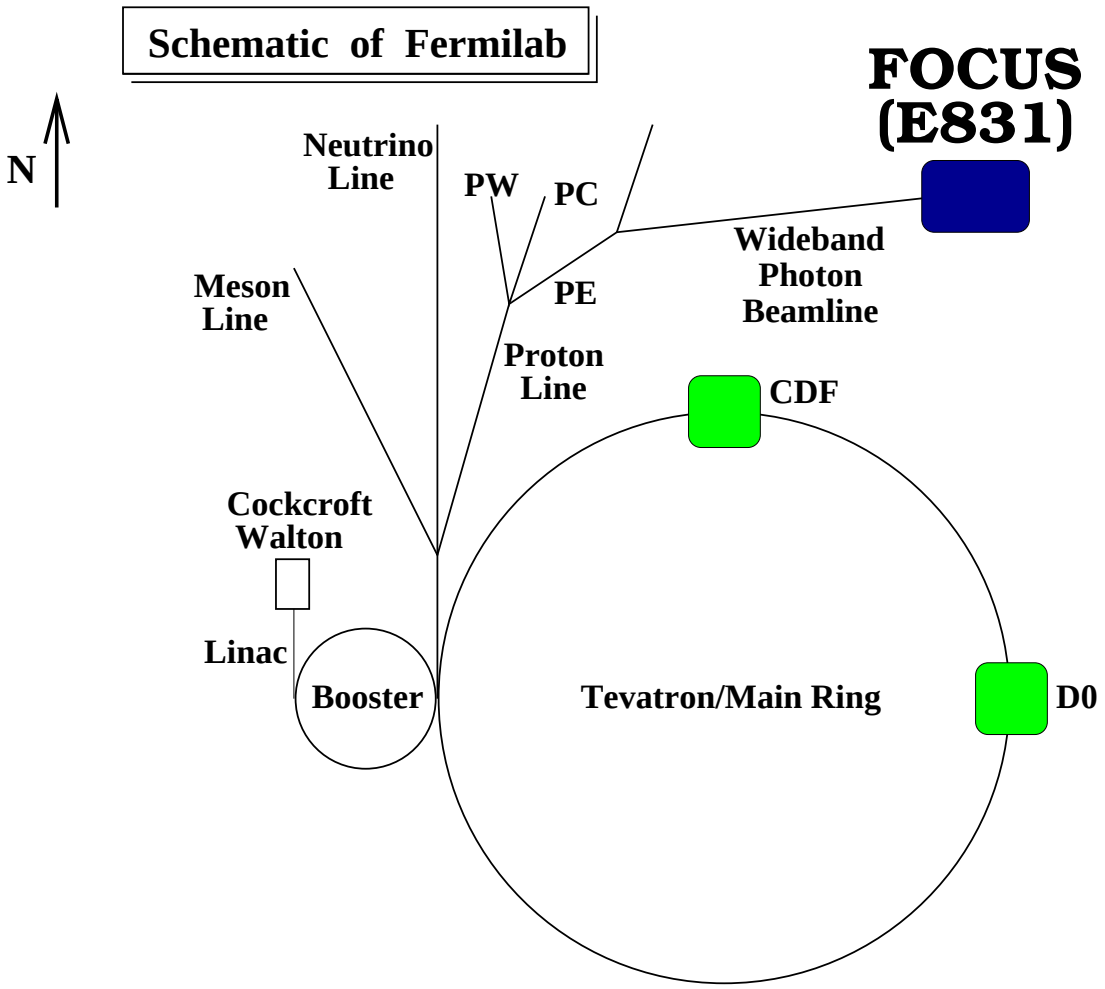

Figure 2.1: Schematic of the fixed-target experiment complex at Fermilab.

2.1.2 The Photon Beam

Creating pure high energy photon beam for the FOCUS experiment is a multi-step process. A schematic of the Wideband photon beamline is shown in Fig. 2.2. First, incident 800 GeV protons from the Tevatron impinge on a liquid deuterium target. Charged particles, mainly non-interacting protons and pions, are swept away from the beam direction by sweep magnets and deposited into a charged particle dump. The neutral products from the proton-deuterium interactions consist mainly of photons, neutrons, K_L^0's and Λ^0's. This neutral beam is allowed to pass through a small beam hole in the dump and impacts a lead converter. This converter is a sheet of lead of 0.6 radiation length thick. The thickness of the radiator is chosen such that a large fraction of the photon component of the neutral beam is converted into e^+e^- pairs, whereas it is likely that the neutral hadrons pass through it. After the electrons and positrons are focused with quadrupole magnets, the charged beam portion is bent around a dump which absorbs the uninteracting neutral particles. The electrons and positrons are transported by separate beamlines towards the experimental apparatus. The beam transport system is designed to select the electrons and positrons with momentum of 300 GeV/c with $\pm 15\%$ of range. The two beams are recombined into a single beam by the momentum recombining dipoles. The combined beam is refocused and impacts the radiator which is a sheet of lead with 0.2 radiation length thick where it produces the bremsstrahlung photons aimed at the experimental target. After the beam passes through the radiator, sweeping magnets remove the remaining charged portion of the beam which is directed into the Recoil Electron Shower Hodoscope detector (RESH) and recoil POsitron Shower Hodoscope detector (POSH) described in next section. The final photon beam has very little hadronic contamination. The 300 GeV electron and positron beams produce photons with mean energy of about 180 GeV. Fig. 2.3 shows steps schematically used to produce the photon beam.

2.1.3 The Beam Tagging

The beam tagging system which is installed in the FOCUS beamline determines the energy of photon on event by event basis. The interacting photon is determined by measuring the electron momentum before and after the radiator and measuring the energy of any non-interacting photons which are created by multiple

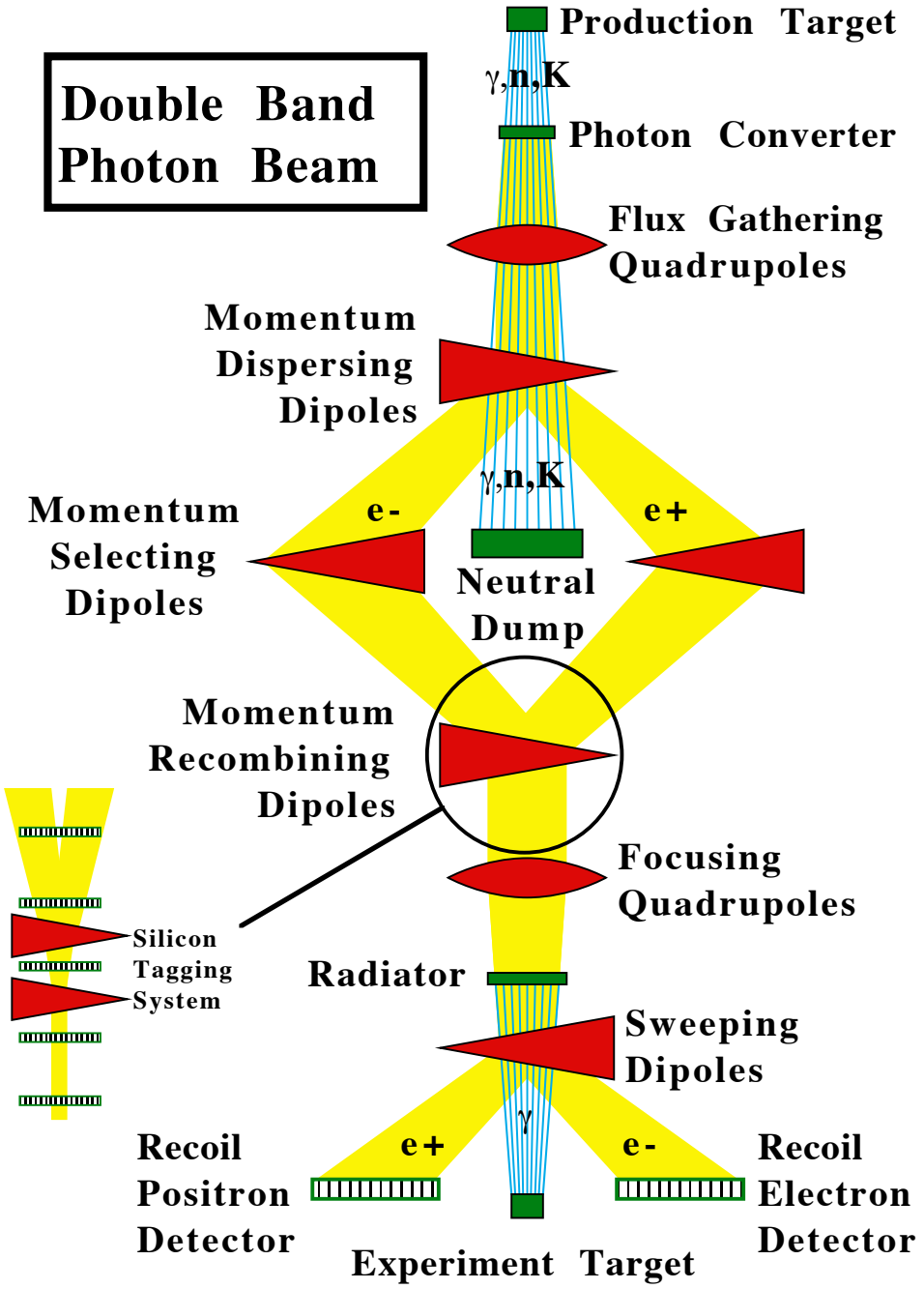

Figure 2.2: Layout of the FOCUS photon beamline. The inset is the electron beam tagging system.

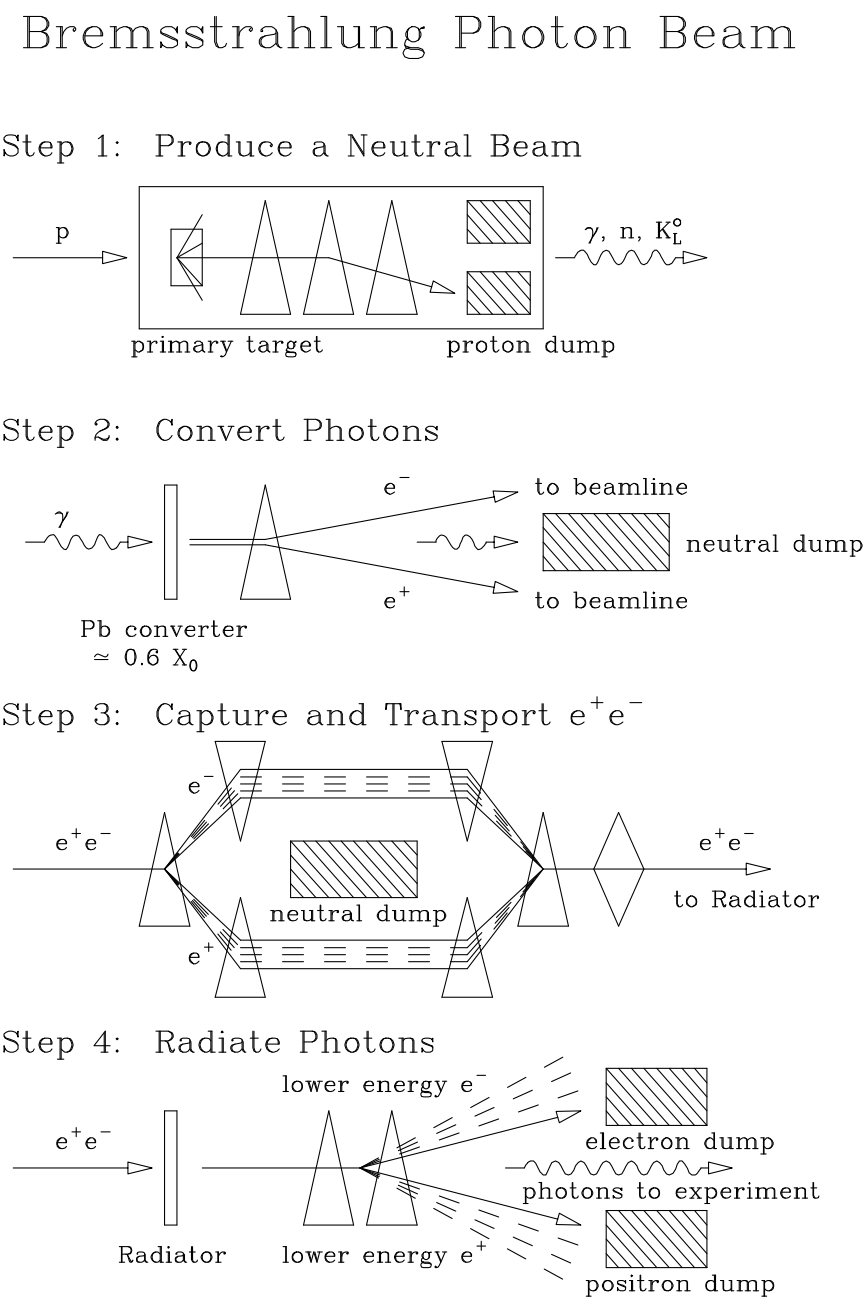

Figure 2.3: Schematics of the successive steps to produce the FOCUS photon beam.

bremsstrahlung. The tagging system has three independent detectors: the silicon microstrip tagging system, the RESH and POSH and the BGM (Beam Gamma Monitor) [24]. The silicon tagging system consists of five planes of silicon strip detector, two on either side of the momentum recombining dipoles and one positioned between the two dipole magnets. The arrangement is shown in the inset of Fig. 2.2. Each 7.7 cm $\times$ 5.7 cm silicon plane is composed of 256 silicon strips of 300 μm pitch for a total of 1,280 channels. The microstrip system accurately measures the deflection angle of the charged particle at it traverse the dipole magnets and provides a 2.2% momentum resolution. RESH and POSH each have 12 counters, labeled 0-9, 11 and 12. RESH0 and POSH0 detect electrons and positrons which do not radiate. RESH and POSH are sampling calorimeters with alternating layers of lead and Lucite. The struck counters determine the bend angle of the electron or positron and thus its energy. The final detector needed for measurement of the non-interacting photons is the Beam Gamma Monitor (BGM). The BGM has 24 alternating layers of lead and SiO_2 equivalent to 25 radiation lengths and was designed to measure the electromagnetic shower energies resulting from multiple bremsstrahlung photons created in the upstream lead radiator. With the energies determined by the above detectors, the energy of interaction photon is calculated by:

$$E_\gamma \;=\; E_{e^-} \;-\; E_{\rm RESH} \;- E_{\rm BGM} \tag{2.1}$$

where

- E_{e^-} is the energy of the electron measured by the silicon microstrip tagging system,
- $E_{\rm RESH}$ is the energy of the recoil electron after emitting a bremsstrahlung photon in the radiator,
- $E_{\rm BGM}$ is the total energy deposited in the BGM by non-interacting photons.[1]

2.2 The FOCUS Spectrometer

The FOCUS detector is a large aperture fixed-target multiparticle spectrometer which features excellent particle identification and vertexing for charged hadrons

[1] Correspondingly, $E_\gamma \;=\; E_{e^+} \;-\; E_{\rm POSH} \;- E_{\rm BGM}$.

and leptons. The layout of the spectrometer is shown in Fig. 2.4. Major detector systems are silicon microstrip detector for vertexing, multiwire proportional chamber and two dipole magnets for momentum determination and Čerenkov detector for particle identification. Also electromagnetic and hadronic calorimeters, muon detectors and numerous hodoscopes for triggering are included.

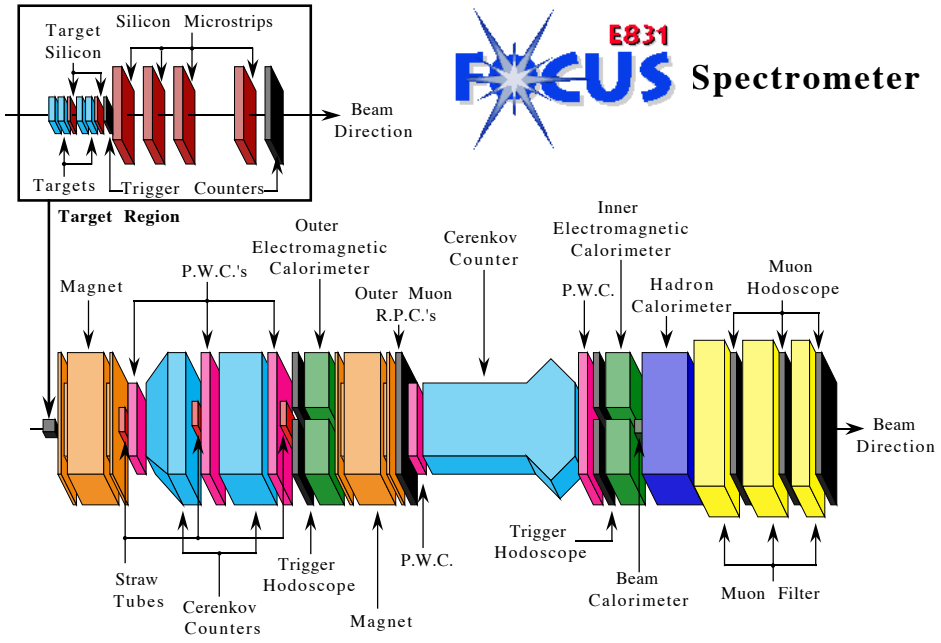

Figure 2.4: Layout of the FOCUS Spectrometer. The inset is an expanded view of the target region.

2.2.1 Coordinate Systems

There are two main coordinate systems employed in the explanation of the detector and the event reconstruction. Both have the positive Z axis oriented along the beam direction, positive X pointing to the west and positive Y vertically upward. The first system, called M2 coordinates, has the origin at the bend center of M2. The second system, called granite block coordinate, has its origin at the upstream edge of the granite block that support the SSD. The offset between the two systems is about 1240 cm. The M2 coordinate is used for analysis of MWPC data and lepton identification, while the granite block is used for analysis of SSD-based information

such as vertexing. Fig. 2.5 shows the coordinate systems and terminologies used to describe locations in the course of the experiment.

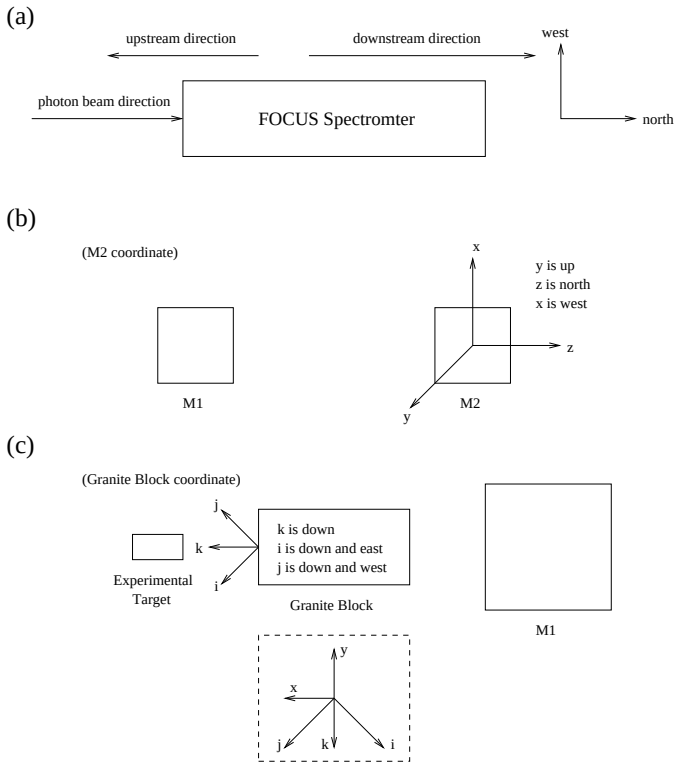

Figure 2.5: Idealized view of FOCUS coordinate systems. We are looking from y direction in all cases except the inset view of (c). (a) shows some basic terminologies, (b) represents the M2 coordinate system and (c) shows the granite block coordinate system. The inset of (c) is the relation between the M2 coordinates and the granite block coordinates. We are looking it in the z direction.

2.2.2 Experimental Target

The FOCUS experiment used segmented target configuration. This helped to increase number of decays out of target. Based on the experience from E687, cleaner charm signals were obtained when the secondary vertices are outside of the target [25]. This is because a major background to charm are events with multiple interactions which can easily fake detached vertices. For example, a non-charm

hadronic photon interaction can produce a secondary which can undergo subsequent inelastic interactions within the target. The final state will have separated vertices just like a charm event and will be hard to eliminate through a detachment cut. But they can be easily eliminated by requiring one vertex is in the gap between target segments. The target is composed of Beryllium Oxide (BeO) arranged into four separate segments with two embedded silicon strip detector. BeO has a fairly large radiation length to interaction length and a fairly high density for such a low Z material. The large radiation length for our 15% interaction length target both minimizes multiple Coulomb scattering within the target and the number of e^+e^- pairs created on each beam pulse which both confuses charm events and creates problems for the MWPC system by creating a large current draw. The relative high density allows us to use thin target segments which maximizes the number of clean charm decays which take place in the air gaps between target segments. The target layout is presented in Fig. 2.6. Each target is 6.75 mm thick and the gap between targets is 10 mm in the beam direction and 25.4 mm $\times$ 25.4 mm in area. This is the target configuration with which most of the FOCUS data was accumulated. Other configurations included a single beryllium (Be) target, a segmented Be target and a segmented BeO target without embedded silicon microstrip detectors.

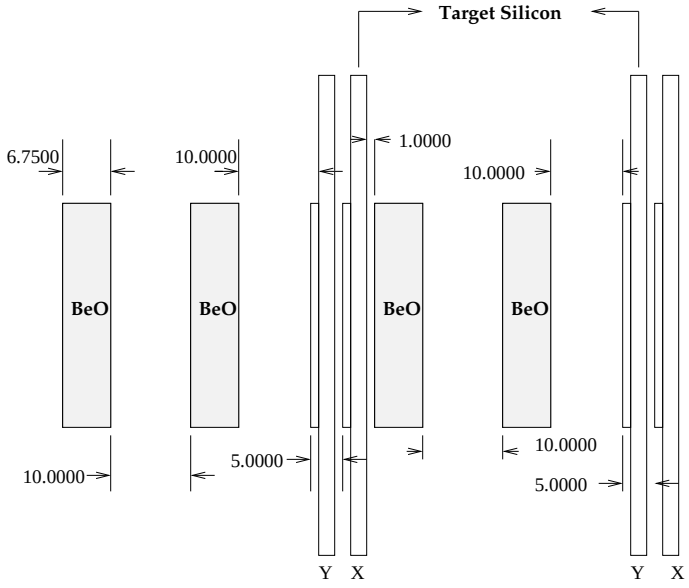

Figure 2.6: Schematic layout of the target region for the FOCUS. All units are in millimeters.

2.2.3 Silicon Microstrip Detector

There are two silicon microstrip detector systems. One system referred to as the **Target Silicon** or **TSSD** is interleaved with the target segments and the other one **SSD** is the downstream of target region. They are essential components of the experiment.

TSSD In order to increase the vertex resolution, two high resolution silicon strip detectors, shown in Fig. 2.6 and inset of Fig. 2.4 are embedded in the target region. Each station has two views oriented at $\pm 45^{\circ}$ from horizontal; each view has 1024 strips with 25 μm spacing, providing an active region about 25 mm across. This dimension is well matched to the beam size and to the extent of the target segments. Each strip is about 50 mm long, enabling an active area of about 50 mm $\times$ 25 mm per plane. Readout is accomplished with ADC (Analog to Digital Converters). The TSSD system was in place only for the 1997 run period of FOCUS which includes bulk of the data collected.

SSD The SSD is located immediately after the target in the downstream and upstream of the first magnet. The SSD consists of 12 silicon microstrip planes grouped into four stations of three planes each. The strips of one plane in each station are oriented vertically, while the strips of other two planes are situated at $\pm 45^{\circ}$ with respect to the horizontal axis (x-axis) of spectrometer. The planes within a station are separated by 5 mm. The geometrical layout of the detector is shown in Fig. 2.7 and tabulated in Table 2.1. The innermost section of each plane, covering the region where tracks pass most closely to each other, has two times better resolution than the outer section. In addition, because the station nearest the target is the most important for determination of decay vertex, it has a resolution twice as good as the others. The analog pulse height is readout for each strip. Since the charge released in an interaction with the microstrip is proportional to the incoming charge, the pulse height provides a simple estimate for the number of charged tracks involved in a series of adjacent hits. The resolution power of the SSD turns out to be about 6 μm in the transverse direction for infinite momentum tracks crossing the high resolution region.

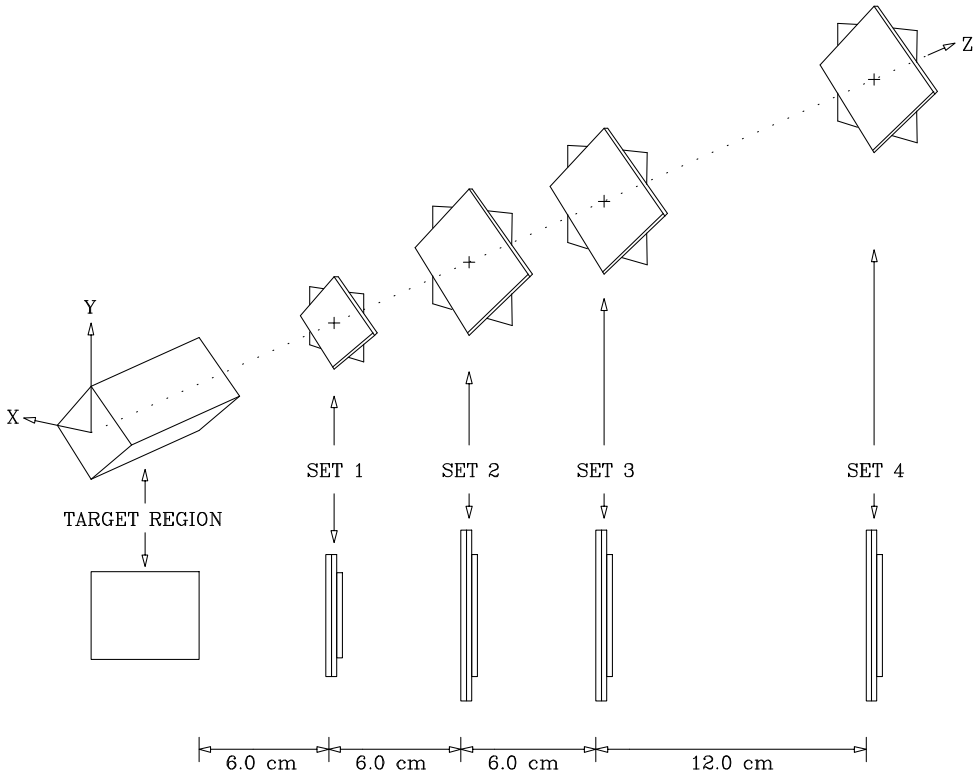

Figure 2.7: Schematic drawing of the SSD layout. Target region is shown in Fig. 2.6 in detail.

Property	Station I	Station II	Station III	Station IV
Active area (cm^2)	2.5×3.5	5×5	5×5	5×5
High resolution area (cm^2)	1.0×3.5	2×5	2×5	2×5
Pitch (High/Low Res.) (μm)	25/50	50/100	50/100	50/100
No. of channels	688×3	688×3	688×3	688×3

Table 2.1: Properties of the silicon microstrip detector

2.2.4 Analysis Magnets

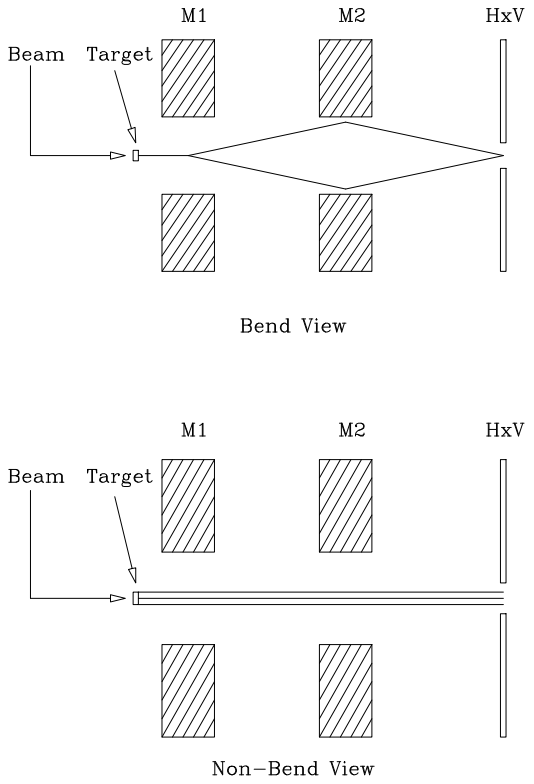

Figure 2.8: Topology of typical e^+e^- event.

Two large aperture dipole magnets are used in the momentum analysis of charged tracks. The first magnet (M1) is located just in the downstream of the SSD and operated at the current of 1,020 amperes yielding a kick of 0.4 GeV/c. The second magnet (M2) is placed in the center of the spectrometer, between the third and fourth wire chambers and operated at the current of 2,000 amperes yielding a kick of 0.836 GeV/c. The two magnets are operated with opposite directions on the transverse plane (Y-view). The aperture size for both magnet is $\pm$38 cm in X-view and $\pm$63.5 cm in Y-view. Both magnet is 1.7 m long and mass of about 245,000 kg. This particular arrangement of magnet positions and momentum kicks was determined for its unique affect on the event topology. There are many e^+e^- pairs coming from beam photon conversions in the target. Because they are produced with small transverse momentum they initially travel parallel to the beam direction (Z-direction) and have a transverse profile comparable to the beam size. The first

magnet bends the electrons and positrons in Y, creating a vertical swath. The low energy pairs hit the M1 dipole tips or the upstream face of the M2, while the remainders pass through the M2 aperture and are bent back towards the beam axis. The beam profile is reconstituted at the end of the spectrometer with some smearing due to bremsstrahlung energy loss of the particles in the spectrometer material. A schematic of this is given in Fig. 2.8. Hadronic events, by comparison, have much more angular spread and will almost have at least two particles outside the pair region in the downstream end of the spectrometer. This crucial difference between pair events and hadronic ones is exploited by the trigger, which requires two or more hits in a hodoscope located in the downstream end of spectrometer. The hodoscope, H×V, as well as the trigger is discussed in detail in Sec. 2.2.11.

2.2.5 Multiwire Proportional Chambers

Property	P0	P1	P2	P3	P4
Aperture (cm^2)	76×127	152×229	152×229	76×127	152×299
Wire spacing (mm)	2.0	3.0	3.0	2.0	3.0
No. of X-view wires	376	480	480	376	480
No. of Y-view wires	640	704	704	640	704
No. of U/V-view wires	640	768	768	640	768

Table 2.2: Properties of the five multiwire proportional chambers.

Five stations of multiwire proportional chambers (MWPC) are used to track charged particles in the main spectrometer. The first three chamber (P0, P1 and P2) are located between the two analysis magnets, M1 and M2. The other two (P3 and P4) are located in the downstream of the M2. This arrangement allows two independent momentum measurements for track leaving hits at least in tracks which are not accepted by the M2. The properties of each station are shown in Table 2.2. All five chambers consist of four planes of wires, measuring X, Y, V and U positions. X-view wires, running vertically, measure the horizontal position. The U and V wires make angles of $\pm 11.3^\circ$ with respect to the Y-view, which are designed to resolve ambiguities and provide the better momentum resolution. The arrangement of each views is shown in Fig. 2.9. The chambers P0 and P3, called Type I

stations, are identically constructed. P0 and P3 are just downstream of M1 and M2 respectively. These chambers have aperture of about (±38 cm) × (±63.5 cm) which is matched to the magnet aperture. The Type II chambers, P1, P2 and P4, have (±76 cm) × (±114.5 cm) aperture. P1 and P2 are situated between P0 and M1 and P4 is located after the last Čerenkov detector. The gas used in the MWPC systems is a gas mixture of 75% argon and 25% ethane bubbled through ethyl alcohol at 0°C.

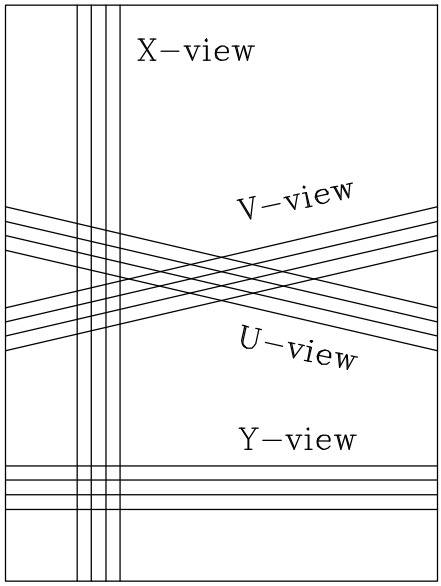

Figure 2.9: Orientation of the PWC wires (Looking downstream).

2.2.6 Straw Tube Chambers

Straw tube chamber works similarly to multiwire proportional chambers, but instead of high voltage being supplied along a plane, the high voltage is maintained on metal coated tube with a ground sense wire in the center. Because each sense wire has its own source of electric field, straw tube chambers can be operated reliably in higher rate environments. They also have the additional benefit of being more reliable since a single broken wire only impacts one channel. It was originally concerned that the FOCUS PWC system would not be able to handle the high rates present in the pair region and that the PWCs would have to be deadened in this region. To prepare for this possibility, three straw tube chambers were con-

structed to cover the pair region of each of the first three PWCs. The three straw tube chambers have similar designs with the length and number of the straws being the primary difference between chambers. P0 is smaller than P1 and P2 so the corresponding straw tube chamber is also smaller. ST0 and ST1 are placed just in front of P0 and P1 respectively, ST2 is placed just behind P2. There are three views per station, one vertical and two aligned at $\pm 11.3^\circ$ from vertical. Each view has three layers of straws. All the chambers use 5 mm diameter straws. Table 2.3 summarized their properties. Actually, the deadening the PWC system was not necessary, so the straw tubes were not needed for tracking. However, because the straw tubes are readout with TDCs (Time to Digital Converters), they can provide useful information about the timing of events, rejecting tracks which occur in other accelerator buckets.

Property	ST0	ST1	ST2
Straw length (cm)	138	241	241
No. of Vertical wires	3×10	3×10	3×10
No. of Angled wires	3×38	3×74	3×74
Total Wires	258	474	474

Table 2.3: Properties of the three straw tube chambers.

2.2.7 Čerenkov Counters

Čerenkov radiation in a medium occurs when a charged particle travels faster than speed of light in the medium:

$$\beta = \frac{p}{E} = \frac{p}{\sqrt{p^2 + m^2}} > \frac{1}{n} \tag{2.2}$$

or equivalently,

$$p > p_{\text{threshold}} = \frac{m}{\sqrt{n^2 - 1}} \tag{2.3}$$

where n is the index of refraction of the material.[2] The experiment has three threshold Čerenkov counters, referred as to C1, C2 and C3 and they were operated

[2]We use units where c=1.

at atmospheric pressure. We look for the presence or absence of light to identify a particle. For a given track momentum we are able to identify four kinds of particles, e, π, K and p. The gases in the counters have been chosen to provide wide momentum ranges over which pions can be distinguished from kaon and protons. There is also a wide range over which kaons and protons can be distinguished from each others. The characteristics of each counter are summarized in Table 2.4.

Counter	Gas	$p_{\text{threshold}}$ (GeV/c)			No. of cells
		pion	kaon	proton	
C1	58% He, 48% N_2	8.5	29.9	56.8	90
C2	N_2O	4.5	16.2	30.9	110
C3	He	17.0	61.0	116.2	100

Table 2.4: Characteristics of the Čerenkov counters.

C1 The C1 is located between P0 and P1. There are 90 cells with photomultiplier tube (PMT) readout. In the outside portion of counter, spherical mirrors were used to focus light onto each individual PMT. In the inner, high rate, portion of the detector, two planar mirrors oriented at $\pm 45^\circ$ to the beam reflect Čerenkov radiation orthogonal to the beam to where it is collected by a set of 50 PMTs. The cell geometry of C1 is shown in Fig. 2.10(a).

C2 This is located between P1 and P2. Čerenkov light is focused onto the outer 56 cells by spherical mirrors. Čerenkov light in the central region is reflected by a planar section, composed of 32 small planar mirrors. The geometry of C2 is shown in Fig. 2.10(b).

C3 The C3 is located between P3 and P4. Light from each cell is focused with a spherical mirror onto a PMT. The cell arrangement is shown in Fig. 2.10(c).

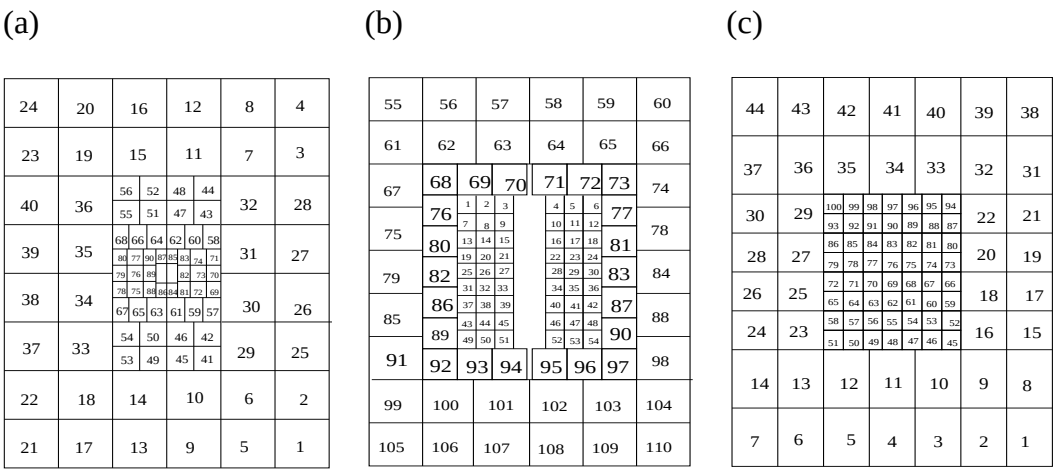

Figure 2.10: The arrangement of the light gathering cells for the three Čerenkov counters. (a) is C1: Cells 1-40 use spherical mirrors, 41-90 use planar mirrors, (b) is C2: Cells 1-54 use planar mirrors, 55-110 use spherical mirrors and (c) is C3: All cells use spherical mirrors.

The momentum ranges over which particles can be identified are shown in Table 2.5. These numbers assume a large number of emitted photons, namely it is an unrealistic assumption. Near threshold, it is often the case that only a few photons may be emitted and may avoid detection. The Čerenkov algorithm described in Sec. 3.4.1 takes this into account.

particle	momentum ranges (GeV/c)	
	5-chamber track	3-chamber track
e	0.16−17.0	0.16−8.5
π	4.5−17.0	4.5−8.5
K	16.2−56.8	16.2−29.9
p	16.2−56.8 & 61.0−116.2	16.2−56.8
e/π	17.0−61.0	8.5−29.9
$e/\pi/K$	61.0−116.2	29.9−56.8
K/p	4.5−16.2	4.5−16.2
$\pi/K/p$	0.16−4.5	0.16−4.5

Table 2.5: Particle identification momentum ranges.

2.2.8 Hadron Calorimeter

The Hadronic Calorimeter [26] (HC) is located in the downstream of the IE. It measures the energy of hadronic particles within the acceptance of M2. The HC also plays a crucial role in the first level of triggering by providing a fast sum of the hadronic energy in each event. The HC consists of 28 active scintillator planes separated by 28 planes of iron which absorb energy. The scintillating planes are divided into tiles as shown in Fig. 2.11. Scintillation light created in the tiles is collected by wave shifting fibers which are mated to clear fibers at the tile's edge. The clear fibers are routed to phototubes at the edge of the detector. The depth is 209 cm or 7.8 hadronic interaction lengths.

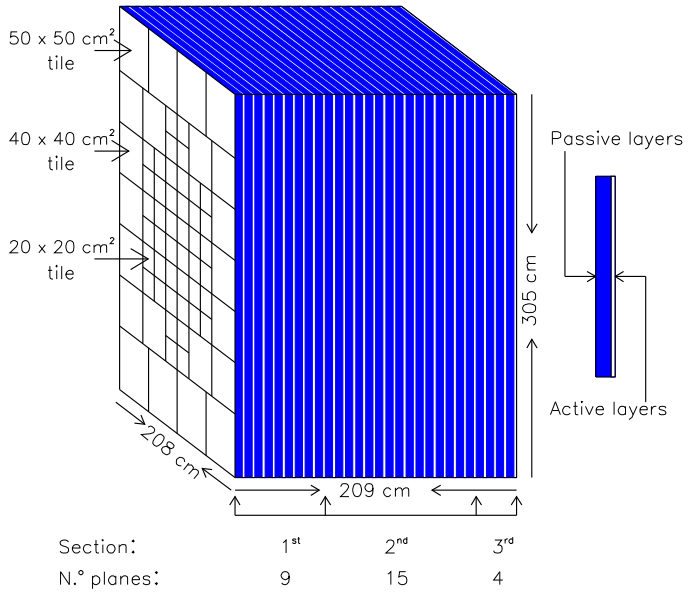

Figure 2.11: Schematic drawing of the Hadron Calorimeter.

2.2.9 Electromagnetic Calorimeters

The FOCUS spectrometer has two independent electromagnetic calorimeters. The Outer Electromagnetic (OE) calorimeter is just in front of M2 and has a rectangular gap in the middle which matches the magnet's aperture. The OE's design is that

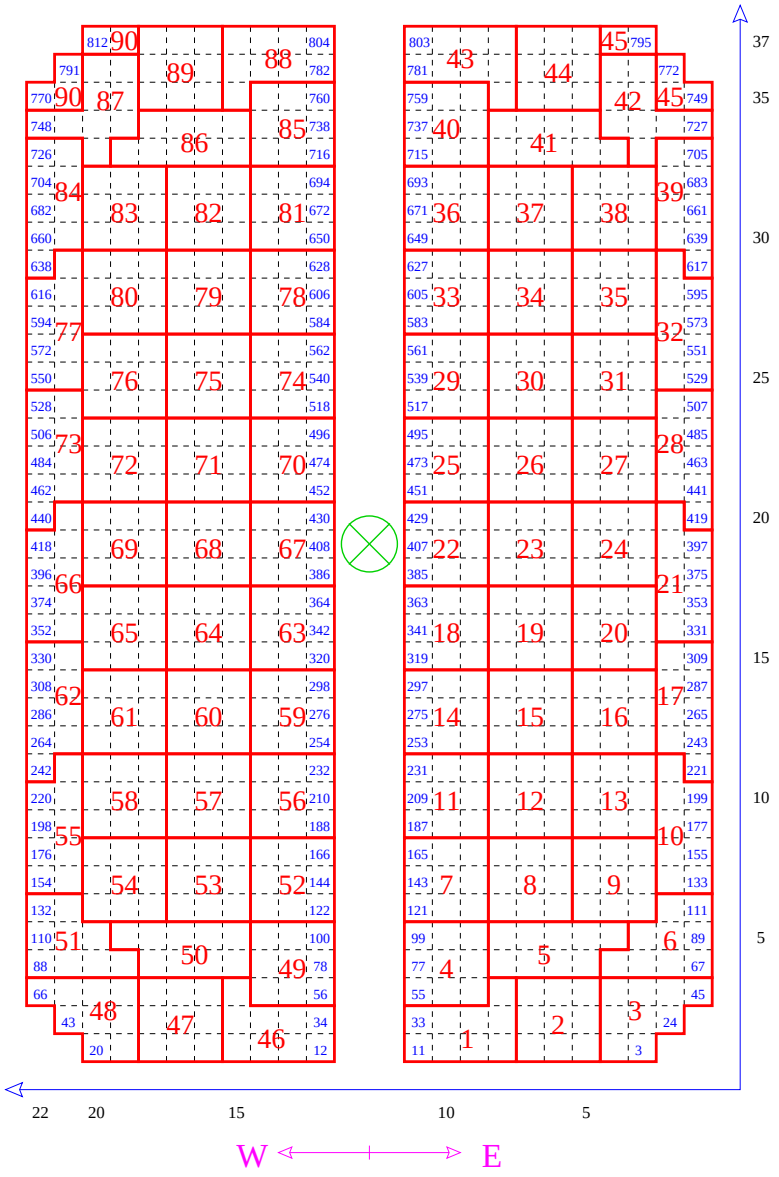

Figure 2.12: Schematic of the Inner Electromagnetic calorimeter showing block layout (dashed lines) and trigger summer groupings (heavy lines).

of a lead-aluminum-scintillator sandwich, with 10 modules of various orientations. The OE detects and measures the shower of electromagnetic particles outside of the acceptance of M2. The Inner Electromagnetic (IE) calorimeter detects and measures the energy of electromagnetic particles that are within the acceptance of M2. The IE is an array of lead glass blocks arranged in a tower geometry. Čerenkov light generated in the lead glass by the charged particles of the electromagnetic shower is collected by phototubes mated to the lead glass blocks on the downstream end of the calorimeter. The detector is divided into two halves about the y axis with a central gap of 14 cm which allows non-interacting beam photons and e^+e^- pairs to pass through. A schematic drawing of the layout of the IE is shown in Fig. 2.12. Each block has dimensions 5.8 cm $\times$ 5.8 cm $\times$ 60.2 cm. This is correspond to 18.75 radiation lengths and 2.2 proton interaction lengths. A fast energy sum is performed on groups of nine blocks for trigger.

2.2.10 Muon Detectors

The FOCUS has two muon detecting systems. The Inner Muon (IM) detection system consists of three stations of scintillating hodoscopes. Each station is proceeded by a steel block. The widths of the three steel blocks are 61 cm, 129 cm and 68 cm from upstream to downstream. The Outer Muon (OM) detection system uses resistive plate chambers to detect passing muons. The muon detectors take advantage of the facts that muons will not generate electromagnetic showers often and muons have high penetration power, to distinguish them from other charged particles, electrons and hadrons. Detectors are placed behind the OE and IE calorimeters along with additional material to ensure that all particles are filtered out except muons. The OM counters are located just downstream of the yoke of M2, and the IM counters are the very last downstream elements in the experiment.

2.2.11 Trigger

The electric logic that is required to select interesting events from the background is called the trigger. In each spill the FOCUS spectrometer typically had about 10^8 (mostly electromagnetic) interactions and triggered on about 30,000 (mostly hadronic) interactions. It is known that in high energy photoproduction interaction the hadronic interaction rate is about 1/500 of the pair productions. The e^+e^- pairs

generally are produced at a very small transverse momentum, and very low opening angle trajectories, whereas the hadronic interactions produce particles with larger transverse momentum, and wider trajectories. The hadrons also deposit larger energies in the hadronic calorimeter. Therefore the main purpose of the trigger is to select the events with wide angles and non-negligible deposited energy in the HC. The first level of the hadronic trigger is called the Master Gate (MG). The MG trigger occurs within 200 ns after interaction takes place. 160 ns is allocated for transfer of information from the spectrometer, and the remaining 40 ns is used decision making, whether the events is selected or not. If the MG accepts the events, then the readout is processed and the second level trigger evaluation begins. The second level trigger decision take 1.2 μs. If the event is accepted by the second level trigger, writing the state of the detector to the magnetic tape for off-line analysis continues, otherwise the readout electronics are reset and the process is repeated again. The electronics are reset in 1 μs.

First Level Trigger The first level trigger checks to ensure that the photon has interacted in the target and thereby charged particles has passed through the target. This is achieved by TR1 located in the upstream of the first SSD plane. The TR1 counter consists of a scintillator counter and a PMT. The TR2 counters are located downstream of the last SSD plane, and ensure that the charged particles that pass through TR1 also go through the microstrips. TR2 consists of four scintillator counters and PMTs. It is required that there are wide angle tracks in the event by using the H$\times$V array. This set if arrays are located downstream of M2, after the last PWC station. A fast trigger logic module determines if the pattern of hit is consistent with one charged particle, $(\mathrm{H}\times\mathrm{V})_1$, or more than one, $(\mathrm{H}\times\mathrm{V})_2$. The array has a central gap to let the e^+e^- pairs through without counting them. Another set of scintillator counters called OH are located in the upstream of OE to assure passage of at least one particle. There is also a gap at the center of to let the e^+e^- pairs through. The hadronic MG requirement is then;

$$\mathrm{MG1} \;=\; \mathrm{TR1}\cdot\mathrm{TR2}\cdot\{(\mathrm{H}\times\mathrm{V})_2+[(\mathrm{H}\times\mathrm{V})_1\cdot\mathrm{OH}_1]\}\cdot\mathrm{E_{HI}} \tag{2.4}$$

where $\mathrm{E_{HI}}$ ensures the energy deposited in HC by the hadrons is above a high threshold. Fig. 2.13 shows H$\times$V and OH arrays.

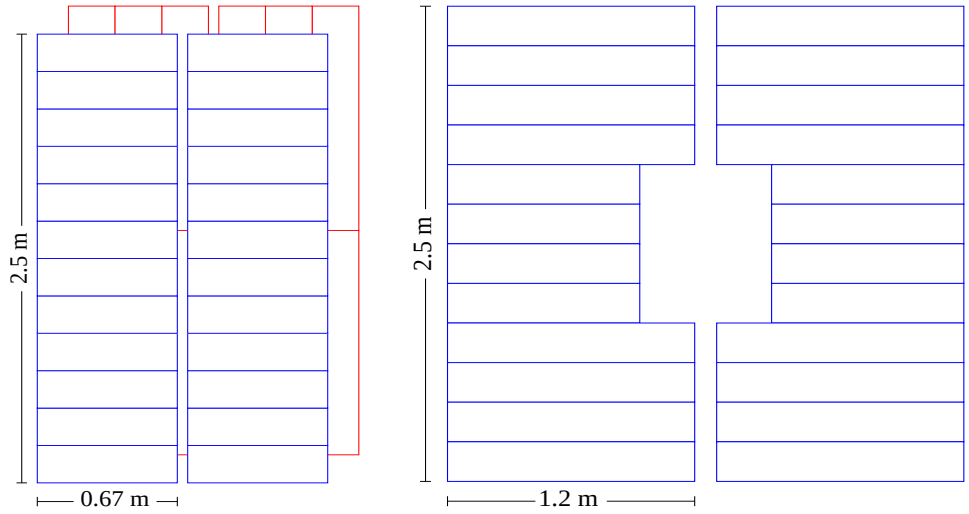

(a) H X V (b) OH

Figure 2.13: The H×V and OH hodoscope arrays.

Second Level Trigger The second level trigger requires that there is evidence of a minimum number of tracks outside the pair region. This is done by evaluating logic signals with voltage proportional to the number of hits in each plane that is derived from the PWC readout module. The information from each plane are combined, and a condition of at least three tracks outside the pair region is imposed (MULT4). The inner electromagnetic calorimeter (IE) is also used at the second level trigger. The electromagnetic energy deposited in IE is required to be over the threshold, and at least two hits above threshold in IE is required (E_{IE-2}). The hadronic second level trigger requirement is then;

$$\mathrm{TRIG1} \;=\; \mathrm{MG1} \cdot \mathrm{E_{IE-2}} \cdot \mathrm{MULT4} \tag{2.5}$$

2.2.12 Data Acquisition System

Events after passing the Second Level Trigger requirements are readout and written to tape for future analysis. Then there is 1 ms of deadtime. If the event fails the Second Level Trigger there is about 1.5 μs of deadtime as the system resets. Fig. 2.14 shows the layout of the Data AcQuisition (DAQ) system which is described in detail elsewhere [27]. Digitized information on timing, charge and hits

are collected through a direct VME interface, by an SGI Challenge L computer, which assembles the events and saves it to disk. Once a run is complete, typically about 30 minutes of data taking and 1 M triggered events, the data are written to an 8 mm tape.

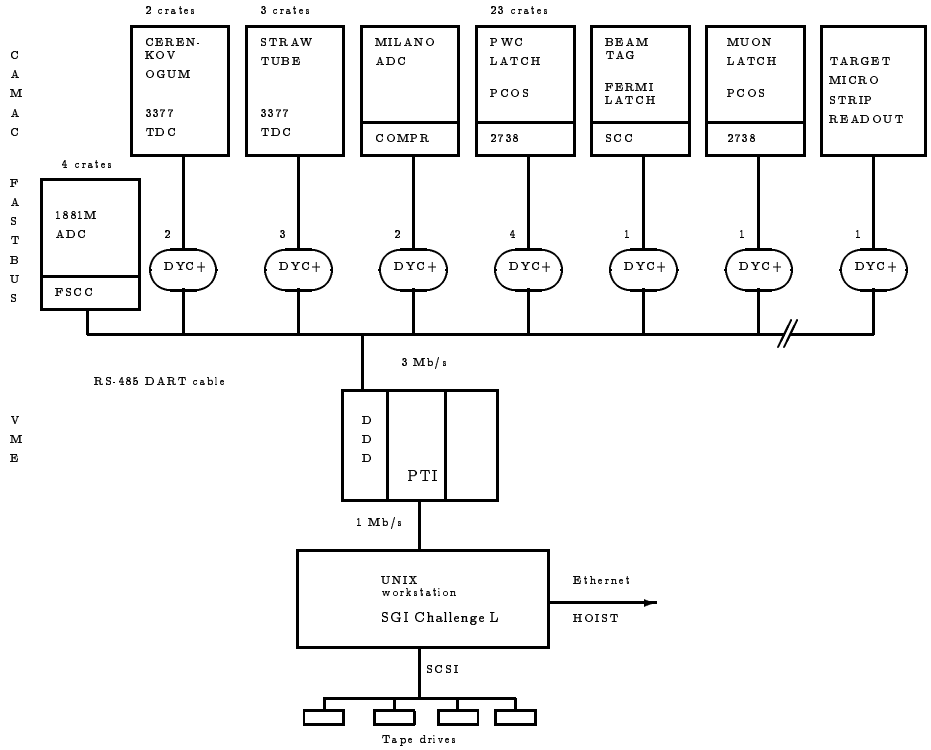

Figure 2.14: Overview of the DAQ layout.

Chapter 3

Data Reconstruction

The events taken during the run are usually stored in a raw data format which contains pulse heights, arrival times and hits from the different detectors in the spectrometer. The deduction of the basic information from the raw data is called **data reconstruction**. The FOCUS reconstruction process, called **PASS1**, involves determining charged particle momenta and trajectories, identifying the particles, locating vertices, identifying electromagnetic, hadronic showers and their energies.

3.1 Track Reconstruction

The tracking routines reconstruct tracks independently within the microstrip detector (SSD) and within the spectrometer from multiwire proportional chamber system (PWC). Responses of these systems to charged particles were first reconstructed, and linking algorithm in turn matches together the fitted track segments which came from the same particle.

3.1.1 SSD Tracks

The SSD tracks were reconstructed in three main steps:

- Analysis hits in the SSD
- Projection finding

- Three dimensional space track fitting

Clusters of up to three hit channels are grouped into hit clusters. Using the ADC information, it is possible to determine if one of two traversing particles created a single cluster by comparing the total ADC counts present to the number expected for a single Minimum Ionizing Particle (MIP). For multi-strip, single-MIP hits, enhanced position resolution is achieved by fitting the ADC values in the cluster with a pulse height sharing algorithm. Projections are found in each of the three SSD measurement directions by taking all combinations of hits in the four SSD planes of given direction and fitting those hits to a straight line. Projections are rejected if χ^2 per degree of freedom (χ^2/DOF) is greater than 3. Projections must contain hits from at least three of the four planes; hits are allowed to be shared among three-plane projection and in the first plane of four-plane projections. Tracks are formed by intersecting all combinations of three projections (one from each view) and requiring that χ^2/DOF is less than 8 for these combinations. Shared projections among tracks are arbitrated based on the lowest χ^2/DOF and groups of tracks with nearly identical parameters are reduced to a single equivalent track. The spatial resolution of a track in the high resolution region of SSD is:

$$\begin{aligned} \sigma_{\mathrm{x}} &= 11.0\ \mu\mathrm{m} \cdot \sqrt{1 + \left(\frac{17.5\ \mathrm{GeV}/c}{p}\right)^2} \\ \sigma_{\mathrm{y}} &= 7.7\ \mu\mathrm{m} \cdot \sqrt{1 + \left(\frac{25.0\ \mathrm{GeV}/c}{p}\right)^2} \end{aligned} \tag{3.1}$$

where the second term under each square root indicates the momentum below which the MCS effects dominates. The 11.0 μm and 7.7 μm are the contributions to the resolutions due to the strip granularity and the quantities within the radicals describe the MCS contribution.[1] While the resolution of a track entirely in the low resolution region of the SSD is about twice as large. The Target Silicon (TSSD) is not used in finding the initial tracks in the target region.

[1] These are spatial resolutions of a track in E687. In FOCUS, these resolution are slightly better because the pulse height sharing algorithm is being used.

3.1.2 PWC Tracks

The PWC tracks can be also found by projection methods. Initially, the x (non-bend) components of SSD tracks are extrapolated through the spectrometer. PWC hits close to the extrapolation are used to form x projections. Projections in the y, u and v PWC planes are formed independently and combined with the x projections to form tracks. Unused hits in x are then used to form additional projections which are combined with the other unused projections to form additional tracks. The x projections found by extrapolating the SSD tracks must have hits in P0. Each track must have hits in at least three chambers and missing no more than four hits, only two of which may be in a single chamber. A least square fit is performed on all tracks to fix the track parameters (slopes and intercepts) and χ^2/DOF. For tracks passing through M2, the bend in the y direction is also included as a fit parameter, allowing a rough estimation of the momentum. Tracks which leave hits in all five PWCs are called "tracks" while those which leave hits only in the first three chambers are called "stubs". Additional algorithm are employed to recover tracks which do not satisfy the above criteria. For example, microstrip tracks are used to seed low momentum, two chamber tracks which exit the spectrometer after P1. Halo muon tracks, useful for certain studies, are reconstructed over a large area by reconstructing tracks with hits in P1, P2 and P4. These muons are assumed to pass through the steel magnet with little deflection. Occasionally the wire chambers have a very large number of hits which would produce many tracks. These events are too cluttered to extract reasonable physics, so in the interest of reducing the reconstruction time the number of tracks is limited to a maximum of 30. This limit is reached in roughly 3.5% of the events.

3.1.3 Linking of SSD and PWC Tracks

In order to obtain useful information for reconstructing charm decays, SSD and PWC tracks must be "linked", or associated with each other. This serves two purposes. First, it associates a momentum with an SSD track if the corresponding PWC track's momentum is measured in M2. Second, it allows determination of the momentum of stubs from the bend angle in M1. Linking is performed by extrapolating both SSD and PWC tracks to the center of M1. The slopes and intercepts of the two types of tracks are required to be consistent at this point. A

loose cut is applied to discard obviously incorrect choices. A global least square fit with both PWC and SSD hits is performed to test the hypothesis that the tracks come from the same particle. The links are arbitrated based on χ^2/DOF as returned by this fit. Because of e^+e^- pair production (with almost no opening angle), a maximum of two PWC tracks are allowed to be associated with each SSD track.

3.2 Vertexing

In order to perform certain kinds of reconstruction (for instance, finding the momentum of unlinked stubs), approximate vertex locations are required for each event. However, the approach described in this section has certain inefficiencies, so it is not typically used to find the vertices used in physics analyses. To find vertices, χ^2(x, y, z) in the equation

$$\chi^2 = \sum_{i=1}^{n} \left(\frac{\mathrm{x} - (\mathrm{x}_i + a_i' \mathrm{z})}{\sigma_{\mathrm{x},i}} \right)^2 + \left(\frac{\mathrm{y} - (\mathrm{y}_i + b_i' \mathrm{z})}{\sigma_{\mathrm{y},i}} \right)^2 \tag{3.2}$$

is minimized where (x, y, z) are the coordinate of the vertex; $\mathrm{x}_i, \mathrm{y}_i, a_i'$ and b_i' are the SSD track parameters; and $\sigma_{\mathrm{x},i}$ and $\sigma_{\mathrm{y},i}$ are the errors on the SSD tracks. The index i sums over the tracks in the vertex. To find the initial set of vertices all the SSD tracks in an event are forced into a single vertex. If χ^2/DOF is greater than 3, the track contributing most significantly to the χ^2 is removed from the vertex and the vertex is re-fitted. This process is repeated until χ^2/DOF is less than 3. At this point, all the tracks which no longer belong to a vertex are again forced into a single vertex and the process continues until all possible vertices have been established.

3.3 Momentum Determination

The momentum of charged particles are measured by determining their deflection angles in a magnet field. FOCUS uses two magnets to measure the momenta of charged particles; M1 is used to measure the momenta of three-chamber tracks and M2 for five-chamber tracks. For five-chamber tracks, particles are traced through the magnetic field using the known magnetic field in M2 and the track parameters

on both sides of the magnet as inputs to the calculation. This fit is performed iteratively until both accurate momentum and improved track parameters are obtained. Linked stubs and 4-chamber tracks are subjected to a similar procedure using the SSD track parameters, the track parameters between M1 and M2, and the known field of M1. Unlinked stubs pose a special problem since there is no information for them before they enter the magnetic field of M1. To obtain an approximate momentum measurement of these particles, the x projection of the track is extrapolated into the target region and the closest vertex is chosen as the point of origin. If no vertices are reconstructed, the unlinked stub is assumed to be originated from the center of the target material. The momentum resolutions are approximately

$$\begin{aligned} \frac{\sigma_p}{p} &= 3.4\% \cdot \left(\frac{p}{100\ \text{GeV}/c}\right) \cdot \sqrt{1+\left(\frac{17\ \text{GeV}/c}{p}\right)^2} \quad \text{for M1} \\ \frac{\sigma_p}{p} &= 1.4\% \cdot \left(\frac{p}{100\ \text{GeV}/c}\right) \cdot \sqrt{1+\left(\frac{23\ \text{GeV}/c}{p}\right)^2} \quad \text{for M2.} \end{aligned} \tag{3.3}$$

At high momentum, the resolution is limited by the position resolution of the PWC system and at low momentum it is dominated by MCS.

3.4 Particle Identification

3.4.1 Čerenkov Particle Identification [30]

FOCUS uses a Čerenkov algorithm know as **CITADL** which is based on particle hypothesis likelihoods for the stable charged particles e, π, K and p.[2] For each track, likelihoods $\mathcal{L}$s for each particle hypothesis are determined from observation of the cells status in the track's $\beta = 1$ Čerenkov light cone. If the number of photoelectrons expected in cell i for a track of given momentum under a particular particle hypothesis is μ_i then the Poisson probability of that cell firing is $(1 - e^{-\mu_i})$. In addition the cell has an accidental firing probability, a_i. Then the full

[2] Čerenkov Identification Through A Digital Likelihood.

contribution to the likelihood for cell i is given by

$$\mathcal{L}_i = \begin{cases} (1 - e^{-\mu_i}) + a_i - a_i(1 - e^{-\mu_i}) & \text{if the cell is on} \\ 1 - [(1 - e^{-\mu_i}) + a_i - a_i(1 - e^{-\mu_i})] & \text{if the cell is off} \end{cases} \tag{3.4}$$

In general the accidental rate is different for each cell and it is dependent on the instantaneous rate in the spectrometer. CITADL provides a set of χ^2-like variables $\mathcal{W}(i) \equiv -2\log(\mathcal{L})$ where i ranges over the four particle hypothesis. The hypothesis with the lowest $\mathcal{W}$ is the most likely. These variables will be used in the following ways:

- Separate one hypothesis from another with
  $\Delta\mathcal{W}_{i,j} \equiv \mathcal{W}(j) - \mathcal{W}(i) > n$
  such that hypothesis i is n units of $\mathcal{W}$ more likely then hypothesis j.

- Separation of a hypothesis from the minimum hypothesis with
  $\Delta\mathcal{W}_{i,\min} \equiv \mathcal{W}(\min) - \mathcal{W}(i) > n$.
  This selection is used to ensure that the chosen hypothesis is not wildly less likely then some other hypothesis.

Fig. 3.1 shows a 405,000 events golden mode charm sample obtained (from about 75% of our data) without any Čerenkov cuts. A selection of cuts on vertex detachment, isolation, (see Sec. 4.1) the $D^{*+} - D^0$ mass difference, and momentum were used to obtain this reasonably clean sample. Also shown are sideband regions used for background subtraction. Fig. 3.2 shows the likelihood difference $\Delta\mathcal{W}_{K,\pi}$ for the kaon and pion daughters from these background subtracted charm decays for tracks with two ranges of momentum. A positive $\Delta\mathcal{W}_{K,\pi}$ implies that a given track is more likely to be a kaon as opposed to a pion.

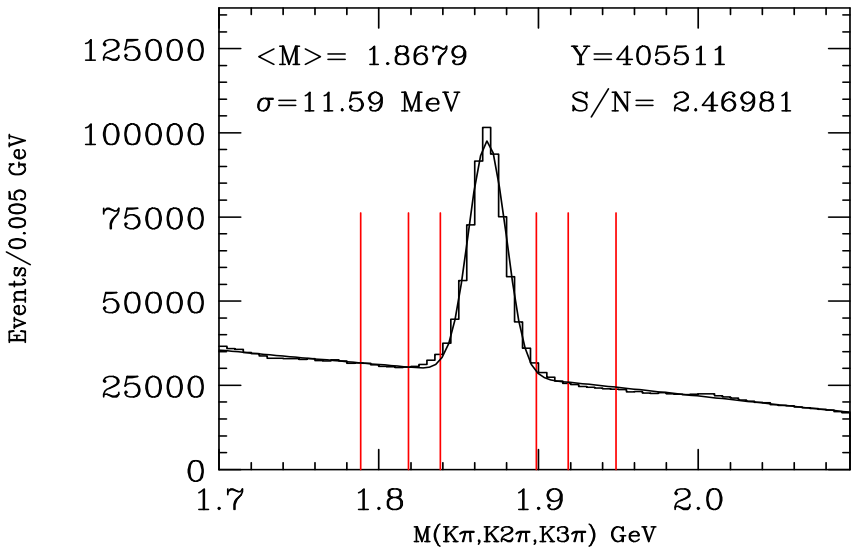

Figure 3.1: Invariant mass plot for the three golden mode decays $D^0 \to K^-\pi^+$, $K^-\pi^+\pi^+\pi^-$ and $D^+ \to K^-\pi^+\pi^+$. The reconstructed D^+ mass was shifted by 5 MeV/c^2 so that its peak will reconstruct in the same place as the peak of the D^0. This data has vertex quality and kinematic cuts only. No Čerenkov cuts were used. The vertical lines denote signal and sideband regions which will be used to make a background subtraction.

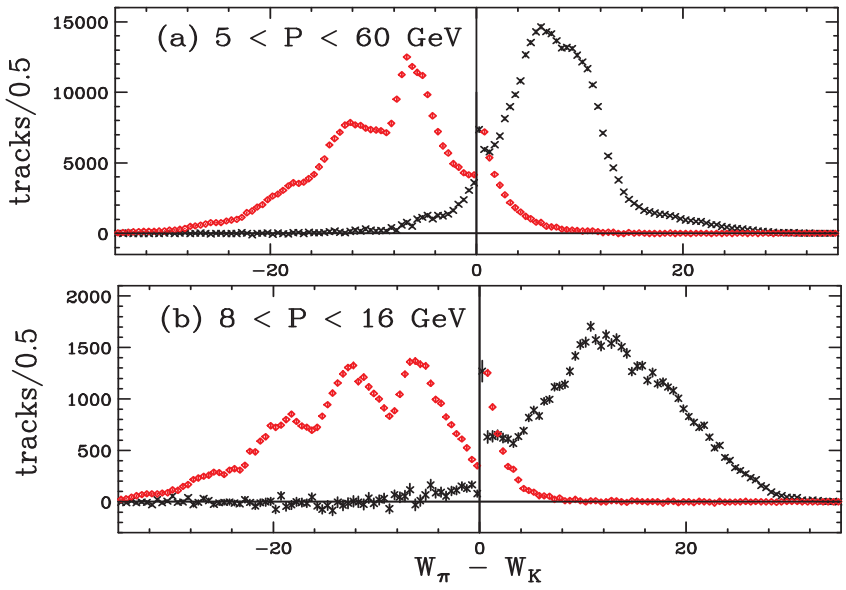

Figure 3.2: The log likelihood difference $\Delta\mathcal{W}_{K,\pi}$ distribution obtained from background subtracted kaons ($\times$'s and $*$'s) and pions (diamonds) from the golden mode charm signal shown in Fig. 3.1. The background distributions were rescaled to have the same area as the kaon distributions. Fig. (a) Track with momenta in the range $5 < p < 60$ GeV/c. Fig (b) Track with momenta in the range $8 < p < 16$ GeV/c.

3.4.2 Electron Identification

The electron identification provided by the Čerenkov system is reliable only up to the momentum where the pions are also above the Čerenkov threshold. For tracks which are only observed in the upstream of M2 the pion threshold (for C1) is about 8.5 GeV/c, while for five-chamber tracks the threshold (C3) is 17 GeV/c. For tracks above these thresholds electron identification requires the use of the electromagnetic calorimeters (IE and OE). The details of shower clustering and energy calculation differ in the inner and outer calorimeters, but both systems identify a track as an electron by comparing the energy (E) collected in the calorimeter cluster associated with the track to the track's momentum (p). The energy of an electron is typically fully contained in the electromagnetic calorimeter, while hadrons generally leave only a fraction of their energy in the system, and muons leave almost no energy.

Therefore a track and cluster combination with the ratio $E/p \approx 1$ has a high probability of identifying an electron.

3.4.3 Muon Identification

In the Inner Muon system, muons are identified by requiring hits in at least four of the six hodoscope planes. If the track momentum is below 10 GeV/c then only two hits are required. If the required number of hits are present then a χ^2 is calculated which gives a measure of the deviation of the hits from the extrapolated track. The hit positional errors used in the χ^2 calculation include both the scintillator paddle granularity and the expected multiple Coulomb scattering in the iron. This algorithm is described in detail in reference [28]. The methodology of muon identification in the Outer Muon system is similar to that used in the inner system, except that it is complicated by the presence of a magnetic field in the M2 iron [29]. Both systems provide muon identification confidence levels, which are set to zero when there are too few hits.

3.5 Reconstruction of Vees, Kinks, and Ξ^-'s/Ω^-'s [31]

3.5.1 Vees

K^0_S and Λ^0, usually referred to as **vees**, are found among the decay products of charmed hadrons. In the FOCUS experiment, these particles are reconstructed through the charged decay modes:

$$K^0_S \longrightarrow \pi^+\pi^- \qquad (\mathrm{BR} = 68.6\%)$$
$$\Lambda^0 \longrightarrow p\pi^- \qquad (\mathrm{BR} = 63.9\%)$$

These neutral vees have relatively long lifetime with respect to charm particles, and may travel several meters within the spectrometer before decaying. Depending on the decay region, they leave topologically distinct tracks and must be reconstructed with different algorithm. Fig. 3.3 shows four different decay regions and categories: **SSD vees**, which decay upstream of the SSD; **MIC vees**, which decay inside the SSD; **M1 vees**, which decay between the SSD and the first PWC station, P0; **Recon vees**, which decay between P0 and P2. In every case, vees are reconstructed

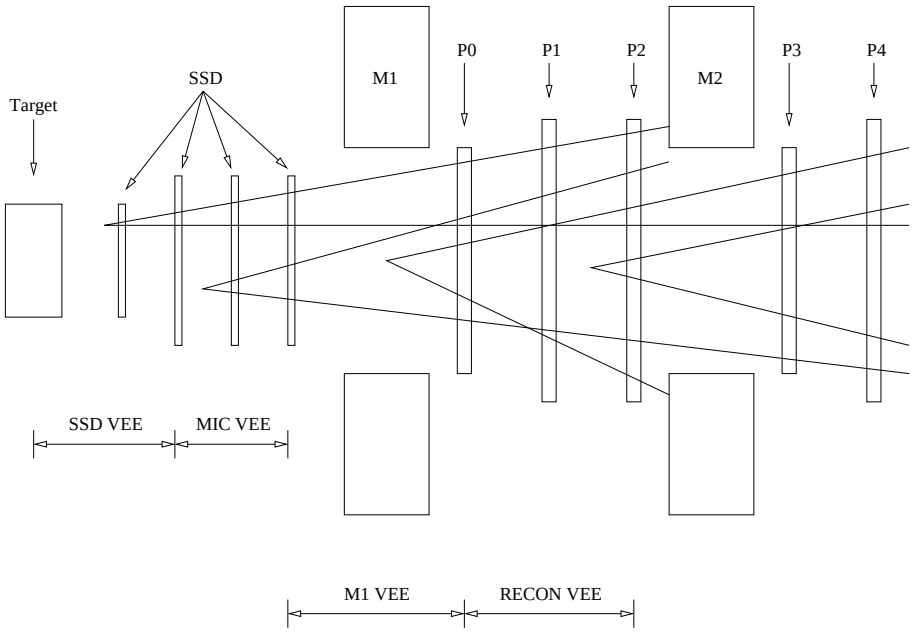

Figure 3.3: Schematics of the regions of the spectrometer where vees are reconstructed by the different algorithm.

over a decay length of about 10 m. Although they have the differences, all vee reconstruction algorithms have common features of the search for a pair of oppositely charged tracks which originate from a common point in a space, the vee decay vertex. The invariant mass of the pair is calculated, first assigning to both tracks the pion mass to test the K_S^0 hypothesis. Next, we have assigned the proton mass to the particle with higher momentum and the pion mass to lower momentum to examine the Λ^0. MIC vees and Recon vees are not used in FOCUS analyses.

SSD Vees The SSD vees decay upstream of SSD. These vees are searched for using the SDVERT algorithm (see Sec. 4.1) by looping over all pairs of oppositely charged linked SSD-PWC tracks and fitting for their vertex. The normalized mass is required to be less than 4.[3] The SSD vees are the highest resolution vees because they verticize upstream of the microstrips and therefore have low momentum and thus by virtue of Eq. 3.3 have very good momentum resolution. This is also the only vee class with good vertex resolution since the SSD vees contain SSD information.

[3] K_S^0 normalized mass is $\frac{|M(\pi^+\pi^-)-M(K_S^0)_{\rm PDG}|}{\sigma_{M(\pi^+\pi^-)}}$ and Λ^0's $\frac{|M(p\pi^-)-M(\Lambda^0)_{\rm PDG}|}{\sigma_{M(p\pi^-)}}$

The vee vertex is required to be in downstream of the primary by greater than 3σ (σ is the error for the distance between the primary and vee vertex).

M1 Vees The majority of vees are reconstructed in the M1 region, which covers the area between the last microstrip station and the first PWC station, P0. All M1 region vees are reconstructed using unlinked PWC tracks and are divided into three different sub-categories: *track-track* (**TT**) vee, formed by two unlinked five-chamber tracks; *track-stub* (**TS**) vee, formed by one five-chamber track and one three-chamber track; and *stub-stub* (**SS**) vee, formed by two unlinked three-chamber tracks. For each candidate pair of unlinked PWC tracks, the X and Z locations of the vee vertex are first estimated by intersecting the two daughter tracks in the non-bend view. An iterative procedure then traces the two daughter tracks through the M1 field and determines the Y position of the vee vertex. In case of the track-stub vee, the procedure also determines unknown momentum of the three-chamber track. For the stub-stub vee, however, an additional assumption is needed to determine the unknown momenta of both three-chamber tracks, along with the Y position of the vertex. With the assumption that the vee is originated from the primary vertex, the transverse momenta of the vee daughters can be balanced and all unknowns computed. Finally a global fit with the full covariance matrices of the tracks, including MCS contributions, is performed for each vee candidate to obtain a better momentum and decay vertex of the vee. A constraint that the vee point back to the primary vertex is included in the fit through a contribution of the χ^2. If the χ^2 is returned less than a certain value, the track parameters are updated and a vee quality flag is set on, otherwise the old parameters are retained. The normalized mass for M1 vee is required to be less than 5.

3.5.2 Kinks

The term **kink** refers to a decay where a long-lived charged particle passes through the SSD and then decays into a single charged track and a missing neutral track. The decay volume is from the end of the SSD to the main spectrometer chamber P0.

The following shows the decays that can be reconstructed from the kink topology:

$$
\begin{aligned}
\pi^- &\longrightarrow \mu^-\bar{\nu}_\mu \quad (\mathrm{BR} = 100\%) \\
K^- &\longrightarrow \mu^-\bar{\nu}_\mu \quad (\mathrm{BR} = 63.5\%) \text{ and } \pi^-\pi^0 \quad (\mathrm{BR} = 21.2\%) \\
\Sigma^+ &\longrightarrow p\pi^0 \quad (\mathrm{BR} = 51.6\%) \text{ and } \pi^+ n \quad (\mathrm{BR} = 48.3\%) \\
\Sigma^- &\longrightarrow \pi^- n \quad (\mathrm{BR} = 100\%) \\
\Xi^- &\longrightarrow \pi^-\Lambda^0 \quad (\mathrm{BR} = 100\%) \\
\Omega^- &\longrightarrow K^-\Lambda^0 \quad (\mathrm{BR} = 67.8\%)
\end{aligned}
$$

In order to reconstruct kinks, unlinked SSD tracks which point into the M1 aperture are matched with unlinked PWC tracks that also point into the aperture. PWC tracks which were previously used to form vees are not considered. The matching is performed with the x projections of the two tracks. For five-chamber PWC tracks which intersect upstream of M1, the momentum of the kink candidate is obtained by assuming the kink mass and solving the kinematic equations. However, this gives two momentum solutions for each kink, both of which must be considered to be valid. For five-chamber PWC intersections within M1, both the charged track and kink are traced through the magnetic field. The momentum of the kink is varied until the intersection distance is minimized, giving an approximate value for the kink momentum. As before, the kinematic equations are solved, but in this case the kink momentum value closest to the value found during the iteration is chosen. For three-chamber PWC tracks, the kink decay must occur upstream of M1. The (x, y, z) of the kink decay vertex is obtained by taking the x and z intersection points of the two tracks. The y value is fixed from the SSD track parameters at the z of intersection. Again, the kink mass is assumed to calculate the kink momentum. In order to reject topologically similar backgrounds, particle ID from the Čerenkov system is placed on the charged tracks and an E/p cut is made on neutrons. Requiring a confirming π^0 also reduces background, but this is not done at the reconstruction stage because such a requirement is very inefficient.

3.5.3 Ξ^-'s/Ω^-'s

The Ξ^- and Ω^- hyperons, referred to as **cascade** are fully reconstructed through their decay modes:

$$\Xi^- \longrightarrow \Lambda^0\pi^- \qquad (\mathrm{BR} = 100\%)$$
$$\Omega^- \longrightarrow \Lambda^0 K^- \qquad (\mathrm{BR} = 67.8\%)$$

The cascade reconstruction considers two cases. In the first case, the Ξ^- or Ω^- decays in the target region, upstream of the SSD detectors. In this case, we require that the charged track (the π^- or the K^-) forms a good vertex with Λ^0 momentum vector and that the combination points back to another vertex. In second case, the Ξ^- or Ω^- decays downstream of the SSD detector. This is similar to the kink topology, but the neutral particle (Λ^0) is fully reconstructed. The algorithm begins by finding a vertex between a Λ^0 and an unlinked PWC track, both of which must be traced into the magnetic field of M1. When the best fit for this vertex is found, the unlinked SSD track (the Ξ^- or the Ω^-) is also traced into M1. If the two traced objects intersect, the entire decay is refit with the new cascade decay vertex position. Both cascade topologies place additional requirements on the Λ^0 in order to reject backgrounds.

3.6 Data Processing

The FOCUS collaboration recorded 5926 8 mm tapes of good photon interaction data. Each data tape has a capacity of 4.5 GBs which holds on average 1.1 million triggered events for a total of 27 TBs and 6.5 billion events. The data were processed in three collaboration wide stages, in order to make it manageable for individual analyses. The three stages were known as **PASS1**, **SKIM1** and **SKIM2**. These collective processing stages took nearly two years to complete.

3.6.1 PASS1

PASS1 was conducted on the Fermilab processing farms using CPS [32], a distributed computing package developed and maintained by Fermilab's Computing Division. CPS groups together a server node and a cluster of about ten worker nodes into a computing farm. In this way a single data tape can be processed in

parallel on ten computers. During PASS1 all the major reconstruction algorithm were run. This stage of processing was most intense computationally. The reconstructed data were added to the raw data and written to tape. Each tape of input corresponded to a single tape of PASS1 output. The addition of the reconstructed data to the output tape was offset by compressing raw data blocks, by rejecting events with certain kinds of reconstruction errors and from very loose selection cuts. About 10% of events were rejected at the PASS1 level.

3.6.2 SKIM1

At the next level of processing, known as SKIM1, data from the PASS1 output tapes was split into six separate streams (known as superstreams to distinguish them from the output of SKIM2) based on physics selection criteria (see Table 3.1). This splitting process resulted in more manageable data sets ranging in size from 200 to 500 tapes. In addition to splitting the data, some reconstruction algorithms were rerun to fix problems discovered in the original PASS1 algorithms. The SKIM1 processing was carried out at Vanderbilt University and the University of Colorado. Each used their own locally produced control software, but both institutions relied on large clusters of computers and tape stackers. Unlike PASS1, SKIM1 was primarily limited by the speed of tape reading and writing.

3.6.3 SKIM2

The final stage of collective data processing, referred to as SKIM2, further split the data into specific physics topics. In many cases there "substreams" were tailored to the specification of an individual collaboration member. Each of the SKIM1 superstreams was processed at a single institution. The specifics of each SKIM2 setup varied from skim to skim, but most of the skims used skim control software known as the Generalized Skim Framework (GSF). The GSF maintained databases and provided data processing control, disk management and permanent skim record keeping. All but a few of the SKIM2 substream fit on less than 100 tapes and many fit on fewer than 25 tapes.

Super stream	Physics Topics	SKIM2 Institution
1	Semi-leptonic decays	Puerto Rico
2	Topological vertexing and K_S^0	Illinois
3	Rare decays and Calibration	CBPF, Brazil
4	Baryons	Fermilab
5	Light quark states	UC Davis
6	Meson hadronic decays	UC Davis

Table 3.1: Description of the six SKIM1 superstreams with thier SKIM2 computing institutions.

Chapter 4

Branching Ratio Measurements

In this chapter we analyze the four hadronic decay modes of the D^+ into the final states of $K^0_S K^-\pi^+\pi^+$, $K^0_S K^+\pi^+\pi^-$, $K^0_S K^+ K^-\pi^+$ and $K^0_S\pi^+\pi^+\pi^-$ and two hadronic decays of the D^+_s into the $K^0_S K^-\pi^+\pi^+$ and $K^0_S K^+\pi^+\pi^-$. We have measured the branching ratios of the $D^+ \to K^0_S K^-\pi^+\pi^+$, $D^+ \to K^0_S K^+\pi^+\pi^-$ and $D^+ \to K^0_S K^+ K^-\pi^+$ relative to the $D^+ \to K^0_S\pi^+\pi^+\pi^-$ and $D^+_s \to K^0_S K^+\pi^+\pi^-$ relative to the $D^+_s \to K^0_S K^-\pi^+\pi^+$ using Eq. 4.1. Among these decay modes $D^+ \to K^0_S K^-\pi^+\pi^+$ and $D^+ \to K^0_S K^+\pi^+\pi^-$ are Cabibbo suppressed decay modes and others are Cabibbo favored decay modes (see Table 4.1).

$$\Gamma_{\rm rel} \;=\; \frac{\mathcal{N}_{\text{signal mode}}}{\mathcal{N}_{\text{nomalized mode}}} \cdot \frac{\mathcal{E}_{\text{normalized mode}}}{\mathcal{E}_{\text{signal mode}}} \tag{4.1}$$

$D^+ \to K^0 K^-\pi^+\pi^+ \to K^0_S K^-\pi^+\pi^+$	Cabibbo suppressed	
$D^+ \to \overline{K}^0 K^+\pi^+\pi^- \to K^0_S K^+\pi^+\pi^-$	Cabibbo suppressed	
$D^+ \to \overline{K}^0 K^+ K^-\pi^+ \to K^0_S K^+ K^-\pi^+$	Cabibbo favored	†
$D^+ \to \overline{K}^0\pi^+\pi^+\pi^- \to K^0_S\pi^+\pi^+\pi^-$	Cabibbo favored	†
$D^+_s \to K^0 K^-\pi^+\pi^+ \to K^0_S K^-\pi^+\pi^+$	Cabibbo favored	
$D^+_s \to \overline{K}^0 K^+\pi^+\pi^- \to K^0_S K^+\pi^+\pi^-$	Cabibbo favored	†

Table 4.1: Decay modes studied in this thesis. Modes marked with † can occur from doubly Cabibbo suppressed decay mode also if K^0_S comes from K^0 in these decay modes.

where $\mathcal{N}$ is number of observed events and $\mathcal{E}$ is reconstruction efficiency. First, we introduce analysis tool used in FOCUS experiment, referred to as Candidate-Driven Vertex Algorithm.

4.1 Candidate-Driven Vertex Algorithm

In any charm analysis, it is most fundamental to determine the production or primary vertex, where the charm particles are produced by the photon-nucleon interaction, and the decay or secondary vertex, where the charm particles decay into daughter particles and separation between them. The ability to reconstruct the charm production and decay vertices with good precision of separation is the most compelling signature of a charm event, as opposed to a non-charm hadronic event or an electromagnetic event, where all particles originate from the same vertex. The vertexing algorithm most commonly uses in FOCUS analysis is called a **Candidate-Driven** algorithm or **SDVERT**. The SDVERT gives five cuts to find and isolate charm signals and Fig. 4.1 schematically shows them.

4.1.1 Secondary Vertexing

A combination of objects compatible with the charm decay of interest is selected and fed to the SDVERT. The SDVERT examines the hypothesis that all the objects of the combination which contain SSD information are compatible with coming from the same point in space, the candidate secondary vertex. The probability that this occurs is returned by the SDVERT as a confidence level for the secondary vertex (**CLS**), which is required to be greater than some threshold value. Typically, in order to form a secondary vertex, a combination must have at least two objects of them which have SSD information since decay objects not having SSD information such as π^0, spectrometer vees, Ξ^- and Ω^- are not used in the construction of the secondary vertex. Therefore, this could be a combination of some linked charged tracks as in the decay $D^0 \to K^-\pi^+$, $D^+ \to K^-\pi^+\pi^+$ and $\Lambda_c^+ \to pK^-\pi^+$, or a combination of some linked charged tracks and some neutral or longer living particles, such as in the decay $D^0 \to K^-\pi^+\pi^0$, $D^0 \to K_S^0\pi^+\pi^+$ and $\Lambda_c^+ \to \Lambda^0\pi^+\pi^+\pi^-$. In case of an **one-prong decay**, where just one decay object has SSD information such as $D_s^+ \to K_S^0K^+$, if the K_S^0 is reconstructed in the spectrometer, no secondary

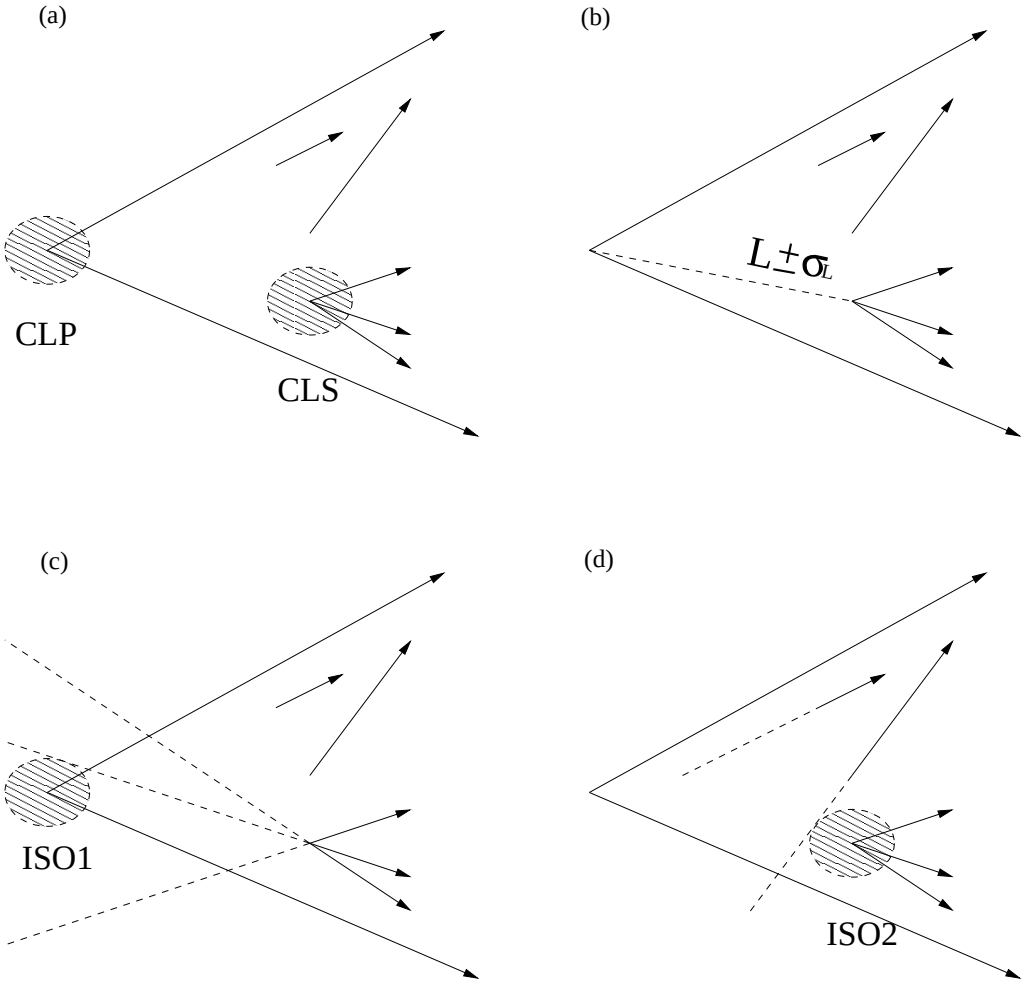

Figure 4.1: Schematics of the five output parameters from the candidate-driven vertex algorithm: (a) CLP and CLS, (b)L/σ_L, (c) ISO1 and (d) ISO2.

vertex formed through the common way. The secondary vertexing for one-prong decay will be explained in next section.

4.1.2 Primary Vertexing

The primary vertex of candidate charm is reconstructed depending on the decay topology. The most common case is all the decay daughters are reconstructed and at least two of them have SSD information. In this case the total momentum of the decay objects is equal to the candidate parent charm and a secondary vertex can be reconstructed using decay daughters. Therefore, it is possible to attach the total momentum to the secondary vertex and use it as a *seed* to look for the primary vertex. The primary vertex construction begins by choosing all of the SSD tracks, excluding the daughter objects, which intersect in space with the charm seed. A minimum cut on the confidence level for the vertex (**CLP**) is required for an intersection to be accepted. If only one intersecting track is found, its intersection with the seed is assumed to be the primary vertex. If more than one track is found, the algorithm first checks if any two of these tracks make a common vertex with the seed. If no pair is found, the primary vertex location is given by the highest confidence level intersection between a single track and the seed. If as least one pair is found, the primary vertex is given by the intersection of the two tracks of the pair. At this point all other SSD tracks which intersect the seed are added one at a time to the vertex, and are included if the confidence level of the object remains above 1%. In case of an one-prong decay, no secondary vertex has been reconstructed. However, the two decay daughters can define a plane which must contain the primary vertex using their momentum vectors. Therefore, it is also possible to reconstruct the primary vertex with a similar manner described just previously, but clustering SSD tracks around a *seed plane*, not a seed track. To intersect the seed plane, the algorithm must start by looking for a pair of tracks making a common vertex in the seed plane. Therefore, no single track is accepted in the primary vertex. Then, other SSD tracks in the events are clustered around the best pair as long as the confidence level of the vertex remains above 1%. To obtain a secondary vertex for one-prong decay we force the one-prong object to originate at primary vertex since we do not know where it intersects. This allows us to book the one-prong object information in the standard fashion. Confidence level that

an one-prong object verticizes with a charged daughter track of charm candidate is the CLS for one-prong decay that we could not form through the common way in Sec 4.1.1 [34]. Once the primary and secondary vertices are reconstructed, the distance L between them and its error σ_L are calculated. L/σ_L then, is to be *significance of separation* between the two vertices. Requiring the L/σ_L to be greater than a threshold value finds the finite lifetime nature of charm particles in order for rejecting non-charm hadronic and combinatoric background. L/σ_L is the principal selection tool used in the FOCUS analysis and in other fixed-target experiments in general.

4.1.3 Vertex Isolation

The SDVERT also gives two values to isolate the secondary vertex, of which use is an effective way to improve the signal to background. The first isolation tool determines whether the daughter tracks forming the secondary vertex are compatible with coming from the primary vertex. Objects with SSD information from the secondary vertex are added one at a time to the primary and global fit for the primary vertex is performed again. A confidence level for the new object is calculated and the highest confidence level found in the process is retained and denoted as **ISO1**. The ISO1 is designed to cut out events where tracks originally from the primary vertex erroneously are assigned in a secondary vertex candidate. For example, shown in Fig. 4.2 this cut removes the contamination coming from the decay $D^{*+} \to D^0\pi^+ \to (K^0_S\pi^+\pi^-)\pi^+$ in $D^+ \to K^0_S\pi^+\pi^+\pi^-$ final state. The second isolation tool determines whether other SSD object in the event excluding the ones coming from the primary vertex are compatible with originating in the secondary vertex. Again, these objects are assigned one at a time to the secondary vertex and the highest confidence level of the new objects is returned and denoted as **ISO2**. The ISO2 is designed to reject background from higher multiplicity charm events which have been partially reconstructed by the vertexing algorithm.

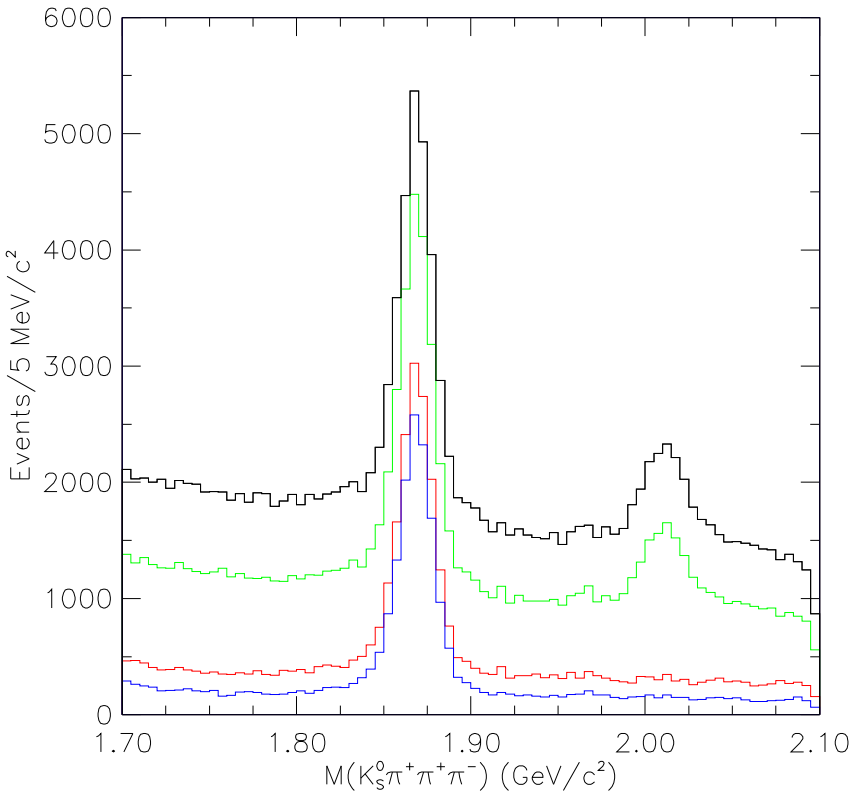

Figure 4.2: Signal evolution for $D^+ \to K^0_S\pi^+\pi^+\pi^-$ final state starting with minimum requirements, $L/\sigma_L > 9$, ISO1<1% and ISO2<0.1%.

	Cuts	$\mathcal{N}(D^+ \to K^0_S\pi^+\pi^+\pi^-)$	$\frac{\mathcal{N}^2_{\rm signal}}{\mathcal{N}_{\rm signal}+\mathcal{N}_{\rm background}}$
(1)	Minimum cuts	17264±209	6823
(2)	(1) and $L/\sigma_L > 9$	15992±182	7721
(3)	(2) and ISO1 < 1.0%	12905±136	9004
(4)	(3) and ISO2 < 0.1%	11590±121	9175

Table 4.2: Signal yields and figure of merits for $D^+ \to K^0_S\pi^+\pi^+\pi^-$ final state in Fig. 4.2.

4.2 Events Selection

We chose the signal events maximizing the figure of merit, Eq. 4.2, and also minimizing reflection backgrounds for all decay channels in this thesis.

$$\mathcal{F} = \frac{\mathcal{N}^2_{\text{signal}}}{\mathcal{N}_{\text{signal}} + \mathcal{N}_{\text{background}}} \tag{4.2}$$

4.2.1 K^0_S Selection [33]

All decay channels we have studied involve K^0_S. In order to identify clean K^0_S, we have applied tighter selection cuts in addition to ordinary K^0_S reconstruction as described in Sec. 3.5.1.

- Use SSD K^0_S and M1(TT, TS, SS) K^0_S
- $|M(\pi^+\pi^-) - M(K^0_S)_{\text{PDG}}| < 3\sigma_{M_{\pi^+\pi^-}}$
- $\Delta\mathcal{W}_{\pi,p} > -5$ for K^0_S daughter track with higher momentum
- Investigate shared K^0_S legs if there are one more K^0_S in the event
  i. If SSD K^0_S leg shared with other SSD K^0_S's, then pick the one with best vertex fit confidence level
  ii. If TT K^0_S leg shared with other TT K^0_S's, then pick the one with the smallest DOCA
  iii. If TT K^0_S leg shared with other TS K^0_S's, then always pick the TT K^0_S
  iv. If TS K^0_S leg shared with other TS K^0_S's, then pick the one with smallest mass error
  v. If TS K^0_S leg shared with other SS K^0_S's, then always pick the TS K^0_S
  vi. If SS K^0_S leg shared with other SS K^0_S's, then pick the one with smallest mass error

Fig. 4.3 shows $\pi^+\pi^-$ and $p\pi^-$ invariant mass distributions after and before using K^0_S selection used in this analysis. It shows our K^0_S selection cuts are rather effective to remove K^0_S background and Λ^0 background in K^0_S.

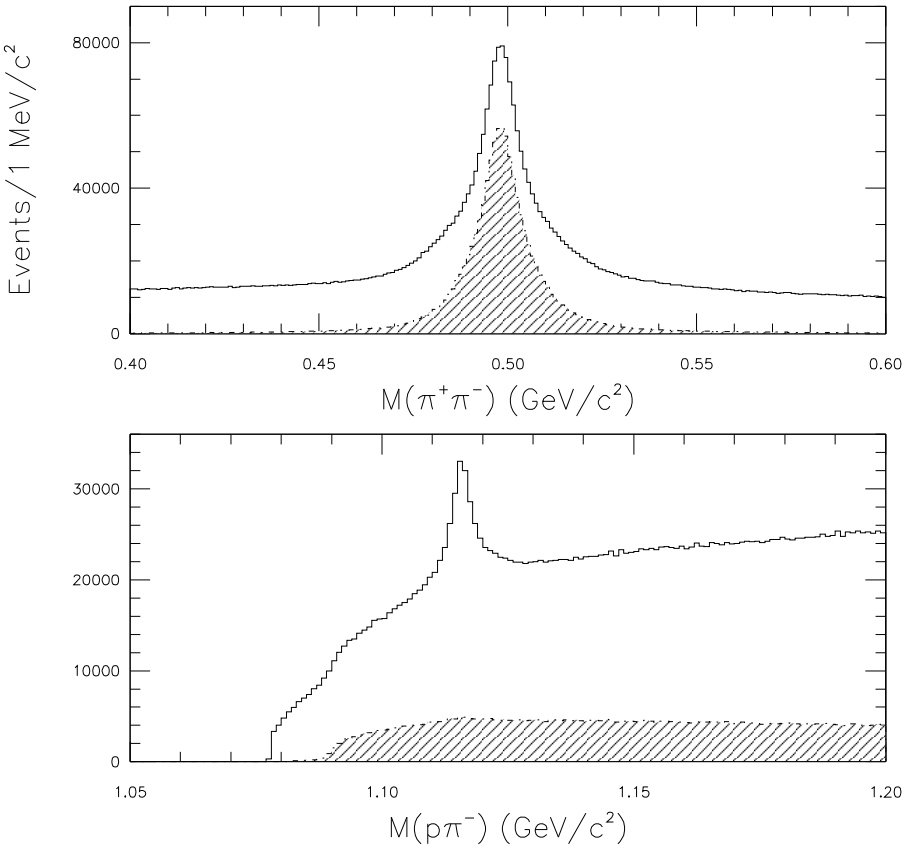

Figure 4.3: Upper plot shows the invariant mass of $M(\pi^+\pi^-)$ and down one shows $M(p\pi^-)$. Histogram is before using K^0_S selection and hatched one is after passing K^0_S selection.

4.2.2 Vertexing

To reduce the systematics, we have employed same vertexing conditions for all decay modes. All decay modes in this thesis have same decay topology, $K^0_S + 3\ prongs$, thus same vertexing requirement is quite reasonable. We required somewhat tighter vertex isolation requirements. Though these tight vertex isolation cuts reduce the value of Eq 4.2, but effective to remove backgrounds as shown in Fig. 4.2. Fig. 4.4 shows the $D^+ \to K^0_S K^- \pi^+ \pi^+$ signal yields for different L/σ_L requirements.

- CLP $> 1.0\%$
- CLS $> 1.0\%$
- ISO1 $< 1.0\%$
- ISO2 $< 0.1\%$
- $L/\sigma_L > 9$ for the D^+ candidates and $L/\sigma_L > 7$ for the D^+_s candidates

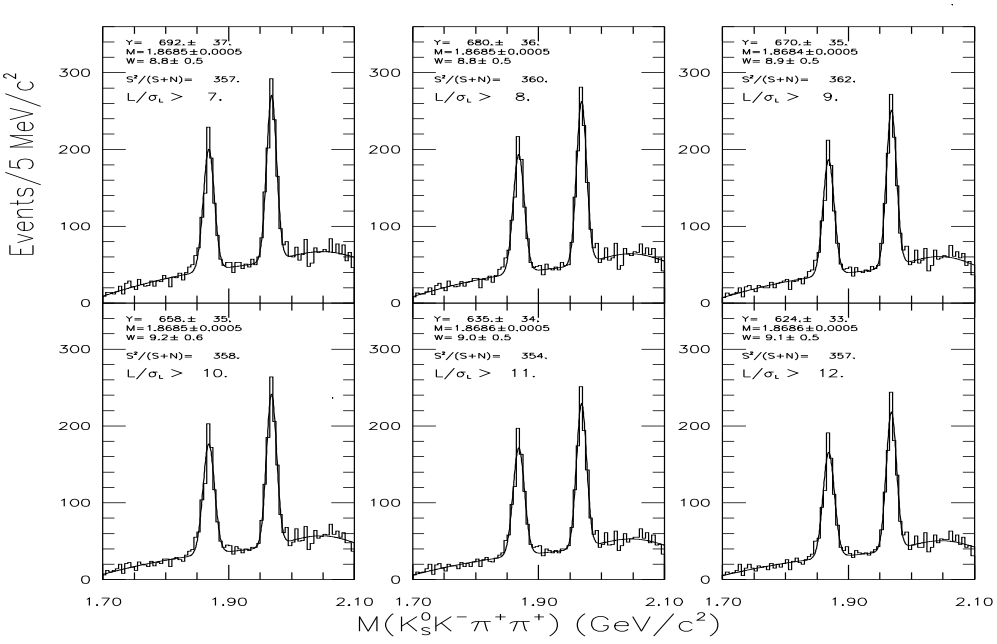

Figure 4.4: $D^+ \to K^0_S K^- \pi^+ \pi^+$ signal evolutions for different L/σ_L cuts.

4.2.3 Particle Identification

- $\Delta\mathcal{W}_{K,\pi} > 2$ for kaon

  In case of the $D^+ \to K^0_S K^+ K^- \pi^+$, $\Delta\mathcal{W}_{K,\pi} > 2$ for faster kaon and $\Delta\mathcal{W}_{K,\pi} > 1$ for slower one

- $\Delta\mathcal{W}_{\pi,\mathrm{min}} > -6$ for pion

In some other analyses, $\Delta\mathcal{W}_{K,p}$ requirement is effective in removing K misidentification to p [35, 36]. In this analysis, we do not impose $\Delta\mathcal{W}_{K,p}$ cut. We have also other two constraints of particle identification in addition to one kaon identification. Thus this cut is not effective to our decay modes. For the same reason, we have not required tighter pion selection cuts such as $\Delta\mathcal{W}_{\pi,p}$ and $\Delta\mathcal{W}_{\pi,K}$. Fig. 4.5 shows the $D^+ \to K^0_S K^- \pi^+ \pi^+$ signal yields for different $\Delta\mathcal{W}_{K,\pi}$ requirements.

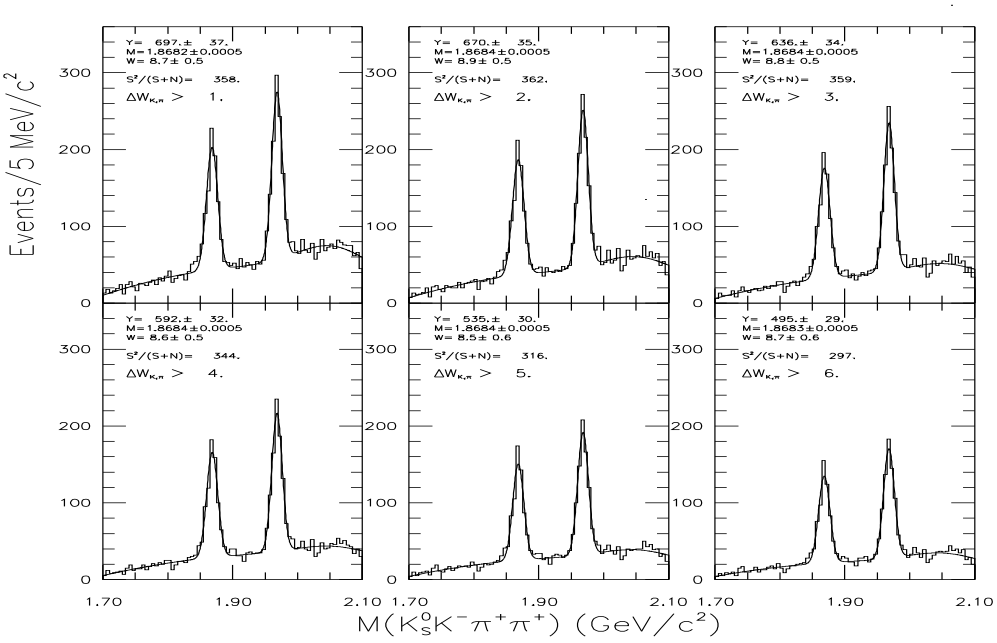

Figure 4.5: $D^+ \to K^0_S K^- \pi^+ \pi^+$ signal evolutions for different $\Delta\mathcal{W}_{K,\pi}$.

4.2.4 Others

- Momentum of charm candidate is greater than 30 GeV/c.
- All charged tracks must be reconstructed in both the SSD and PWC systems and be linked.
- Proper decay time is less than 5 times of the candidate particle's lifetime [1].
- Secondary vertices must be out of target segments.

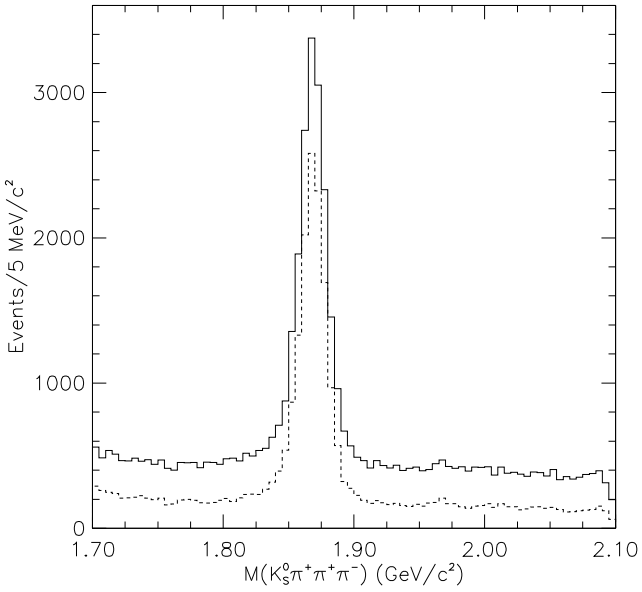

Figure 4.6: The invariant mass distribution of $K^0_S\pi^+\pi^+\pi^-$ final state without (histogram) and with (dot) out of material cut. Yield of histogram is 14564±148 and its signal to noise ratio, S/N is 6. While yield of dot is 11590±121, its S/N is 12.

In a fixed-target experiment, charmed particles are usually produced carrying a significant fraction of the beam momentum. In addition, acceptance and identification of high momentum parent particles is more efficient. Therefore, a cut on the charm momentum of 30 GeV/c removes a small amount of background with almost no loss in signal. A lifetime cut is very effective in eliminating D^+ background in

D_s^+ measurement since D^+ lifetime is longer than two times that of D_s^+. Besides, lifetime cut is effective to remove background from very large detachment. We have required secondary vertices must be out of target segments, referred as "*out of material cut*", to eliminate backgrounds from interactions which are induced by particles from the primary interaction or from conversion of spurious photons. Fig. 4.6 illustrates the effectiveness of the out of material cut.

4.3 Branching Ratio Measurements of D^+ Channels

4.3.1 $D^+ \to K_S^0\pi^+\pi^+\pi^-$

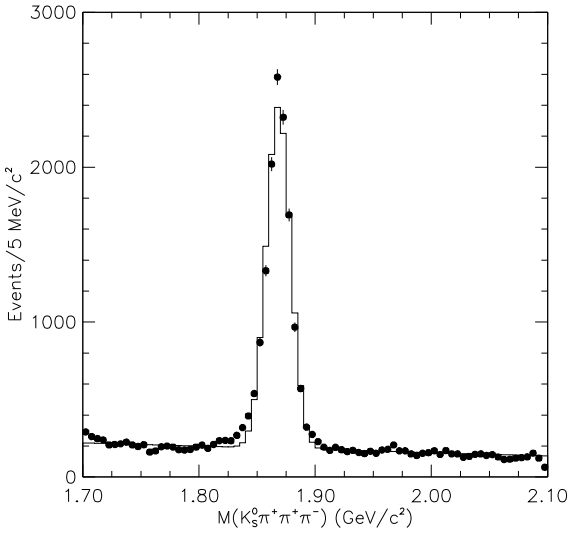

Figure 4.7: The invariant mass distribution of $K_S^0\pi^+\pi^+\pi^-$ with D^+ selection cuts. The data are indicated by points with error bars and the solid lines are the fits.

This final state is known as coming from several sub-decay channels shown in Table 4.3 [1]. Fig. 4.7 shows $K_S^0\pi^+\pi^+\pi^-$ final state from the FOCUS data. The signals are fitted by a Gaussian and backgrounds are linear polynomial. We have obtained 11,590$\pm$121 events for this final state. As shown in Table 4.3, each resonant efficiency of this final state is differ due to geometrical acceptance of the FOCUS

Decay Channels	Γ (%)	$\mathcal{E}$ (%)
Non R. $K^0_S\pi^+\pi^+\pi^-$	0.8±0.4	1.531±0.012
$K^0_S a^+(1260)(\rho^0(\pi^+\pi^-)\pi^+)$	4.0±0.9	1.604±0.012
$K^{*-}(K^0_S\pi^-)\pi^+\pi^+$	1.4±0.6	1.579±0.012
$K^0_S\rho^0(\pi^+\pi^-)\pi^+$	0.5±0.5	1.580±0.012
$\overline{K}^0_1(1400)(K^{*-}(K^0_S\pi^-)\pi^+)\pi^+$	2.2±0.6	1.586±0.012
Incoherently Mixed MC		**1.590±0.012**
Mini MC		1.588±0.003

Table 4.3: Known decay channels in the $D^+ \to K^0_S\pi^+\pi^+\pi^-$ final state. Γ is current branching ratio and $\mathcal{E}$ is its efficiency. $\mathcal{E}$s' do not include $\Gamma(K^0_S \to \pi^+\pi^-)$ and branching ratio of other resonance particles, and its error is Monte Carlo statistical error.

spectrometer. We have generated incoherently mixed Monte Carlo data according to current PDG value and calculated efficiency for that case. Actually, there are many interferences among each intermediate state. To see an interference effect we performed a mini-Monte Carlo study. We determined final state efficiency, $\mathcal{E}_{\text{final}}$ using Eq. 4.3.

$$\mathcal{E}_{\text{final}} = \frac{\sum_i \Gamma_i \mathcal{E}_i}{\sum_j \Gamma_j} \tag{4.3}$$

We allowed 6σ of Γ_i in Eq. 4.3 to incorporate the interferences. The Γ_i is branching fraction of sub-resonant state of $D^+ \to K^0_S\pi^+\pi^+\pi^-$ final state and $\mathcal{E}_i$ is its efficiency shown in Table 4.3. Fig. 4.8 shows the results of mini-Monte Carlo study. They show that our incoherently mixed Monte Carlo results are consistent with mini-Monte Carlo results. Therefore, we have neglected systematics from resonant state efficiency for this decay mode. There might be contamination from $\Lambda^+_c \to \Lambda^0\pi^+\pi^+\pi^-$ mode if Λ^0 is misidentified to K^0_S. Although our K^0_S selection removes Λ^0 from K^0_S as shown in Sec. 4.2.1, we investigated this contamination by assigning a nominal Λ^0 mass instead of K^0_S mass in the data. Fig. 4.9 is sideband subtracted $\Lambda^0\pi^+\pi^+\pi^-$ invariant mass and shows no contamination in decay channel. This final state is used to normalization mode for D^+.

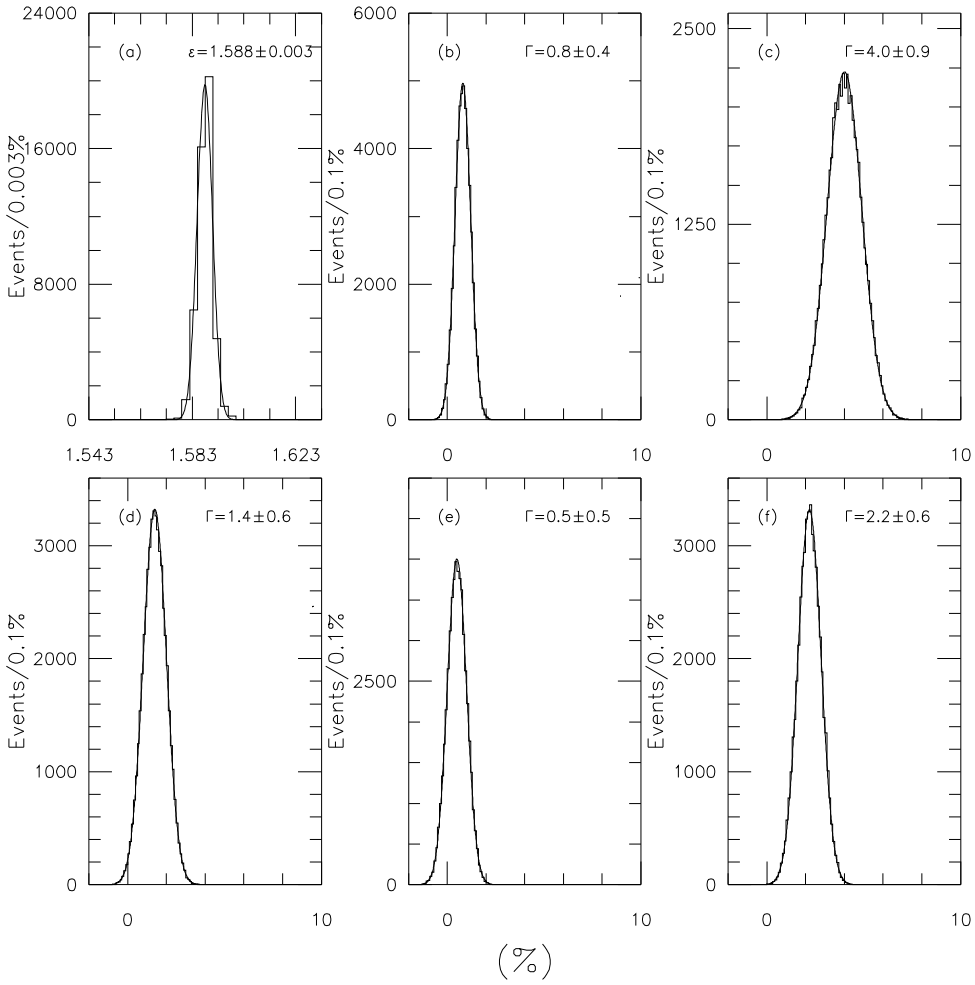

Figure 4.8: $D^+ \to K^0_S\pi^+\pi^+\pi^-$ Mini Monte Carlo results: (a) the efficiency, (b) $\Gamma(D^+ \to N \cdot R\ K^0_S\pi^+\pi^+\pi^-)$, (c) $\Gamma(D^+ \to K^0_S a^+(1260))$, (d) $\Gamma(D^+ \to K^{*-}\pi^+\pi^-)$, (e) $\Gamma(D^+ \to K^0_S\rho^0\pi^+)$, (f) $\Gamma(D^+ \to \overline{K}^0_1(1400)\pi^+)$.

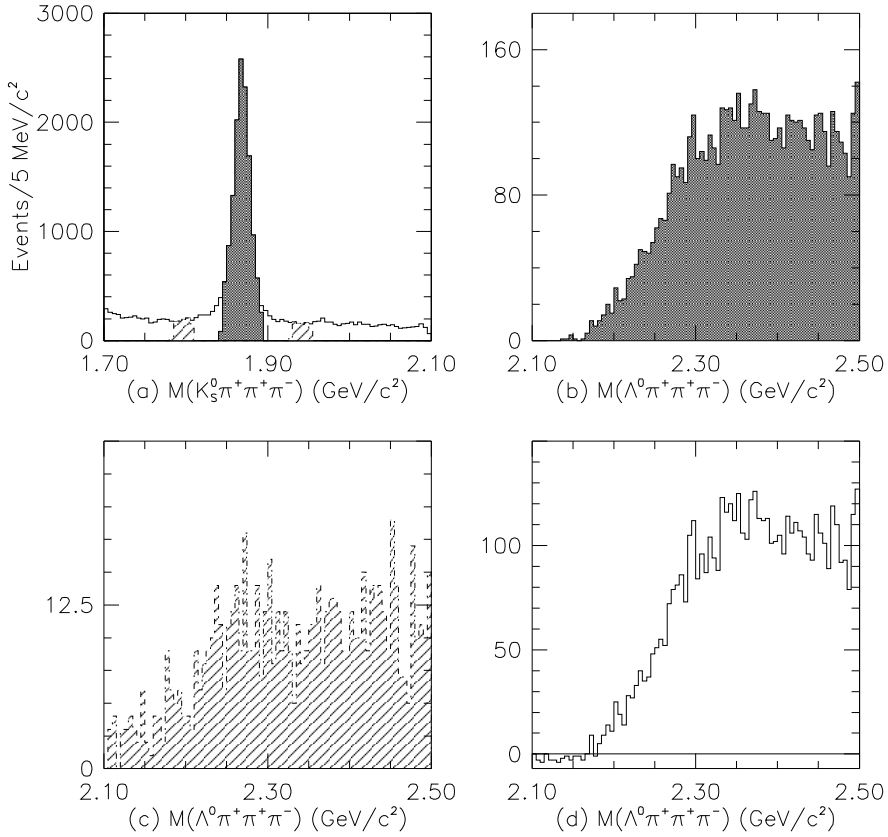

Figure 4.9: (a) is $M(K^0_S\pi^+\pi^+\pi^-)$. Shadowed is 2.5σ of signal region and hatched is sideband region. (b) is $M(\Lambda^0\pi^+\pi^+\pi^-)$ within $M(K^0_S\pi^+\pi^+\pi^-)$ signal region. (c) is $M(\Lambda^0\pi^+\pi^+\pi^-)$ within $M(K^0_S\pi^+\pi^+\pi^-)$ sideband region. (d) is sideband subtracted $M(\Lambda^0\pi^+\pi^+\pi^-)$ distribution in the $D^+ \to K^0_S\pi^+\pi^+\pi^-$ signal region.

4.3.2 $D^+ \to K^0_S K^-\pi^+\pi^+$

This final state may be produced from several two-body or three-body intermediate resonant states or non-resonant state shown in Table 4.4.[1] This final state is shown in Fig. 4.10. We parameterized signal by a Gaussian and background by quadratic polynomial and charm reflection. We have obtained 670±35 events in this mode. Monte Carlo simulation, shown in Fig. 4.11, shows this reflection mainly comes from $D^+ \to K^0_S\pi^+\pi^+\pi^-$ channel due to π/K misidentification. Reflection background shape is determined by Monte Carlo simulation and amplitude is a free fit parameter. There might be some contaminations from $K^0_S K^+\pi^+\pi^-$ decay mode due to double particle misidentification. We saw no contribution in data and Fig. 4.12 shows the $K^0_S K^+\pi^+\pi^-$ contribution in $D^+ \to K^0_S K^-\pi^+\pi^+$ signal region. This state also have different reconstruction efficiencies like the case of $D^+ \to K^0_S\pi^+\pi^+\pi^-$. If there were well known resonant analyses for this channel, we could determine the efficiency using the method applied in $D^+ \to K^0_S\pi^+\pi^+\pi^-$ decay mode. Unfortunately, no detailed study is carried out yet. We have investigated possible resonant states in this final state to determine the efficiency for this final state.

Decay Channels	$\mathcal{E}$ (%)
$Non\ R.\ K^0_S K^-\pi^+\pi^+$	1.140±0.010
$K^{*+}(K^0_S\pi^+)K^-\pi^+$	1.145±0.010
$K^0_S\overline{K}^{*0}(K^-\pi^+)\pi^+$	1.162±0.010
$\mathbf{K^{*+}(K^0_S\pi^+)\overline{K}^{*0}(K^-\pi^+)}$	**1.197±0.010**
$a^-(K^0_S K^-)\pi^+\pi^+$	1.104±0.010

Table 4.4: Possible decay channels in $D^+ \to K^0_S K^-\pi^+\pi^+$ final state and its efficiencies. $\mathcal{E}$s' do not include $\Gamma(K^0_S \to \pi^+\pi^-)$ and branching ratio of other resonance particles, and its error is Monte Carlo statistical error.

Fig. 4.13 shows sideband subtracted resonant states.[2] From Fig. 4.13 we determined

[1] This state may come from other higher mass resonances, such as $\phi(1680)$ meson. But we do not consider these higher mass resonance since we do not see any evidence for these states

[2] There are two same charged pions which does not make us distinguish which pion goes to K^{*+} or $\overline{K}^{*0}$ exactly. This is the reason we plot two K^{*+} and $\overline{K}^{*0}$.

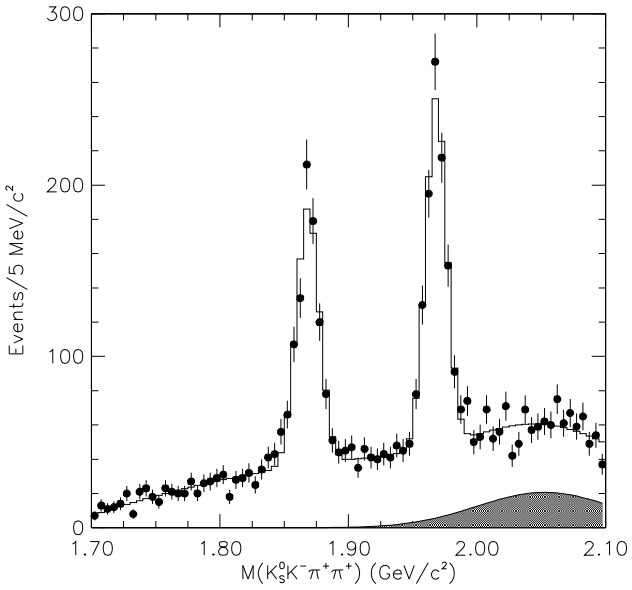

Figure 4.10: The invariant mass distributions of $K^0_S K^-\pi^+\pi^+$ with D^+ selection cuts. The data are indicated by points with error bars and the solid lines are the fits. The shadowed regions are charm reflection backgrounds.

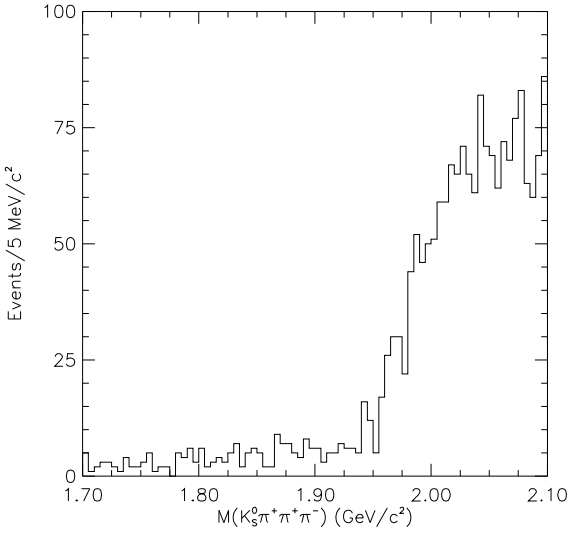

Figure 4.11: Charm reflection background in $D^+ \to K^0_S K^-\pi^+\pi^+$ from Monte Carlo simulation.

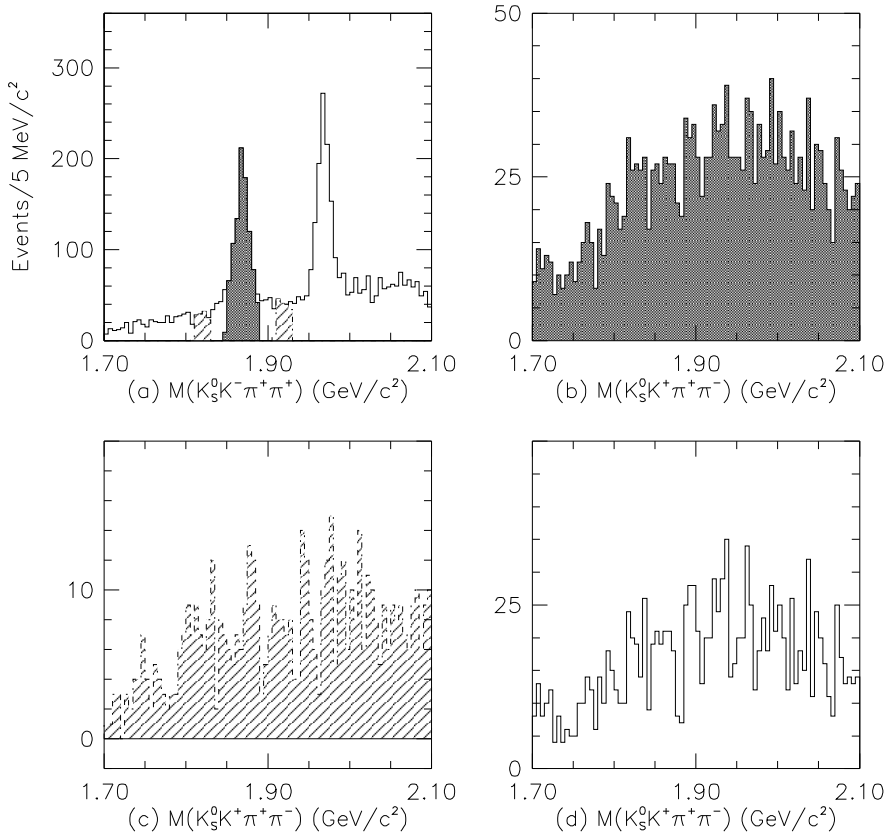

Figure 4.12: (a) is $M(K^0_S K^-\pi^+\pi^+)$. Shadowed is 2.5σ of signal region and hatched is sideband region. (b) is $M(K^0_S K^+\pi^+\pi^-)$ within $M(K^0_S K^-\pi^+\pi^+)$ signal region. (c) is $M(K^0_S K^+\pi^+\pi^-)$ within $M(K^0_S K^-\pi^+\pi^+)$ sideband region. (d) is sideband subtracted $M(K^0_S K^+\pi^+\pi^-)$ distribution in the $D^+ \to K^0_S K^-\pi^+\pi^+$ signal region.

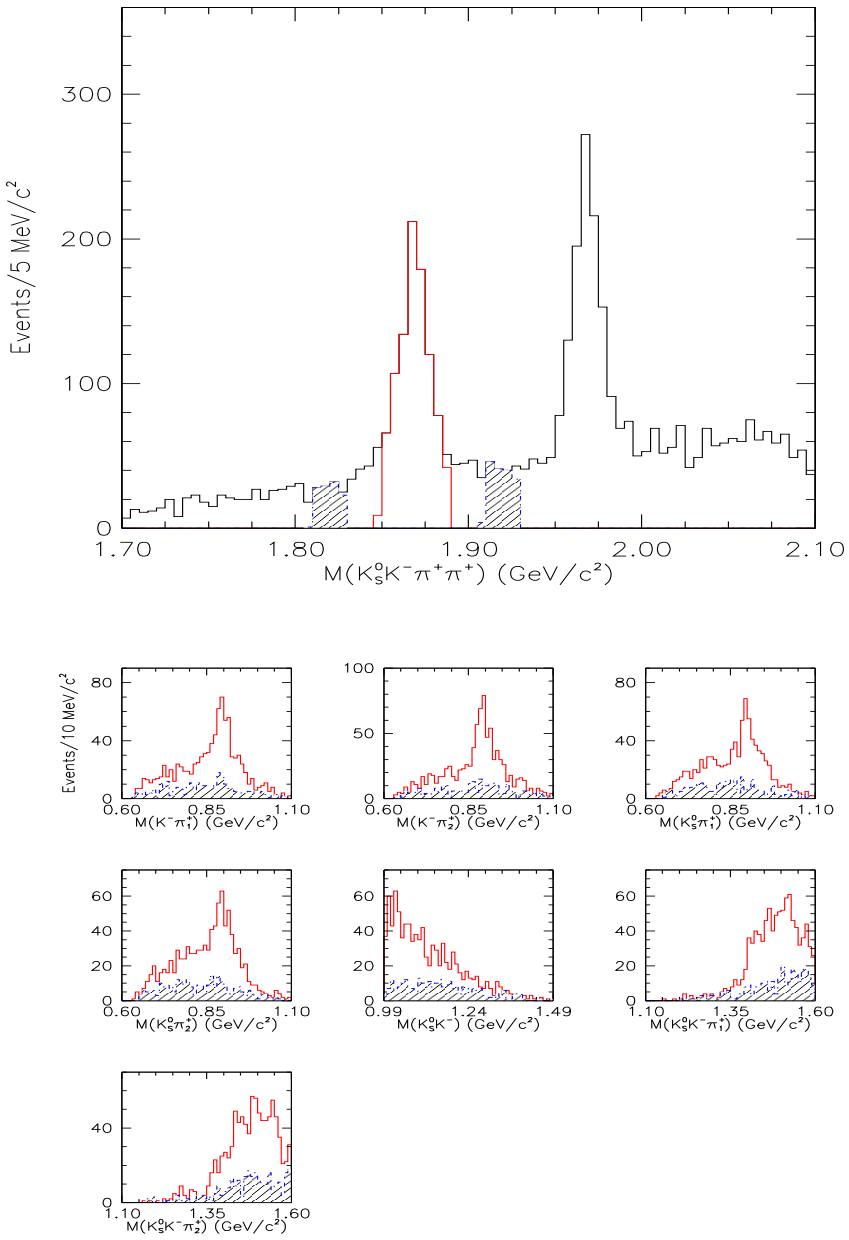

Figure 4.13: Resonant states in the $D^+ \to K^0_S K^- \pi^+ \pi^+$ final state. There is no condition for nomenclature of π^+_1 and π^+_2.

dominant contribution to this final state is $K^{*+}\overline{K}^{*0}$ and used this efficiency as final state efficiency. We have estimated systematics from efficiency difference among resonant states by taking 50% difference between dominant decay mode and decay mode that has biggest difference with dominant decay mode. For this decay mode we estimate systematic error from resonant efficiency is 3.9%. Using Eq. 4.1, we measured relative branching ratio of $\Gamma(D^+ \to K^0_S K^-\pi^+\pi^+)/\Gamma(D^+ \to K^0_S\pi^+\pi^+\pi^-)$ to be:

$$\frac{\Gamma(D^+ \to K^0_S K^-\pi^+\pi^+)}{\Gamma(D^+ \to K^0_S\pi^+\pi^+\pi^-)} \;=\; 0.0768 \pm 0.0041. \tag{4.4}$$

A detailed study of the stability and behavior for branching ratio was performed using variation of our analysis cuts. Fig. 4.14 (a) shows the variation of relative branching ratio through overall cut variable range with several cut combinations. We saw no bias from the choice of analysis cuts. Further we estimate the systematics in this relative branching ratio using the formalisms referred in Appendix A. First, we split our data into following categories:

- 1996 run and D momentum < 75 GeV/c
- 1997 run and D momentum < 75 GeV/c
- 1996 run and D momentum > 75 GeV/c
- 1997 run and D momentum > 75 GeV/c

As shown in Fig. 4.14 (b), we found no systematic uncertainty from splitting our data. In addition to the split sample systematics, we consider the systematics in the fitting procedures which include the binning effects and fitting methods and background parameterizations. We chose the χ^2 fit and quadratic background with other charm reflection as a reference fit procedure with the bin size of 5.0 MeV/c^2. Fig. 4.14 (c) shows the resulting relative branching ratio from the different fitting procedures. We estimated systematic error for fit variant 0.009 in this relative branching ratio measurement. Finally, we determined our final result of the relative branching ratio of $\Gamma(D^+ \to K^0_S K^-\pi^+\pi^+)/\Gamma(D^+ \to K^0_S\pi^+\pi^+\pi^-)$ to be:

$$\frac{\Gamma(D^+ \to K^0_S K^-\pi^+\pi^+)}{\Gamma(D^+ \to K^0_S\pi^+\pi^+\pi^-)} \;=\; 0.0768 \pm 0.0041 \pm 0.0032 \tag{4.5}$$

and summarized systematic contributions in Table 4.5.

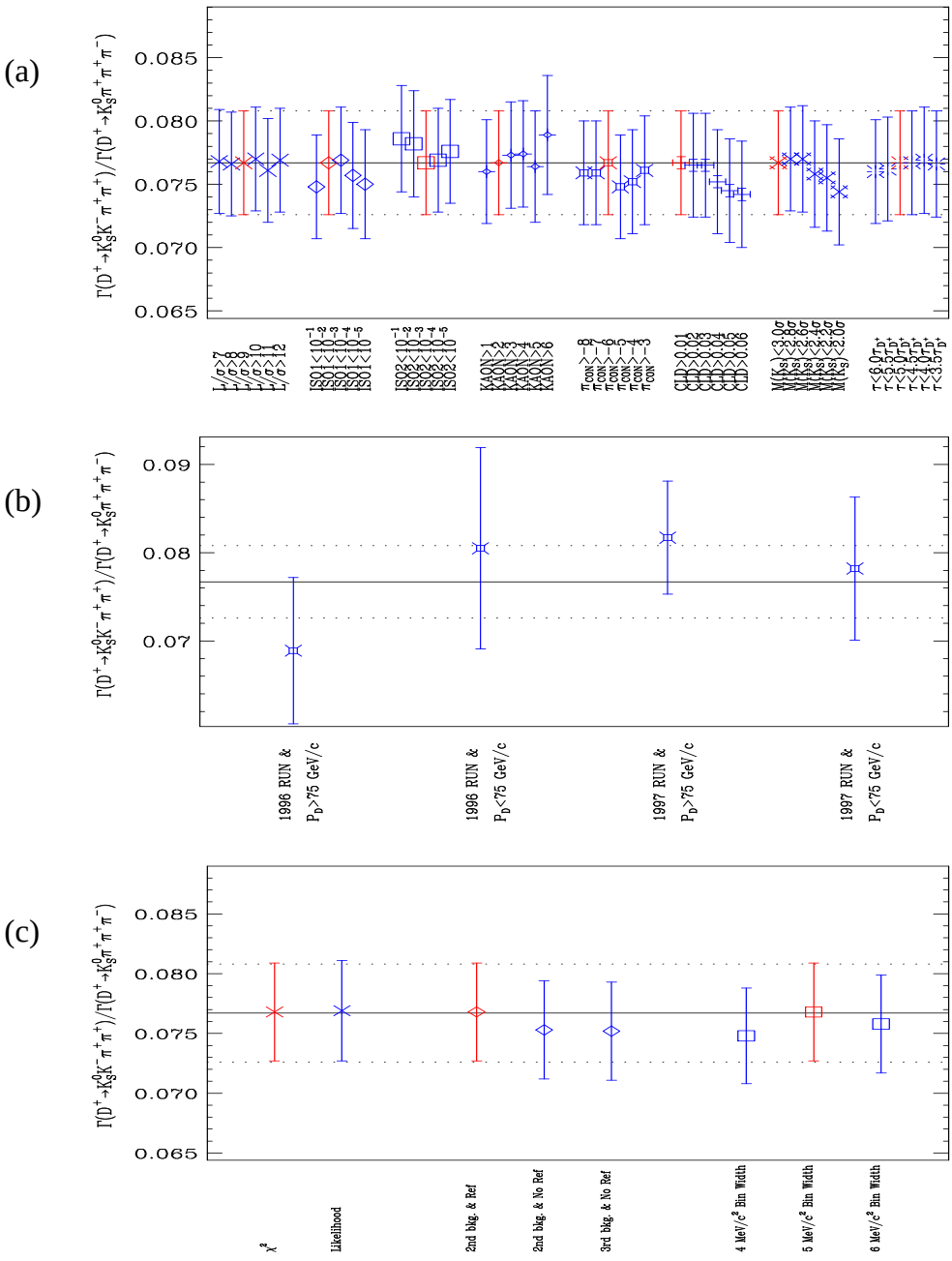

Figure 4.14: Systematics for $D^+ \to K^0_S K^- \pi^+ \pi^+$. (a) is relative branching ratios for cut variants, (b) is relative branching ratios for split sample and (c) is relative branching ratio for fit variants.

Source of error	$\delta_{\Gamma_{\rm rel}}$
$\mathcal{E}$ from resonant state	0.0030
$\mathcal{E}$ from MC statistics	0.0006
Cut variants	0.
Split sample	0.
Fit variants	0.0009
Total	0.0032

Table 4.5: Summary of systematic errors for the $\Gamma(D^+ \to K^0_S K^-\pi^+\pi^+)/\Gamma(D^+ \to K^0_S\pi^+\pi^+\pi^-)$.

4.3.3 $D^+ \to K^0_S K^+\pi^+\pi^-$

Decay Channels	$\mathcal{E}$ (%)
Non R. $\mathbf{K^0_S K^+\pi^+\pi^-}$	**1.144±0.010**
$\overline{K}^0_1(1400)(K^{*-}(K^0_S\pi^-)\pi^+)K^+$	0.990±0.010
$K^+_1(1400)(K^{*0}(K^+\pi^-)\pi^+)K^0_S$	1.207±0.011
$\overline{K}^0_1(1270)(K^0_S\rho^0(\pi^+\pi^-))K^+$	1.131±0.010
$K^+_1(1270)(K^+\rho^0(\pi^+\pi^-))K^0_S$	1.105±0.010
$a^+(K^0_S K^+)\rho^0(\pi^+\pi^-)$	1.011±0.010
$a^+(K^0_S K^+)\pi^+\pi^-$	1.085±0.010
$K^0_S K^{*0}(K^+\pi^-)\pi^+$	1.136±0.010
$K^0_S K^+\rho^0(\pi^+\pi^-)$	1.030±0.010
$K^{*-}(K^0_S\pi^-)K^+\pi^+$	1.149±0.010

Table 4.6: Possible decay channels in $D^+ \to K^0_S K^+\pi^+\pi^-$ final state and its efficiencies. $\mathcal{E}$s' do not include $\Gamma(K^0_S \to \pi^+\pi^-)$ and branching ratio of other resonance particles, and its error is Monte Carlo statistical error.

Though this final state has same decay topology with $D^+ \to K^0_S K^-\pi^+\pi^+$ decay mode, their intermediate states are totally different. Therefore, we do not expect branching ratio of this decay mode is same with $D^+ \to K^0_S K^-\pi^+\pi^+$ decay mode. With our selection cuts, we have obtained 469±32 events and Fig. 4.15 shows

this final state. We investigated $\Lambda_c^+ \to K_S^0 p\pi^+\pi^-$ contamination in the signal region. We found no evidence in the data for any enhancement due to $\Lambda_c^+ \to K_S^0 p\pi^+\pi^-$ where the p is misidentified as a K (see Fig. 4.17). We also studied double misidentification of the $D^+ \to K_S^0 K^+\pi^+\pi^-$ to the $D^+ \to K_S^0 K^-\pi^+\pi^+$ decay mode and found to be negligible (see Fig. 4.18). We parameterized signal by a Gaussian and background by quadratic polynomial and charm reflection. Monte Carlo simulation, shown in Fig. 4.16, shows this reflection mainly comes from $D^+ \to K_S^0\pi^+\pi^+\pi^-$ channel due to π/K misidentification. Reflection background shape is determined by Monte Carlo simulation and amplitude is a free fit parameter. This state also has different reconstruction efficiencies of resonant states (see Table 4.6).[3] To determine reconstruction efficiency for this decay mode, we investigated possible resonant states, as shown in Fig. 4.19. This decay mode has contributions from many sub-decay modes which could not be distinguished without detailed resonant analysis.[4] Therefore we assumed a non-resonant state efficiency to be the efficiency for this final state. We estimated systematic error from resonant sub-states for this decay mode is 6.7%. Using Eq. 4.1, we measured relative branching ratio of $\Gamma(D^+ \to K_S^0 K^+\pi^+\pi^-)/\Gamma(D^+ \to K_S^0\pi^+\pi^+\pi^-)$ to be:

$$\frac{\Gamma(D^+ \to K_S^0 K^+\pi^+\pi^-)}{\Gamma(D^+ \to K_S^0\pi^+\pi^+\pi^-)} \;=\; 0.0562 \pm 0.0039. \tag{4.6}$$

We stepped same approach with the $D^+ \to K_S^0 K^-\pi^+\pi^+$ to estimate systematic error for this final state. Fig. 4.20 (a) shows its cut variants and Fig. 4.20 (b) is split sample test. Fig. 4.20 (c) is fit variant systematics. We see systematic error from fitting method and estimate systematic error for relative branching ratio is 0.0011. Finally, we determined our final result of the relative branching ratio of $\Gamma(D^+ \to K_S^0 K^+\pi^+\pi^-)/\Gamma(D^+ \to K_S^0\pi^+\pi^+\pi^-)$ to be:

$$\frac{\Gamma(D^+ \to K_S^0 K^+\pi^+\pi^-)}{\Gamma(D^+ \to K_S^0\pi^+\pi^+\pi^-)} \;=\; 0.0562 \pm 0.0039 \pm 0.0040 \tag{4.7}$$

and summarized systematic contributions in Table 4.7.

[3] We do not consider all of decay mode

[4] This may be a future analysis

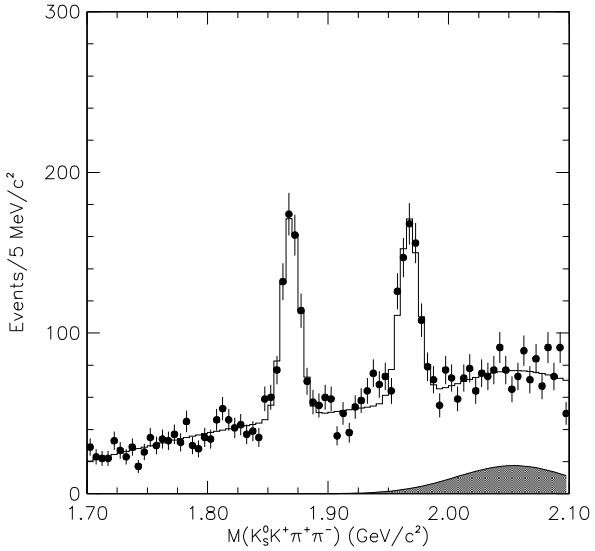

Figure 4.15: The invariant mass distribution of $K^0_S K^+\pi^+\pi^-$ with D^+ selection cuts. The data are indicated by points with error bars and the solid lines are the fits. The shadowed regions are charm reflection backgrounds.

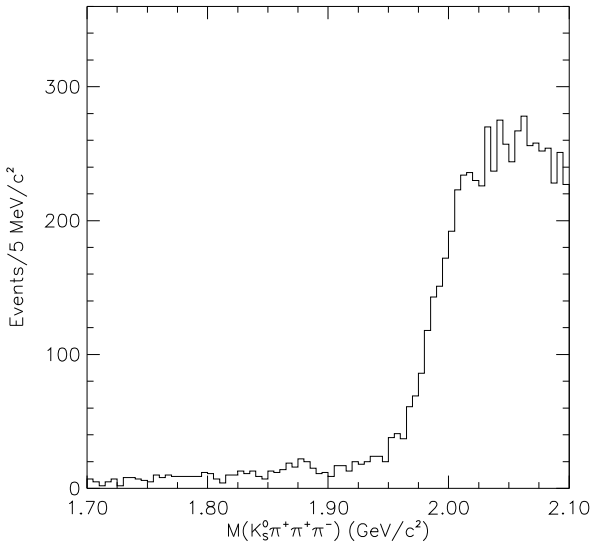

Figure 4.16: Charm reflection background in $D^+ \to K^0_S K^+\pi^+\pi^-$ from Monte Carlo simulation.

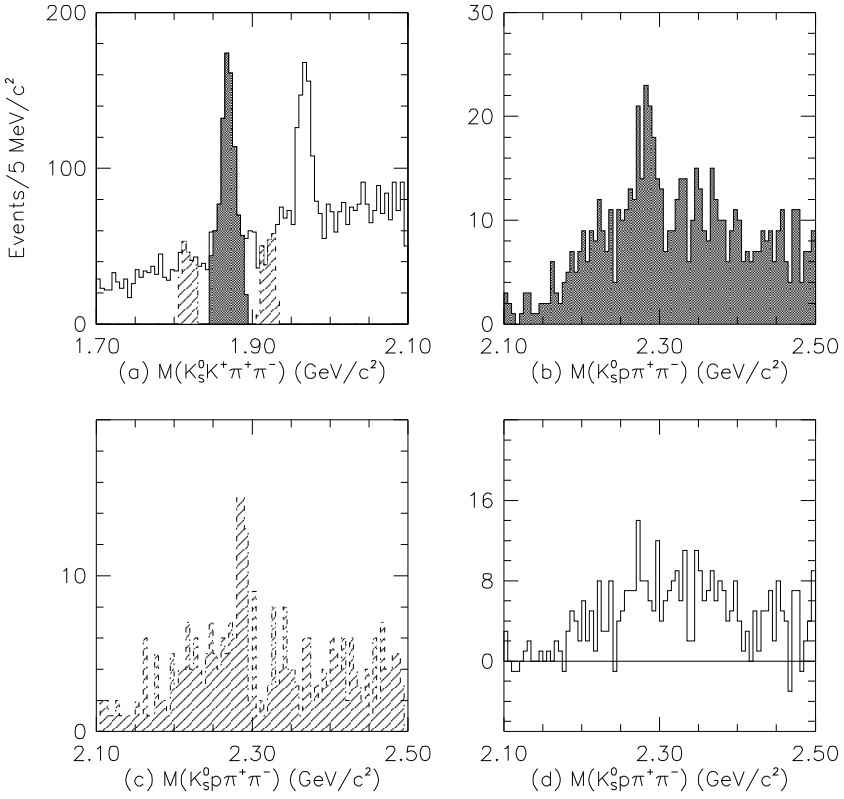

Figure 4.17: (a) is $M(K^0_S K^+\pi^+\pi^-)$. Shadowed is 2.5σ of signal region and hatched is sideband region. (b) is $M(K^0_S p\pi^+\pi^-)$ within $M(K^0_S K^+\pi^+\pi^-)$ signal region. (c) is $M(K^0_S p\pi^+\pi^-)$ within $M(K^0_S K^+\pi^+\pi^-)$ sideband region. (d) is sideband subtracted $M(K^0_S p\pi^+\pi^-)$ distribution in the $D^+ \to K^0_S K^+\pi^+\pi^-$ signal region.

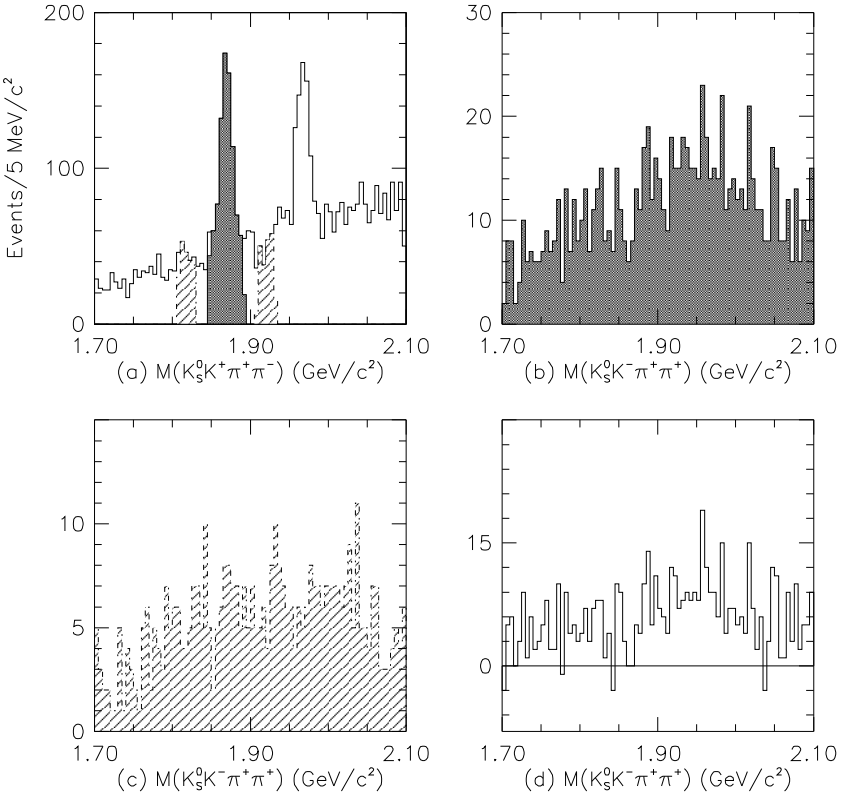

Figure 4.18: (a) is $M(K^0_S K^+\pi^+\pi^-)$. Shadowed is 2.5σ of signal region and hatched is sideband region. (b) is $M(K^0_S K^-\pi^+\pi^+)$ within $M(K^0_S K^+\pi^+\pi^-)$ signal region. (c) is $M(K^0_S K^-\pi^+\pi^+)$ within $M(K^0_S K^+\pi^+\pi^-)$ sideband region. (d) is sideband subtracted $M(K^0_S K^-\pi^+\pi^+)$ distribution in the $D^+ \to K^0_S K^+\pi^+\pi^-$ signal region.

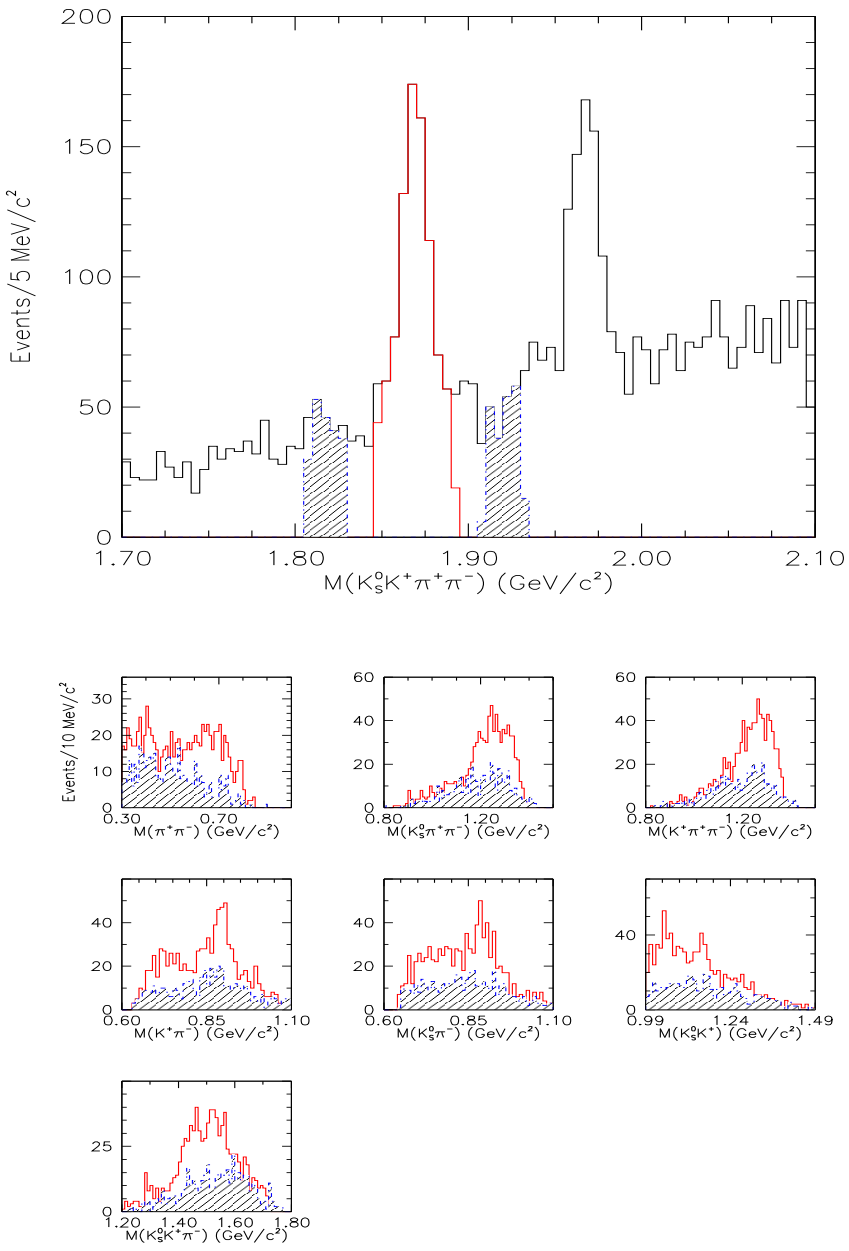

Figure 4.19: Resonant states in the $D^+ \to K^0_S K^+\pi^+\pi^-$ final state.

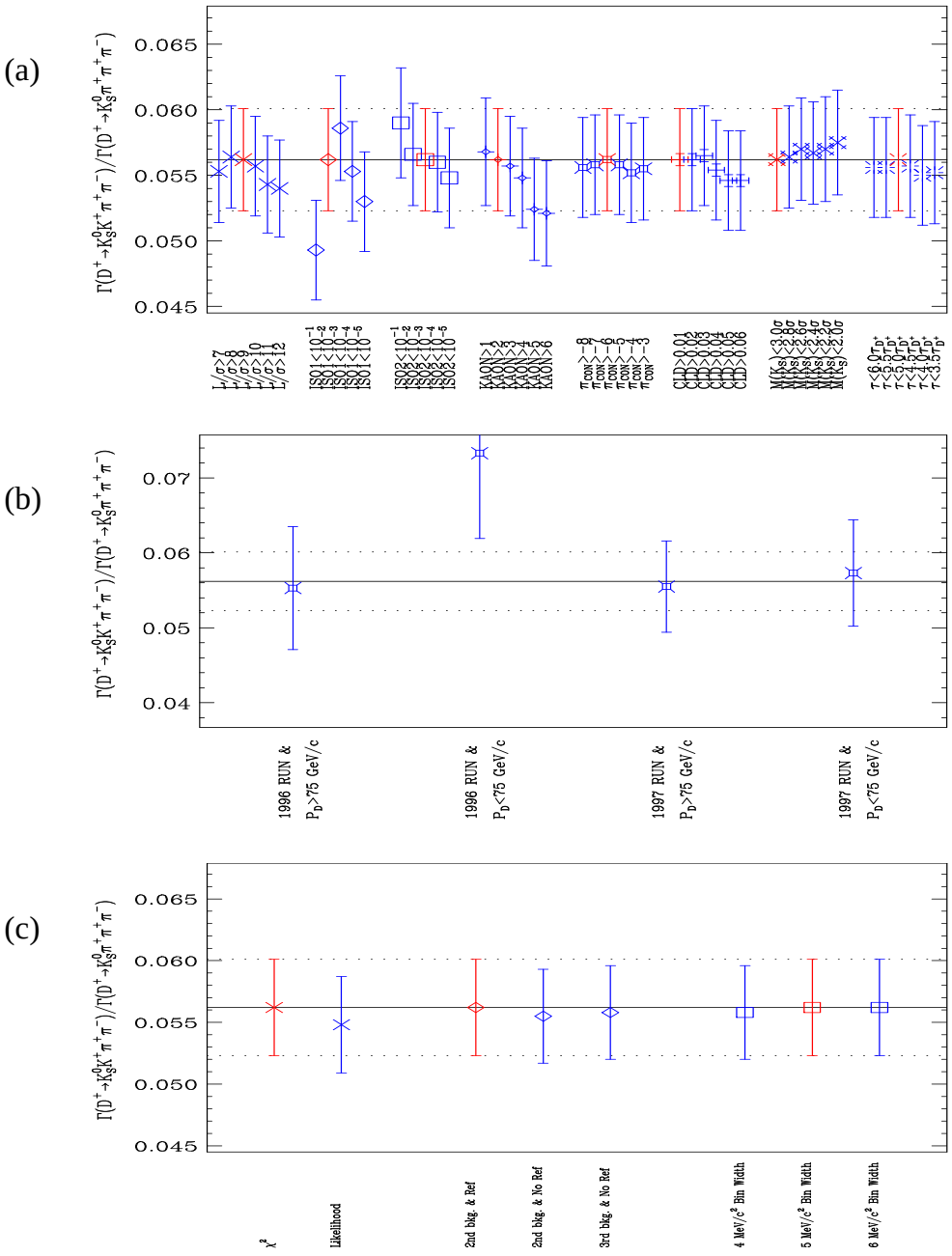

Figure 4.20: Systematics for $D^+ \to K^0_S K^+\pi^+\pi^-$. (a) is relative branching ratios for cut variants, (b) is relative branching ratios for split sample and (c) is relative branching ratio for fit variants.

Source of error	$\delta_{\Gamma_{\rm rel}}$
$\mathcal{E}$ from resonant state	0.0038
$\mathcal{E}$ from MC statistics	0.0005
Cut variants	0.
Split sample	0.
Fit variants	0.0011
Total	0.0040

Table 4.7: Summary of systematic errors for the $\Gamma(D^+ \to K^0_S K^+\pi^+\pi^-)/\Gamma(D^+ \to K^0_S\pi^+\pi^+\pi^-)$.

4.3.4 $D^+ \to K^0_S K^+ K^-\pi^+$

This decay mode is Cabibbo favored, but strongly suppressed by its small phase space. In addition, this decay requires the production of at least one extra quark-antiquark pair, an $s\bar{s}$, either from vacuum or via final state interactions. This final state is shown in Fig. 4.21. We parameterized signal by a Gaussian and background by quadratic polynomial and charm reflection. Monte Carlo simulation, shown in Fig. 4.22, shows this reflection mainly comes from $D^+ \to K^0_S K^-\pi^+\pi^+$ and $D^+ \to K^0_S K^+\pi^+\pi^-$ channels due to π/K misidentification. Reflection background shape is determined by Monte Carlo simulation and amplitude is a free fit parameter. We have obtained 35$\pm$7 events for this decay mode. If π/K misidentification occurred in $D^+_s \to K^0_S K^-\pi^+\pi^+$ and $D^+_s \to K^0_S K^+\pi^+\pi^-$ decay modes, backgrounds from these decay modes would be out of mass window, from 1.7 GeV/c^2 to 2.1 GeV/c^2. The same procedure is adopted in case of $D^+ \to K^0_S\pi^+\pi^+\pi^-$ decay background from double misidentification. Our particle identification cuts for this decay mode do not make any particle misidentification backgrounds in the signal region. Table 4.8 shows its resonant states efficiency. From Fig. 4.23 we could see dominant contribution to this final state is $K^0_S\phi\pi^+$ mode. We estimate systematic error from resonant states efficiency is 9.8%. We do not see any systematic bias by varying our analysis cuts (see Fig. 4.24 (a)). Due to its small statistics, we could not split sample by method in previous section. Instead, we split our $D^+ \to K^0_S K^+ K^-\pi^+$ sample into n splits and then add the errors obtained that

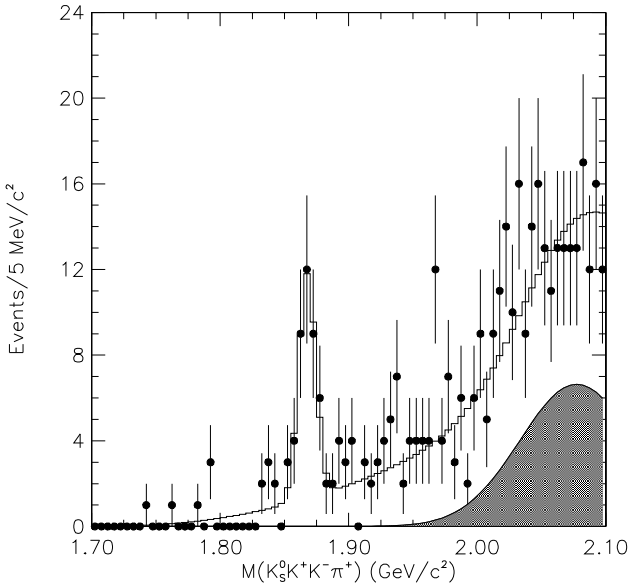

Figure 4.21: The invariant mass distribution of $K^0_S K^+ K^- \pi^+$ with D^+ selection cuts. The data are indicated by points with error bars and the solid lines are the fits. The shadowed regions are charm reflection backgrounds.

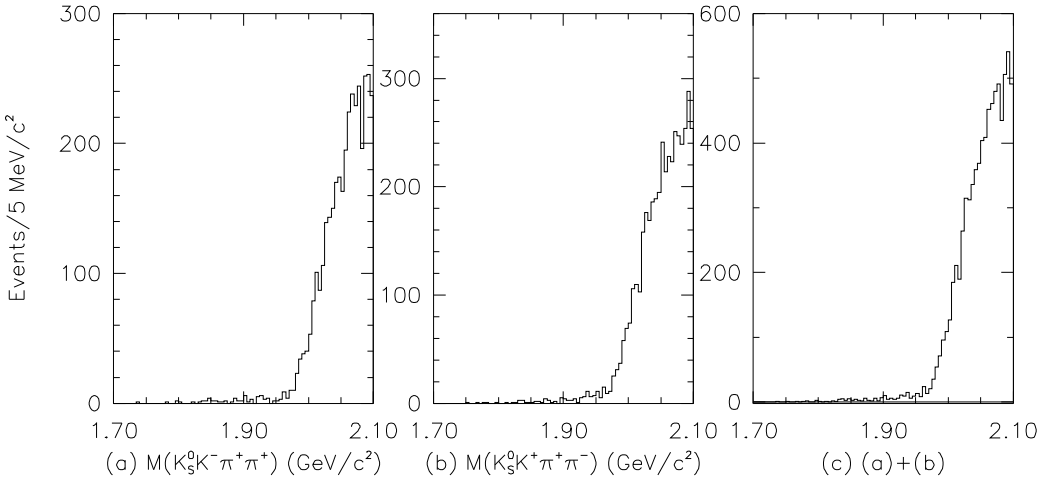

Figure 4.22: Charm reflection background in $D^+ \to K^0_S K^+ K^- \pi^+$ from Monte Carlo simulation. (a) is from $D^+ \to K^0_S K^- \pi^+ \pi^+$, (b) from $D^+ \to K^0_S K^+ \pi^+ \pi^-$ and (c) is sum of two reflections.

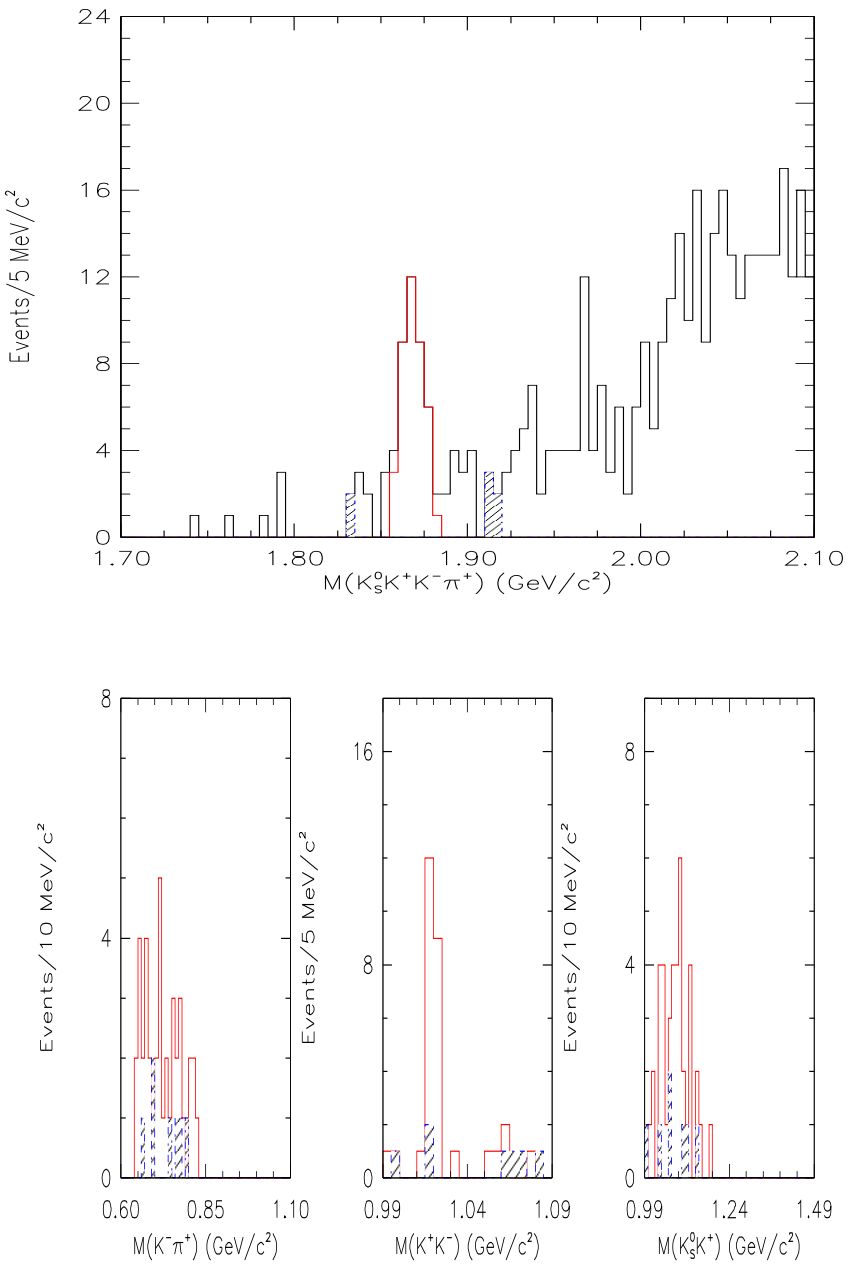

Figure 4.23: Resonant states in the $D^+ \to K^0_S K^+ K^- \pi^+$ final state.

Decay Channels	$\mathcal{E}$ (%)
$Non\ R.\ K^0_S K^+ K^- \pi^+$	0.723±0.008
$a^+(K^0_S K^+)\overline{K}^{*0}(K^-\pi^+)$	0.629±0.008
$\mathbf{K^0_S \phi^0 (K^+ K^-)\pi^+}$	**0.624±0.008**
$K^0_S K^+ \overline{K}^{*0}(K^-\pi^+)$	0.502±0.007
$a^+(K^0_S K^+)K^-\pi^+$	0.725±0.008

Table 4.8: Possible decay channels in $D^+ \to K^0_S K^+ K^- \pi^+$ final state and its efficiencies. $\mathcal{E}$s' do not include $\Gamma(K^0_S \to \pi^+\pi^-)$ and branching ratio of other resonance particles, and its error is Monte Carlo statistical error.

way in quadrature if we found systematic errors [35].[5] So, we split our data into following categories:

- 1996 run
- 1997 run
- D momentum < 80 GeV/c
- D momentum > 80 GeV/c

We found no systematic error from this split sample systematics as shown in Fig. 4.24 (b). Fig. 4.24 (c) is fit variant systematics. We estimated systematic error for relative branching ratio from fit variant is 0.0005. In $D^+ \to K^0_S K^- \pi^+ \pi^+$ and $D^+ \to K^0_S K^+ \pi^+ \pi^-$ decay modes, systematic errors from fit variants comes from background parameterization dominantly, while systematic error from fit variants mainly comes from fitting method itself due to its small statistics.[6] Finally, we determined our final result of the relative branching ratio of $\Gamma(D^+ \to K^0_S K^+ K^- \pi^+)/\Gamma(D^+ \to K^0_S \pi^+ \pi^+ \pi^-)$ to be:

$$\frac{\Gamma(D^+ \to K^0_S K^+ K^- \pi^+)}{\Gamma(D^+ \to K^0_S \pi^+ \pi^+ \pi^-)} \;=\; 0.0077 \pm 0.0015 \pm 0.0009 \qquad (4.8)$$

and summarized systematic contributions in Table 4.9.

[5] Basically, we should split sample into 2^n independent subsamples.

[6] χ^2 fit vs. Likelihood fit

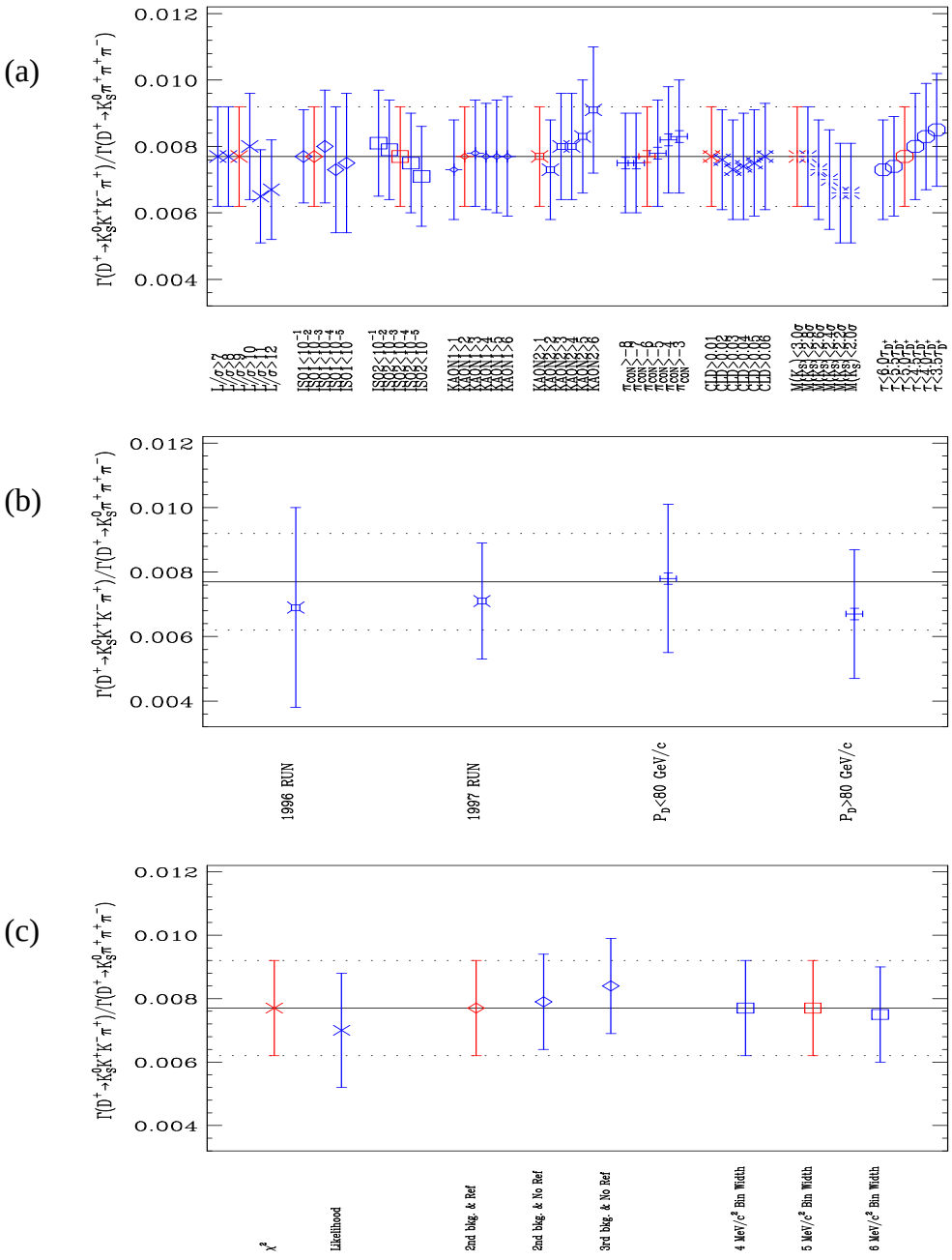

Figure 4.24: Systematics for $D^+ \to K^0_S K^+ K^- \pi^+$. (a) is relative branching ratios for cut variants, (b) is relative branching ratios for split sample and (c) is relative branching ratio for fit variants.

Source of error	$\delta_{\Gamma_{\rm rel}}$
$\mathcal{E}$ from resonant state	0.0008
$\mathcal{E}$ from MC statistics	0.0001
Cut variants	0.
Split sample	0.
Fit variants	0.0005
Total	0.0009

Table 4.9: Summary of systematic errors for the $\Gamma(D^+ \to K^0_S K^+ K^- \pi^+)/\Gamma(D^+ \to K^0_S \pi^+ \pi^+ \pi^-)$.

4.4 Branching Ratio Measurements of D_s^+ Channels

4.4.1 $D_s^+ \to K_S^0 K^- \pi^+ \pi^+$

Decay Channels	$\mathcal{E}$ (%)
Non R. $K_S^0 K^- \pi^+ \pi^+$	0.670±0.008
$K^{*+}(K_S^0\pi^+)K^-\pi^+$	0.682±0.008
$K_S^0\overline{K}^{*0}(K^-\pi^+)\pi^+$	0.663±0.008
$\mathbf{K^{*+}(K_S^0\pi^+)\overline{K}^{*0}(K^-\pi^+)}$	**0.679±0.008**
$a^-(K_S^0K^-)\pi^+\pi^+$	0.617±0.008

Table 4.10: Possible decay channels in $D_s^+ \to K_S^0 K^- \pi^+ \pi^+$ final state and its efficiencies. $\mathcal{E}$s' do not include $\Gamma(K_S^0 \to \pi^+\pi^-)$ and branching ratio of other resonance particles, and its error is Monte Carlo statistical error.

With slightly different cuts from $D^+ \to K_S^0 K^- \pi^+ \pi^+$, we have obtained this final state and it is shown in Fig. 4.25. We parameterized signal by a Gaussian and background by quadratic polynomial and charm reflection. Monte Carlo simulation, shown in Fig. 4.26, shows this reflection mainly comes from $D^+ \to K_S^0 \pi^+ \pi^+ \pi^-$ channel due to π/K misidentification. Reflection background shape is determined by Monte Carlo simulation and amplitude is a free fit parameter. We have obtained 837±38 events for this final state. We investigated double misidentification from $K_S^0 K^+ \pi^+ \pi^-$ state. Fig 4.27 shows no double misidentification from $K_S^0 K^+ \pi^+ \pi^-$ final state. Table 4.10 shows its resonant and non-resonant state reconstruction efficiencies. We determined dominant contribution to this final state is $K^{*+}\overline{K}^{*0}$ and used this efficiency as a final state efficiency (see Fig 4.28). For this decay mode we estimate systematic error from resonant efficiency is 4.6%. This decay mode is used to normalization mode for $D_s^+ \to K_S^0 K^+ \pi^+ \pi^-$ decay mode which will be described in the next section.

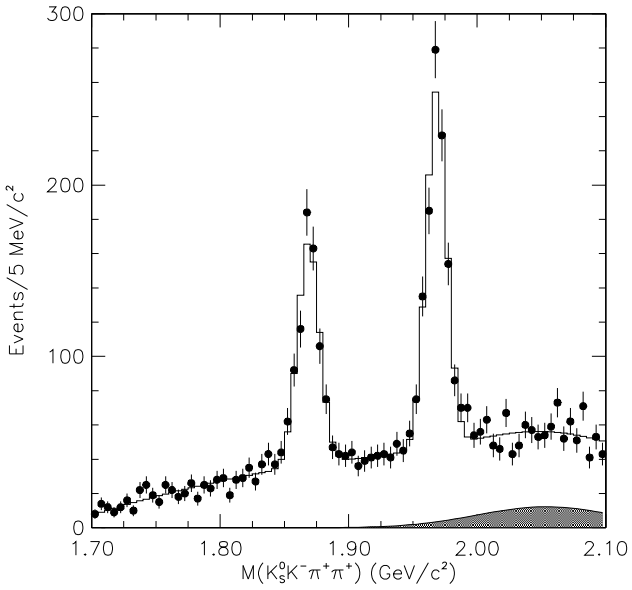

Figure 4.25: The invariant mass distribution of $K_S^0K^-\pi^+\pi^+$ with D_s^+ selection cuts. The data are indicated by points with error bars and the solid lines are the fits. The shadowed regions are charm reflection backgrounds.

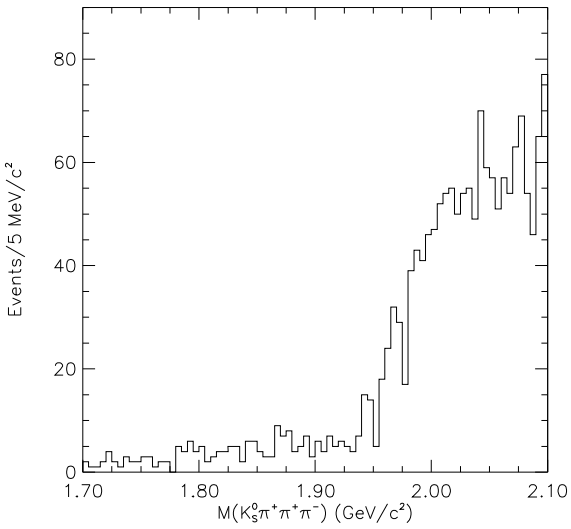

Figure 4.26: Charm reflection background in $D_s^+ \to K_S^0K^-\pi^+\pi^+$ from Monte Carlo simulation.

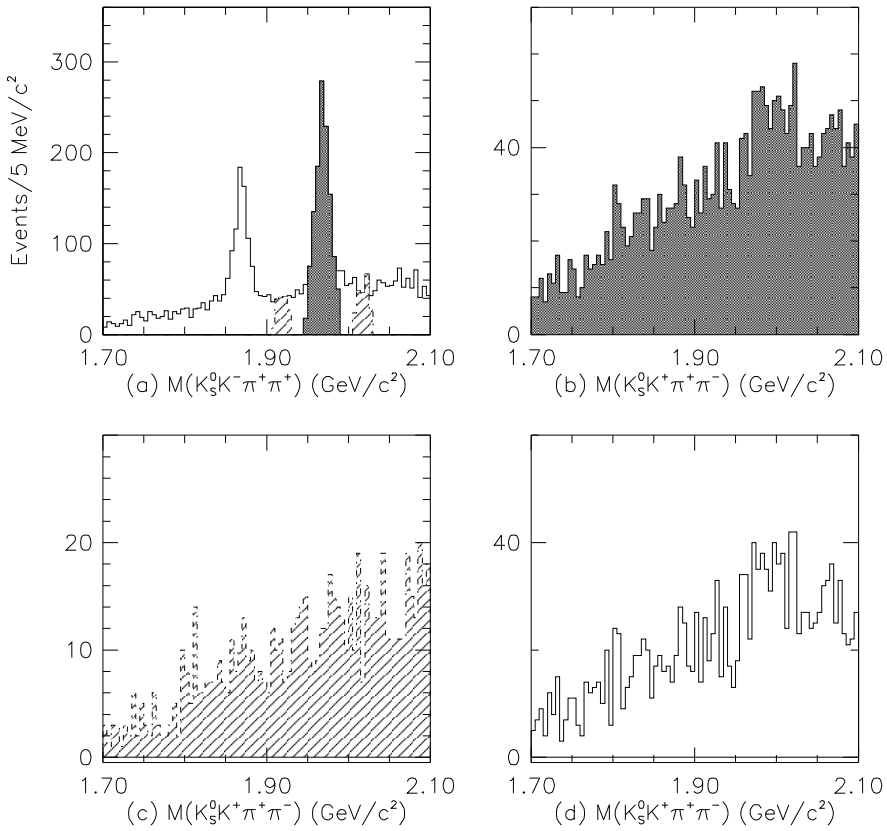

Figure 4.27: (a) is $M(K^0_S K^-\pi^+\pi^+)$. Shadowed is 2.5σ of signal region and hatched is sideband region. (b) is $M(K^0_S K^+\pi^+\pi^-)$ within $M(K^0_S K^-\pi^+\pi^+)$ signal region. (c) is $M(K^0_S K^+\pi^+\pi^-)$ within $M(K^0_S K^-\pi^+\pi^+)$ sideband region. (d) is sideband subtracted $M(K^0_S K^+\pi^+\pi^-)$ distribution in the $D_s^+ \to K^0_S K^-\pi^+\pi^+$ signal region.

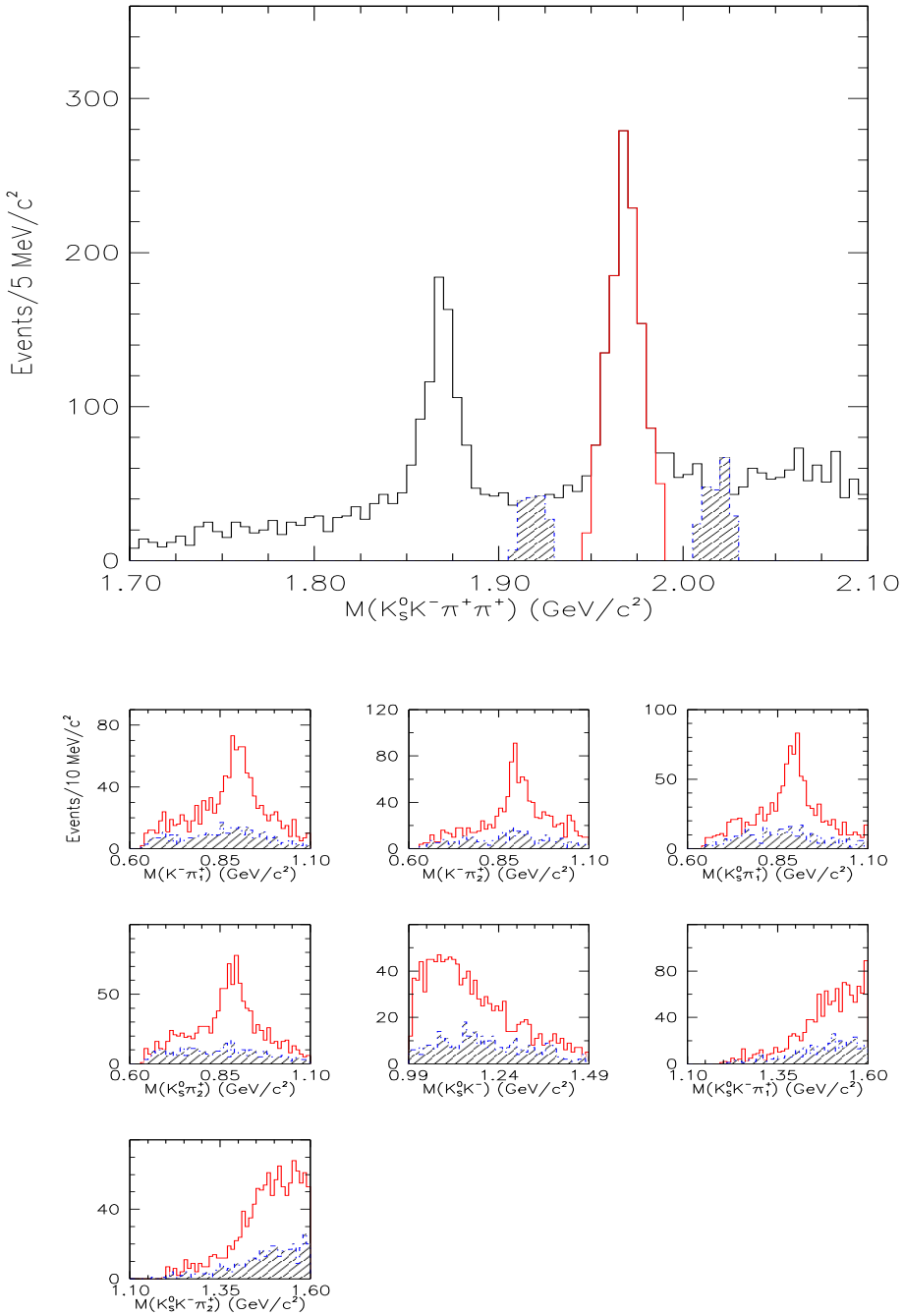

Figure 4.28: Resonant states in the $D_s^+ \to K_S^0 K^- \pi^+ \pi^+$ final state. There is no condition for nomenclature of π_1^+ and π_2^+.

4.4.2 $D_s^+ \to K_S^0 K^+\pi^+\pi^-$

Decay Channels	$\mathcal{E}$ (%)
Non R. $\mathbf{K_S^0 K^+\pi^+\pi^-}$	**0.659±0.008**
$\overline{K}_1^0(1400)(K^{*-}(K_S^0\pi^-)\pi^+)K^+$	0.612±0.008
$K_1^+(1400)(K^{*0}(K^+\pi^-)\pi^+)K_S^0$	0.695±0.008
$\overline{K}_1^0(1270)(K_S^0\rho^0(\pi^+\pi^-))K^+$	0.720±0.008
$K_1^+(1270)(K^+\rho^0(\pi^+\pi^-))K_S^0$	0.627±0.008
$a^+(K_S^0K^+)\rho^0(\pi^+\pi^-)$	0.613±0.008
$a^+(K_S^0K^+)\pi^+\pi^-$	0.635±0.008
$K_S^0K^{*0}(K^+\pi^-)\pi^+$	0.653±0.008
$K_S^0K^+\rho^0(\pi^+\pi^-)$	0.633±0.008
$K^{*-}(K_S^0\pi^-)K^+\pi^+$	0.668±0.008

Table 4.11: Possible decay channels in $D_s^+ \to K_S^0K^+\pi^+\pi^-$ final state and its efficiencies. $\mathcal{E}$s' do not include $\Gamma(K_S^0 \to \pi^+\pi^-)$ and branching ratio of other resonance particles, and its error is Monte Carlo statistical error.

This decay mode has same decay topology with $D_s^+ \to K_S^0K^-\pi^+\pi^+$ but has different intermediate states. As we saw in $D^+ \to K_S^0K^-\pi^+\pi^+$ and $D^+ \to K_S^0K^+\pi^+\pi^-$, we could expect this final state has different decay ratio with $D_s^+ \to K_S^0K^-\pi^+\pi^+$. With our D_s^+ selection cuts, we have obtained 476±36 of $D_s^+ \to K_S^0K^+\pi^+\pi^-$ events. Signal is fitted by a Gaussian and background by quadratic polynomial and charm reflection. Fig. 4.29 shows its invariant mass distribution. Reflection on right side of $D_s^+ \to K_S^0K^+\pi^+\pi^-$ comes from $D^+ \to K_S^0\pi^+\pi^+\pi^-$ due to K/π misidentification. Monte Carlo simulation shows its shape in Fig. 4.30 and the amplitude of reflection background is a free fit parameter. We investigated $\Lambda_c^+ \to K_S^0p\pi^+\pi^-$ contamination in the signal region. We found no evidence in the data for any enhancement due to $\Lambda_c^+ \to K_S^0p\pi^+\pi^-$ where the p is misidentified as a K (see Fig. 4.31). We also studied double misidentification of the $D_s^+ \to K_S^0K^+\pi^+\pi^-$ to the $D_s^+ \to K_S^0K^-\pi^+\pi^+$ decay mode and found to be negligible (see Fig. 4.32).

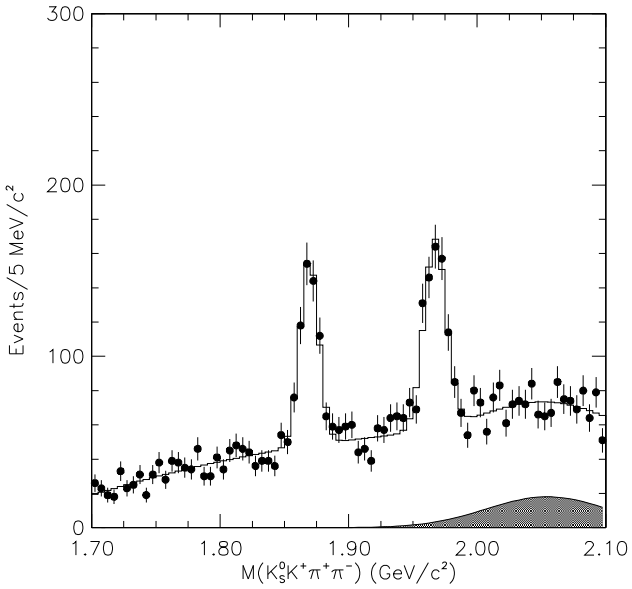

Figure 4.29: The invariant mass distribution of $K_S^0 K^+\pi^+\pi^-$ with D_s^+ selection cuts. The data are indicated by points with error bars and the solid lines are the fits. The shadowed regions are charm reflection backgrounds.

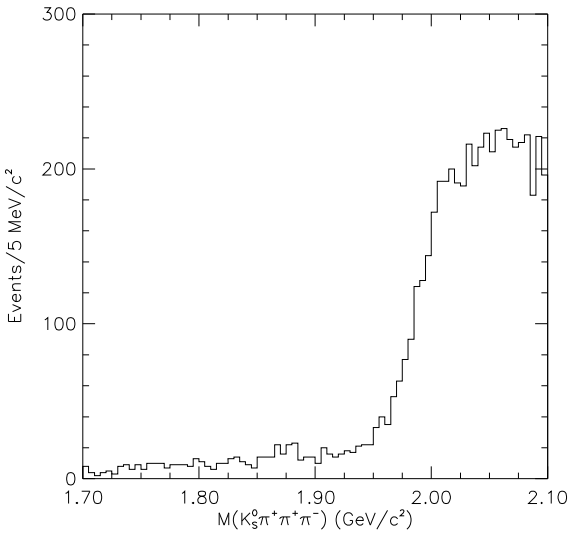

Figure 4.30: Charm reflection background in $D_s^+ \to K_S^0 K^+\pi^+\pi^-$ from Monte Carlo simulation.

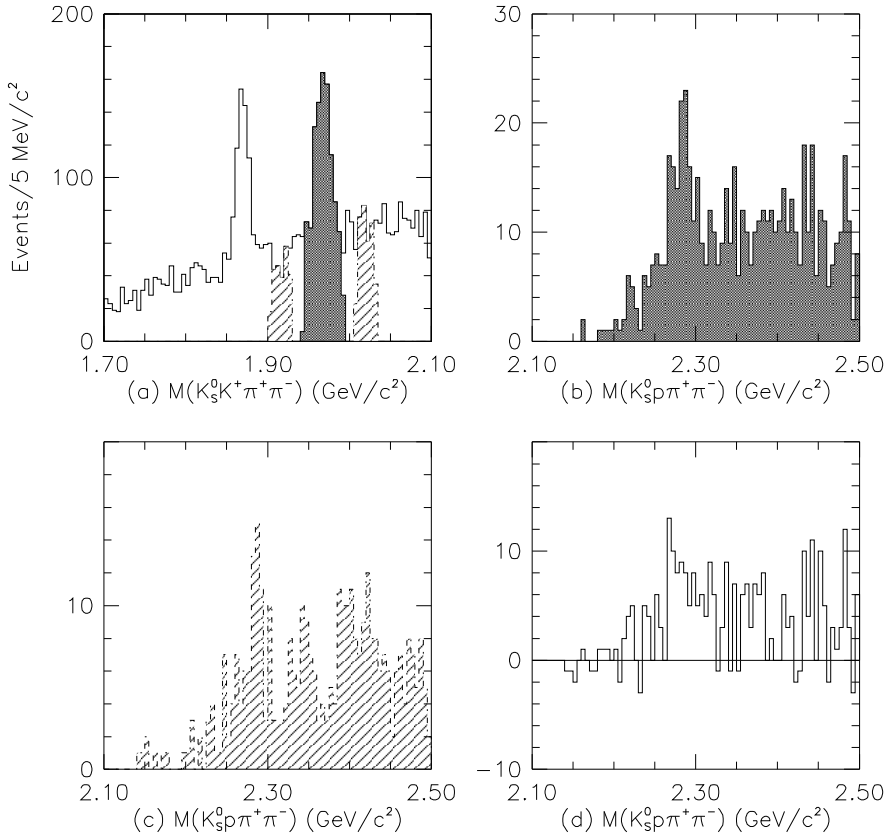

Figure 4.31: (a) is $M(K_S^0K^+\pi^+\pi^-)$. Shadowed is 2.5σ of signal region and hatched is sideband region. (b) is $M(K_S^0p\pi^+\pi^-)$ within $M(K_S^0K^+\pi^+\pi^-)$ signal region. (c) is $M(K_S^0p\pi^+\pi^-)$ within $M(K_S^0K^+\pi^+\pi^-)$ sideband region. (d) is sideband subtracted $M(K_S^0p\pi^+\pi^-)$ distribution in the $D_s^+ \to K_S^0K^+\pi^+\pi^-$ signal region.

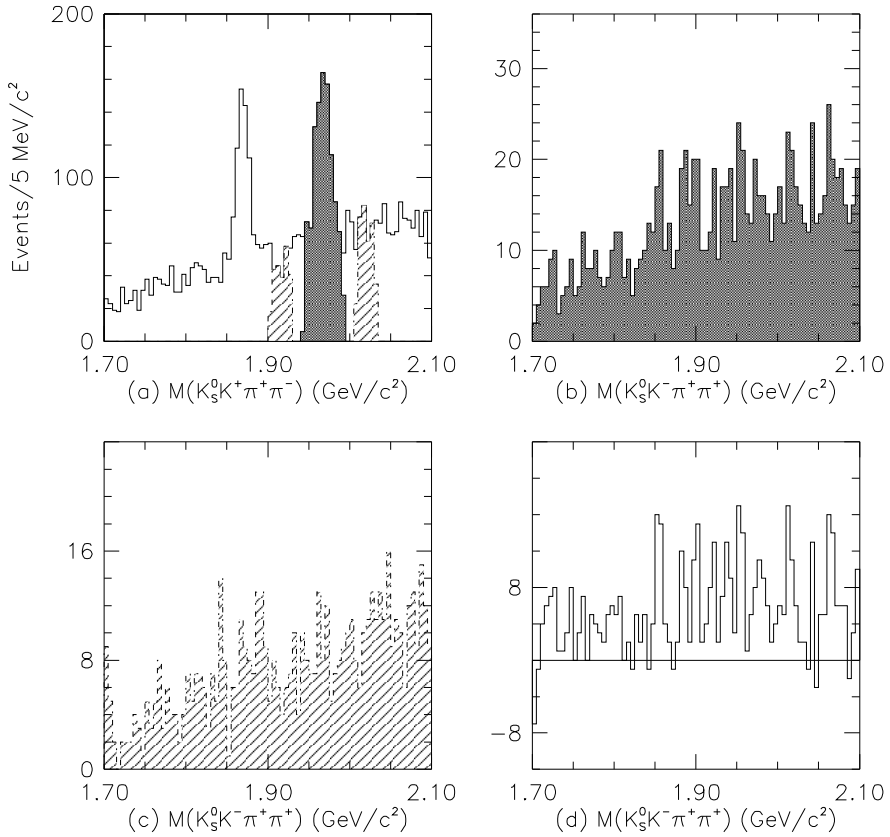

Figure 4.32: (a) is $M(K^0_S K^+\pi^+\pi^-)$. Shadowed is 2.5σ of signal region and hatched is sideband region. (b) is $M(K^0_S K^-\pi^+\pi^+)$ within $M(K^0_S K^+\pi^+\pi^-)$ signal region. (c) is $M(K^0_S K^-\pi^+\pi^+)$ within $M(K^0_S K^+\pi^+\pi^-)$ sideband region. (d) is sideband subtracted $M(K^0_S K^-\pi^+\pi^+)$ distribution in the $D_s^+ \to K^0_S K^+\pi^+\pi^-$ signal region.

To determine reconstruction efficiency for this decay mode, we investigated possible resonant states, as shown in Fig. 4.33, in this final state. This decay mode has contributions from many sub-decay modes which could not be distinguish without detailed resonant analysis like the in case of $D^+ \to K^0_S K^+\pi^+\pi^-$. Therefore we assumed a non-resonant efficiency to be the efficiency for this final state. We estimated systematic error from resonant sub-states for this decay mode is 4.6%. With this reconstruction efficiency, we measured relative branching ratio of $\Gamma(D_s^+ \to K^0_S K^+\pi^+\pi^-)/\Gamma(D_s^+ \to K^0_S K^-\pi^+\pi^+)$ to be:

$$\frac{\Gamma(D_s^+ \to K^0_S K^+\pi^+\pi^-)}{\Gamma(D_s^+ \to K^0_S K^-\pi^+\pi^+)} \;=\; 0.586 \pm 0.052. \tag{4.9}$$

We traced same approach with other decay modes to estimate systematic error for this final state. Fig. 4.34 (a) shows its cut variants and Fig. 4.34 (b) is split sample test. Fig. 4.34 (c) is fit variant systematics. We see systematic error from fitting method and estimate systematic error for relative branching ratio is 0.017. Finally, we determined our final result of the relative branching ratio of $\Gamma(D_s^+ \to K^0_S K^+\pi^+\pi^-)/\Gamma(D_s^+ \to K^0_S K^-\pi^+\pi^+)$ to be:

$$\frac{\Gamma(D_s^+ \to K^0_S K^+\pi^+\pi^-)}{\Gamma(D_s^+ \to K^0_S K^-\pi^+\pi^+)} \;=\; 0.586 \pm 0.052 \pm 0.043 \tag{4.10}$$

and summarized systematic contributions in Table 4.12. Our final systematic error contains systematic error from resonant efficiency from $D_s^+ \to K^0_S K^-\pi^+\pi^+$ final state which is used to normalization mode for this relative branching ratio measurement.

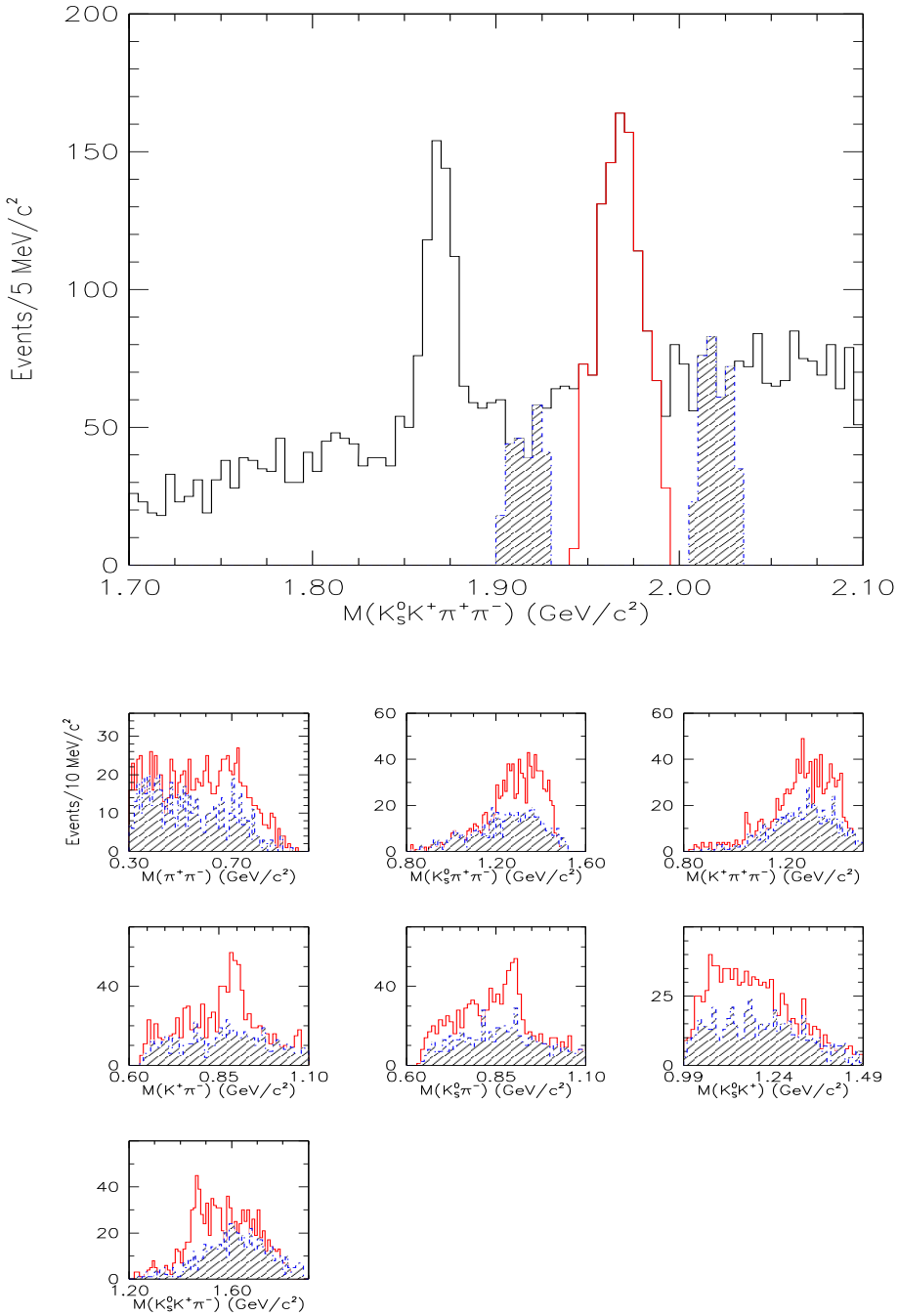

Figure 4.33: Resonant states in the $D_s^+ \to K_S^0 K^+ \pi^+ \pi^-$ final state.

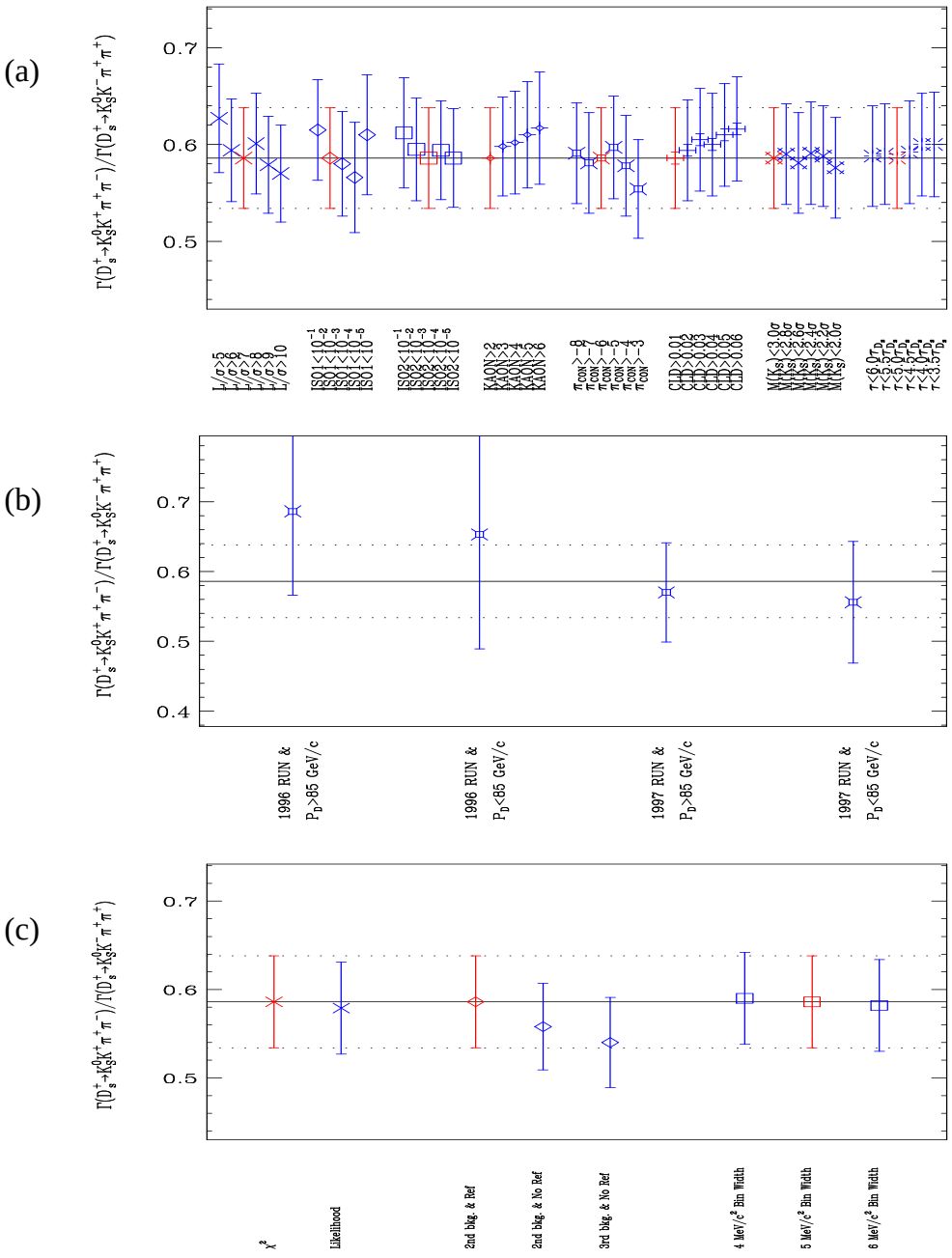

Figure 4.34: Systematics for $D_s^+ \to K_S^0 K^+ \pi^+ \pi^-$. (a) is relative branching ratios for cut variants, (b) is relative branching ratios for split sample and (c) is relative branching ratio for fit variants.

Source of error	$\delta_{\Gamma_{\rm rel}}$
$\mathcal{E}$ from resonant state	0.038
$\mathcal{E}$ from MC statistics	0.010
Cut variants	0.
Split sample	0.
Fit variants	0.017
Total	0.043

Table 4.12: Summary of systematic errors for the $\Gamma(D_s^+ \to K_S^0 K^- \pi^+ \pi^+)/\Gamma(D_s^+ \to K_S^0 K^+ \pi^+ \pi^-)$.

Chapter 5

Conclusion

We have measured new branching ratio of the $D^+ \to K^0_S K^- \pi^+ \pi^+$ relative to the $D^+ \to K^0_S \pi^+ \pi^+ \pi^-$. Although this decay mode is previously reported by other experiment [23], their signal significance is just 2.5σ. We confirmed previous measurement and improved it remarkably. In addition, we have made the first observation of three new decay processes $D^+ \to K^0_S K^+ \pi^+ \pi^-$, $D^+ \to K^0_S K^+ K^- \pi^+$ and $D^+_s \to K^0_S K^+ \pi^+ \pi^-$ and measured their relative branching ratios. We summarize our final results in Table 5.1. We quote the relative efficiency for each decay mode instead of its absolute efficiency. In practice, it is not meaningful to quote the absolute reconstruction efficiency in this thesis since we have measured relative branching ratio. Besides, quoted absolute efficiencies in previous sections are indeed not absolute reconstruction efficiencies since we have imposed K^0_S decays to $\pi^+\pi^-$ with 100% branching ratio. When we quote relative efficiency, the K^0_S reconstruction efficiency is cancelled out and it will be independent of Monte Carlo version. With the assumption that doubly Cabibbo suppressed amplitude is negligible in case of the $D^+ \to K^0_S \pi^+ \pi^+ \pi^-$, $D^+ \to K^0_S K^+ K^- \pi^+$ and $D^+_s \to K^0_S K^+ \pi^+ \pi^-$ and using the current PDG values of the $\Gamma(D^+ \to \overline{K}^0 \pi^+ \pi^+ \pi^-) = (7.0 \pm 0.9)\%$ and $\Gamma(D^+_s \to K^0 K^- \pi^+ \pi^+) = (4.3 \pm 1.5)\%$, we compare our results with previous measurements and summarize them in Table 5.2.[1] We print out total error in Table 5.2 comes from ours and PDGs, where PDGs uncertainty of $\Gamma(D^+ \to \overline{K}^0 \pi^+ \pi^+ \pi^-)$ is

[1] I. I. Bigi points out that interference between Cabibbo favored and doubly Cabibbo suppressed amplitudes, where both occur, could invalidate this assumption by a few percent [39]. Namely, $\Gamma(D \to K^0 \ + \ X)$ is not $2 \cdot \Gamma(D \to K^0_S \ + \ X)$ exactly.

approximately 13% and that of $\Gamma(D_s^+ \to K^0K^-\pi^+\pi^+)$ is about 35%. Finally, these final states have many interesting intermediate states. Future study of amplitude analysis for these final states will give several interesting values and this thesis will be the framework for it.

Decay Mode	$\mathcal{N}_{\rm signal}$	$\mathcal{E}_{\rm rel}$	$\Gamma_{\rm rel}$
$D^+ \to K^0_S K^-\pi^+\pi^+$	670±35	0.753±0.008	0.0768±0.0041±0.0032 †
$D^+ \to K^0_S K^+\pi^+\pi^-$	469±32	0.720±0.008	0.0562±0.0039±0.0040 ‡
$D^+ \to K^0_S K^+K^-\pi^+$	35±7	0.392±0.006	0.0077±0.0015±0.0009 ‡
$D^+ \to K^0_S \pi^+\pi^+\pi^-$	11590±121	1	1
$D_s^+ \to K^0_S K^+\pi^+\pi^-$	476±36	0.971±0.016	0.586±0.052±0.043 ‡
$D_s^+ \to K^0_S K^-\pi^+\pi^+$	837±38	1	1

Table 5.1: Summary of final results. $\mathcal{E}_{\rm rel}$ is the reconstruction efficiency relative to $D^+ \to K^0_S\pi^+\pi^+\pi^-$ for the D^+ modes and $D_s^+ \to K^0_S K^-\pi^+\pi^+$ for the D_s^+ modes, where its error contains Monte Carlo statistical error only. $\Gamma_{\rm rel}$ is the branching ratio relative to $D^+ \to K^0_S\pi^+\pi^+\pi^-$ for the D^+ modes and $D_s^+ \to K^0_S K^-\pi^+\pi^+$ for the D_s^+ modes. Marked mode with † is the world best measurement and modes with ‡ are unseen decay modes previously. The errors on the branching ratios are statistical and systematic, respectively.

Branching Ratio	FOCUS	Others
$\Gamma(D^+ \to K^0K^-\pi^+\pi^+)$	(0.54±0.08)%	(1.0±0.6)% ‡
$\Gamma(D^+ \to \overline{K}^0K^+\pi^+\pi^-)$	(0.39±0.06)%	$<$ 2.0% (@ 90% C.L.) ‡
$\Gamma(D^+ \to \overline{K}^0K^+K^-\pi^+)$	(5.4±1.4)$\times 10^{-4}$	-
$\Gamma(D_s^+ \to \overline{K}^0K^+\pi^+\pi^-)$	(2.5±0.9)%	$<$ 2.8% (@ 90% C.L.) ‡

Table 5.2: Comparison with previous measurement. Marked modes with ‡ are measured by the ARGUS collaboration [23]. The error is combined by quadrature with our total error and PDGs error.

Appendix A

Systematic Error Estimation

Systematic errors in FOCUS measurements are estimated through a combination of the following two methods.

- We estimate systematics by splitting the data sample in two groups and comparing the fit parameters obtained in either half of the split sample. The practical method in *split sample* systematics is to decide how much of the difference in fit parameters is due to statistical fluctuation and how much should be ascribed to systematic error. We use a method for handling this based on the S-factor method which is used by the Particle Data Group.

- We estimate systematic errors by varying reasonable fitting techniques for a complete date set. The trick in *fit variant* systematics is to decide how to extract a meaningful systematic error from the spread if estimates obtained with the various fit variants.

A.1 Split Sample Systematics

As an example, let us say that we are interested in estimating systematics by considering N disjoint samples. If the N independent measurements are statistically consistent, there is no evidence for a *split sample* systematic error. The standard test for statistical consistency is to construct a confidence level for the hypothesis that the N measurements can be fit by a single (weighted average) fit parameter. For N independent samples, the confidence level would be constructed from a χ^2

with $N-1$ degrees of freedom of the form:

$$\chi^2 \;=\; \sum_i^N \frac{(x_i - < x >)^2}{\sigma_i^2}, \tag{A.1}$$

where

$$< x > \;=\; \frac{\sum_i^N x_i/\sigma_i^2}{\sum_i^N 1/\sigma_i^2} \tag{A.2}$$

We can use this χ^2 to extract an estimate of the systematic error in analogy with the S-factor method of the PDG. Let us consider the case where $\chi^2/(N-1) > 1$. We can argue that this inconsistency arises since the split sample true errors are all underestimated due to an unknown systematic problem. If all subsample errors are scaled up to $\sigma_i\sqrt{\chi^2/(N-1)}$, the new χ^2 per DOF will automatically be unity. In addition, the statistical error for the weighted average of the subsample estimates

$$\bar{\sigma} \;=\; \frac{1}{\sqrt{\sum_i^N 1/\sigma_i^2}} \tag{A.3}$$

will be increased by the same factor and becomes a *scaled error* ($\tilde{\sigma}$) of:

$$\tilde{\sigma} \;=\; \bar{\sigma}\sqrt{\chi^2/(N-1)} \;=\; \sqrt{\frac{< x^2 > - < x >^2}{N-1}}, \tag{A.4}$$

where we have used the weighted average brackets $< >$ defined in Eq. A.2. Let σ_f be the statistical error returned by the fitter on the unsplit date set. Our procedure is to quote a *split sample* systematic error of

$$\begin{aligned} \sigma_{\rm sys} &= \sqrt{\tilde{\sigma}^2 - \sigma_f^2} \qquad \text{if } \tilde{\sigma} > \sigma_f, \\ \sigma_{\rm sys} &= 0 \qquad\qquad\qquad\; \text{if } \tilde{\sigma} < \sigma_f \end{aligned} \tag{A.5}$$

A.2 Fit Variant Systematics

We now attempt to check if we can extend *split sample* systematics method to cover *fit variant* systematics. The *fit variant* systematics is different from the *split sample* systematics in the three following respects.

i. We assume that the fit variants are all a *priori* likely. We should not use the weighted average implied by Eq. A.2, but rather use a straight average: $< x >= \sum_i^N x_i/N$.

ii. We are not making a combined average of the *fit variants* where each variant is adding independent information. As a result we should remove a factor of $1/\sqrt{N}$ in the $\tilde{\sigma}$ expression. Now we are trying to assess the actual RMS spread in a set of estimators rather than the spread of the mean.

iii. There is no need to subtract the statistical variance from $\tilde{\sigma}^2$, since the fit variations should essentially have fully correlated statistical errors.

Making these modifications, we get

$$\sigma_{\text{sys}} = \sqrt{\frac{\sum_i^N x_i^2 - N < x >^2}{N-1}} \tag{A.6}$$

Eq. A.6 is the expression for the sample standard deviation and differs from the population standard deviation by $N \to N-1$.

Appendix B

Branching Ratio Measurement II

In Chapter 4, we have measured $\Gamma(D_s^+ \to K_S^0 K^+\pi^+\pi^-)/\Gamma(D_s^+ \to K_S^0 K^-\pi^+\pi^+)$. These signal and normalization modes have same decay topology. So we are able to cancel out systematic errors from K_S^0 and track reconstruction efficiencies. We now measure the branching ratios of the D_s^+ with well-known $D_s^+ \to K_S^0 K^+$ decay mode as the normalization mode. This enables us to quote the relative branching ratio of the $D_s^+ \to K_S^0 K^-\pi^+\pi^+$ in addition to $D_s^+ \to K_S^0 K^+\pi^+\pi^-$. Besides, we also measure the relative branching ratio of $\Gamma(D^+ \to K_S^0 K^+)/\Gamma(D^+ \to K_S^0\pi^+\pi^+\pi^-)$ to support D_s^+ measurements.

B.1 $\Gamma(D^+ \to K_S^0 K^+)/\Gamma(D^+ \to K_S^0\pi^+\pi^+\pi^-)$

As mentioned previously, this decay mode has been studied for supporting D_s^+ measurements using normalization mode of $D_s^+ \to K_S^0 K^+$. But it is of good interest to measure the branching ratio itself. Besides, it could be used to extract the isospin amplitudes and phase shifts with $D \to K\pi$ and $D \to KK$ decay modes [37]. In following two D_s^+ measurements, signal modes have $K_S^0 + 3$ *prongs* decay topology and normalization mode $K_S^0 + 1$ *prong*. Although K_S^0 reconstruction efficiency is cancelled out, track reconstruction efficiency is not. In addition we have used different vertexing algorithm for signal and normalization mode as referred in Sec. 4.1. Therefore, if we show $\Gamma(D^+ \to K_S^0 K^+)/\Gamma(D^+ \to K_S^0\pi^+\pi^+\pi^-)$ is consistent with current world average, we could demonstrate our D_s^+ measurements. We have employed same vertexing conditions although we use different vertexing

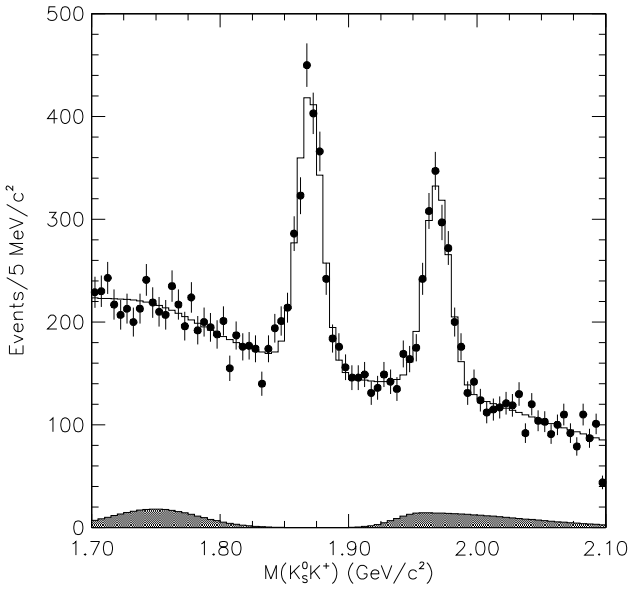

Figure B.1: The invariant mass distribution of $K^0_S K^+$ with D^+ selection cuts. The data are indicated by points with error bars and the solid lines are the fits. The shadowed regions are charm reflection backgrounds.

algorithm from other four-body decay modes to reduce the systematics from cut variants. Fig. B.1 shows the $K^0_S K^+$ final state passing the D^+ selection cuts. Signal is fitted by a Gaussian and background by quadratic polynomial and other charm reflections. From the Monte Carlo study reflection backgrounds on D^+ low mass region come from $D^+_s \to K^{*+} K^0_S$ and $D^+_s \to \overline{K}^{*0} K^+$ due to missing π^0 and D^+ high mass region come from $D^+ \to K^0_S \pi^+$ due to π/K misidentification, as shown in Fig. B.2. The fit returned yields of the $D^+ \to K^0_S K^+$ is 1259$\pm$63. We have investigated $\Lambda^+_c \to K^0_S p$ contamination in the signal region. We have found no evidence in the data for any enhancement due to $\Lambda^+_c \to K^0_S p$ where the p is misidentified as a K (see Fig. B.3). We have also investigated systematics for the $D^+ \to K^0_S K^+$ decay mode with same method used in other decay modes. Fig. B.4 shows relative branching ratios for several cuts and fit variants and split sample. We saw systematic bias from fit variants and estimated error of relative branching ratio is 0.0017.

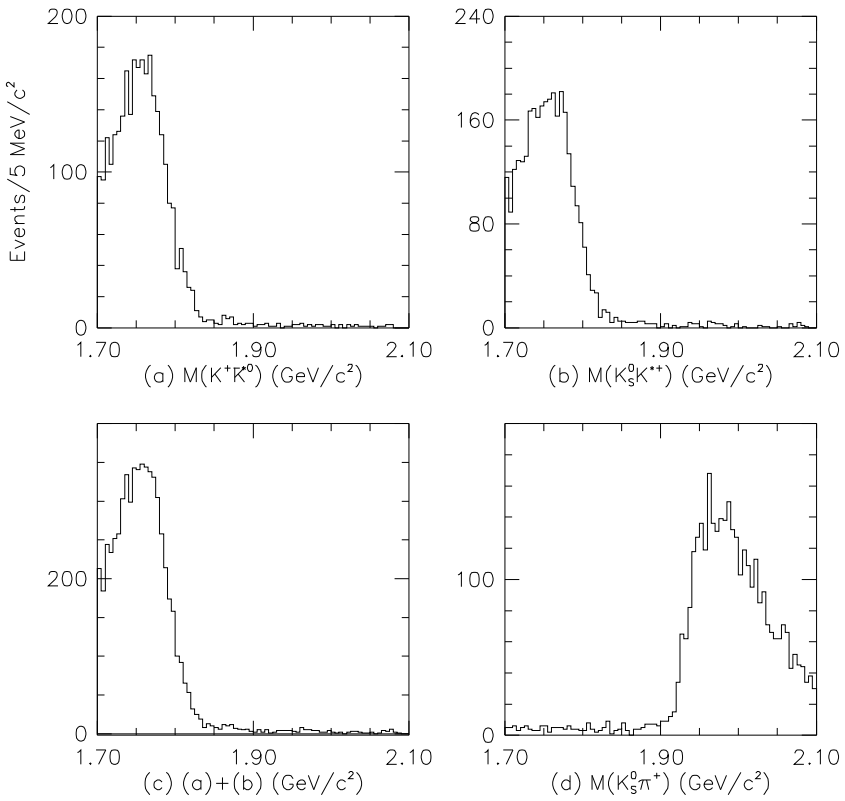

Figure B.2: Charm reflection backgrounds in $K_S^0 K^+$ from Monte Carlo simulation. (a) is from $D_s^+ \to \overline{K}^{*0} K^+$, (b) from $D_s^+ \to K^{*+} K_S^0$, (c) is sum of two reflections and (d) from $D^+ \to K_S^0 \pi^+$.

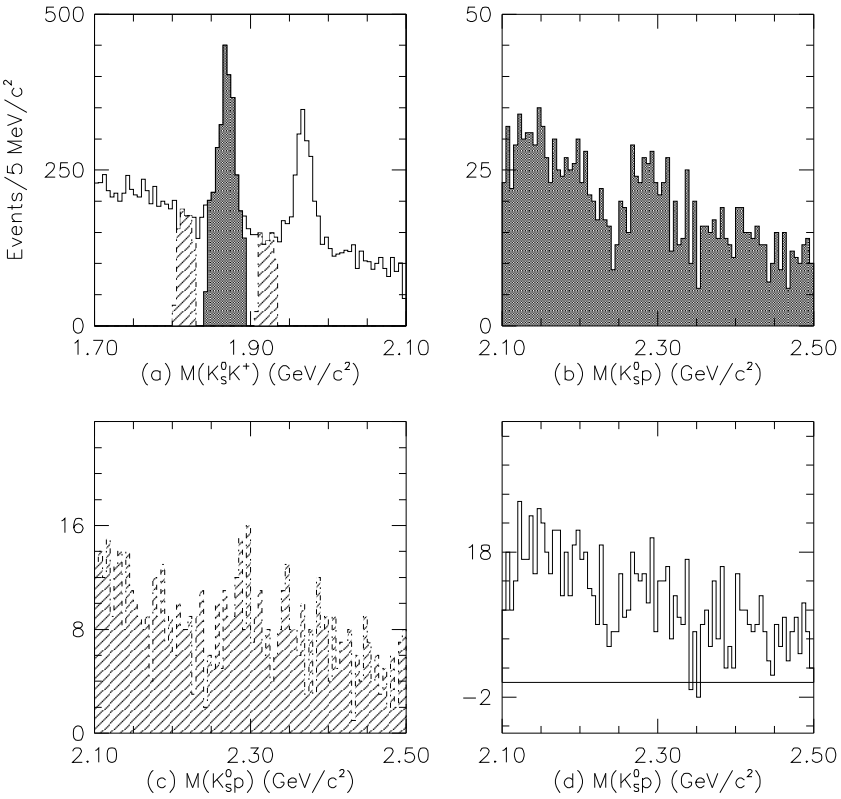

Figure B.3: (a) is $M(K_S^0K^+)$. Shadowed is 2.5σ of signal region and hatched is sideband region. (b) is $M(K_S^0p)$ within $M(K_S^0K^+)$ signal region. (c) is $M(K_S^0p)$ within $M(K_S^0K^+)$ sideband region. (d) is sideband subtracted $M(K_S^0p)$ distribution in the $D^+ \to K_S^0K^+$ signal region.

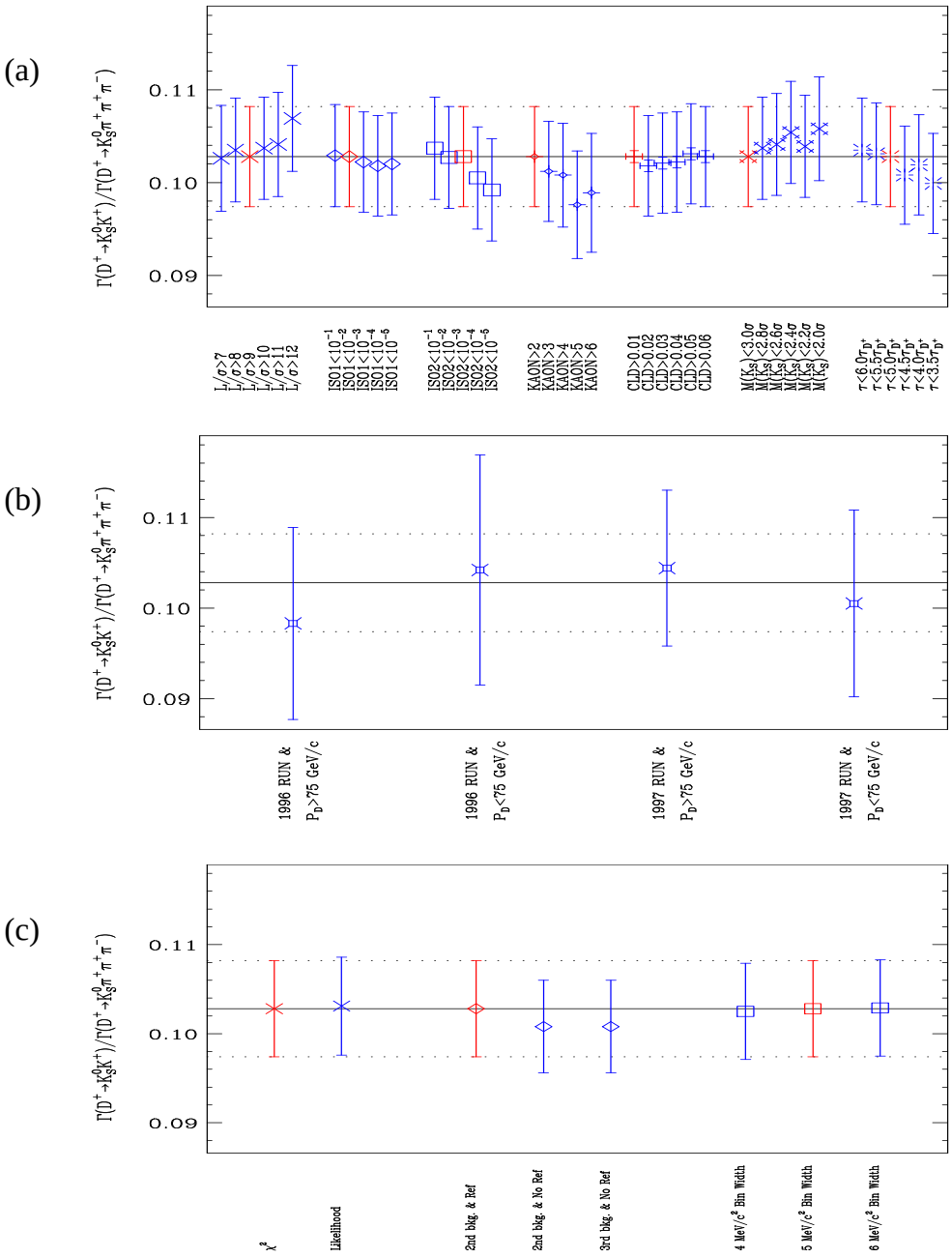

Figure B.4: Systematics for $D^+ \to K^0_S K^+$. (a) is relative branching ratios for cut variants, (b) is relative branching ratios for split sample and (c) is relative branching ratio for fit variants.

Source of error	$\delta_{\Gamma_{\rm rel}}$
$\mathcal{E}$ from resonant state	0.
$\mathcal{E}$ from MC statistics	0.0008
Cut variants	0.
Split sample	0.
Fit variants	0.0017
Total	0.0019

Table B.1: Summary of systematic errors for the $\Gamma(D^+ \to K^0_S K^+)/\Gamma(D^+ \to K^0_S \pi^+\pi^+\pi^-)$.

Finally, we determined our final result of the relative branching ratio of $\Gamma(D^+ \to K^0_S K^+)/\Gamma(D^+ \to K^0_S \pi^+\pi^+\pi^-)$ to be:

$$\frac{\Gamma(D^+ \to K^0_S K^+)}{\Gamma(D^+ \to K^0_S \pi^+\pi^+\pi^-)} \;=\; 0.1042 \pm 0.0053 \pm 0.0019 \tag{B.1}$$

and summarized systematic contributions in Table B.1. Assuming Eq. B.2

$$\Gamma(D \to K^0 \;+\; X) \;=\; 2 \cdot \Gamma(D \to K^0_S \;+\; X) \tag{B.2}$$

and using current world average of $\Gamma(D^+ \to \overline{K}^0 \pi^+\pi^+\pi^-) = (7.0 \pm 0.9)\%$ [1], our measurement of the $D^+ \to K^0_S K^+$ to be:

$$\Gamma(D^+ \to \overline{K}^0 K^+) \;=\; (7.3 \pm 1.0) \times 10^{-3} \tag{B.3}$$

where the error is combined error from PDGs error and our total error. Our measurement for $D^+ \to K^0_S K^+$ is consistent with current world average. More precise measurement for this decay mode utilizing other well-known normalization modes such as $D^+ \to K^0_S \pi^+$ and $D^+ \to K^-\pi^+\pi^+$ is under investigation by our experiment currently [38] and is expected to be published soon.

B.2 $\Gamma(D_s^+ \to K_S^0 K^- \pi^+ \pi^+)/\Gamma(D_s^+ \to K_S^0 K^+)$

To measure this relative branching ratio, we investigated decay mode of $D_s^+ \to K_S^0 K^+$. With slightly different cuts with $D^+ \to K_S^0 K^+$ (see Sec. 4.2), we have obtained this final state as shown in Fig. B.5. The signal is fitted by a Gaussian and background by quadratic polynomial and other charm reflections. Fig. B.6 shows reflection backgrounds on low mass region come from $D_s \to K^* K$ owing to missing π^0. In addition there is significant background from $D^+ \to K_S^0 \pi^+$ caused by misidentification of π to K. This background is not crucial in case of the $D^+ \to K_S^0 K^+$ since this background is out of D^+ signal region, but in $D_s^+ \to K_S^0 K^+$ signal region. From Monte Carlo simulation, we have obtained this background shape and incorporated it to background fit function. The amplitude for charm reflections is a free fit parameter. We have obtained yields of the $D_s^+ \to K_S^0 K^+$ is 1119 ± 59. We investigated $\Lambda_c^+ \to K_S^0 p$ contamination in the signal region. We have found no evidence in the data for any enhancement due to $\Lambda_c^+ \to K_S^0 p$ where the p is misidentified as the K as shown in Fig. B.7.

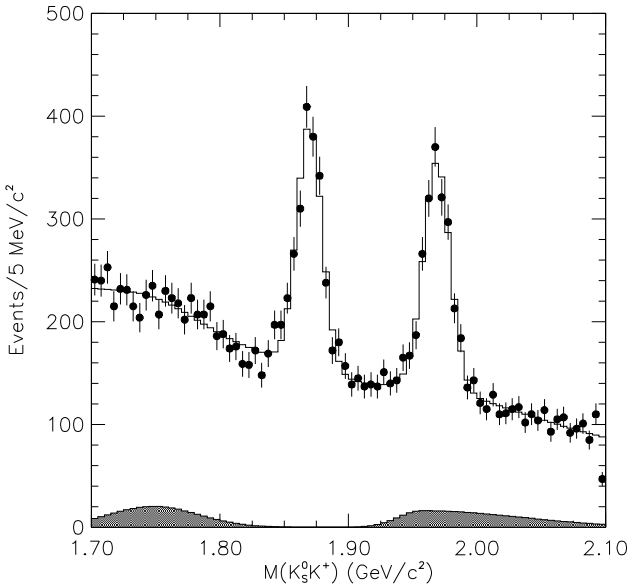

Figure B.5: The invariant mass distribution of $K_S^0 K^+$ with D_s^+ selection cuts. The data are indicated by points with error bars and the solid lines are the fits. The shadowed regions are charm reflection backgrounds.

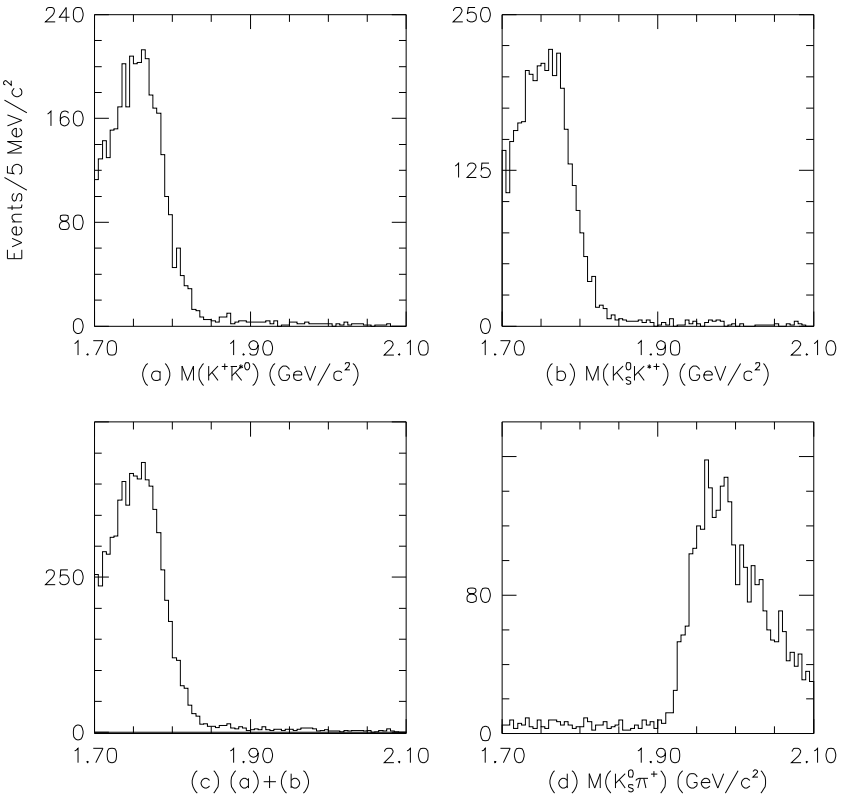

Figure B.6: Charm reflection backgrounds in $K_S^0 K^+$ from Monte Carlo simulation. (a) is from $D_s^+ \to \overline{K}^{*0} K^+$, (b) from $D_s^+ \to K^{*+} K_S^0$, (c) is sum of two reflections and (d) from $D^+ \to K_S^0 \pi^+$.

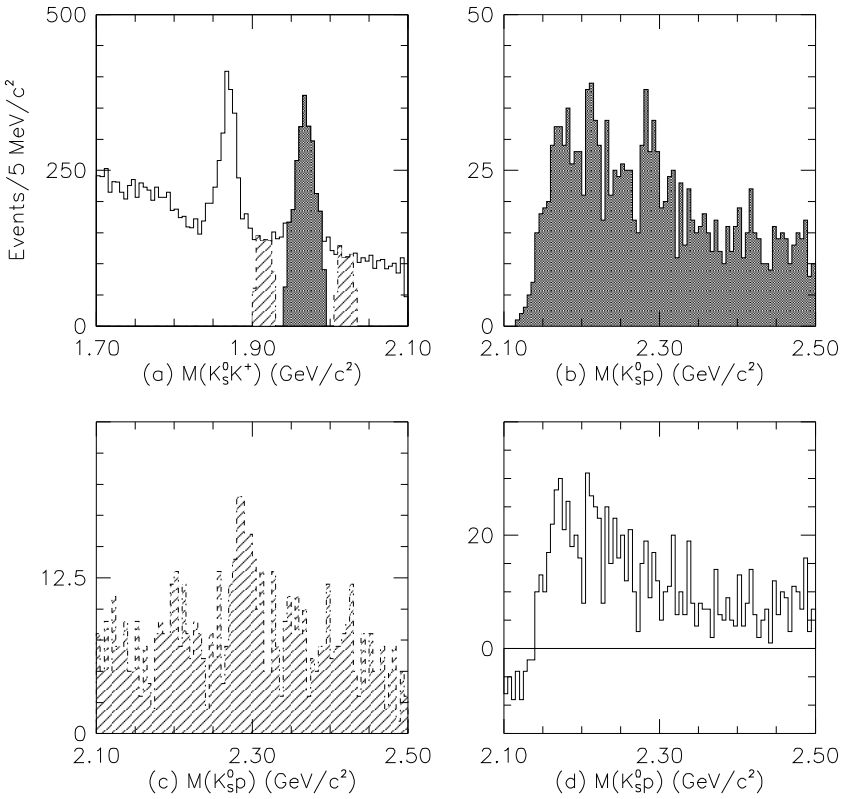

Figure B.7: (a) is $M(K_S^0 K^+)$. Shadowed is 2.5σ of signal region and hatched is sideband region. (b) is $M(K_S^0 p)$ within $M(K_S^0 K^+)$ signal region. (c) is $M(K_S^0 p)$ within $M(K_S^0 K^+)$ sideband region. (d) is sideband subtracted $M(K_S^0 p)$ distribution in the $D^+ \to K_S^0 K^+$ signal region.

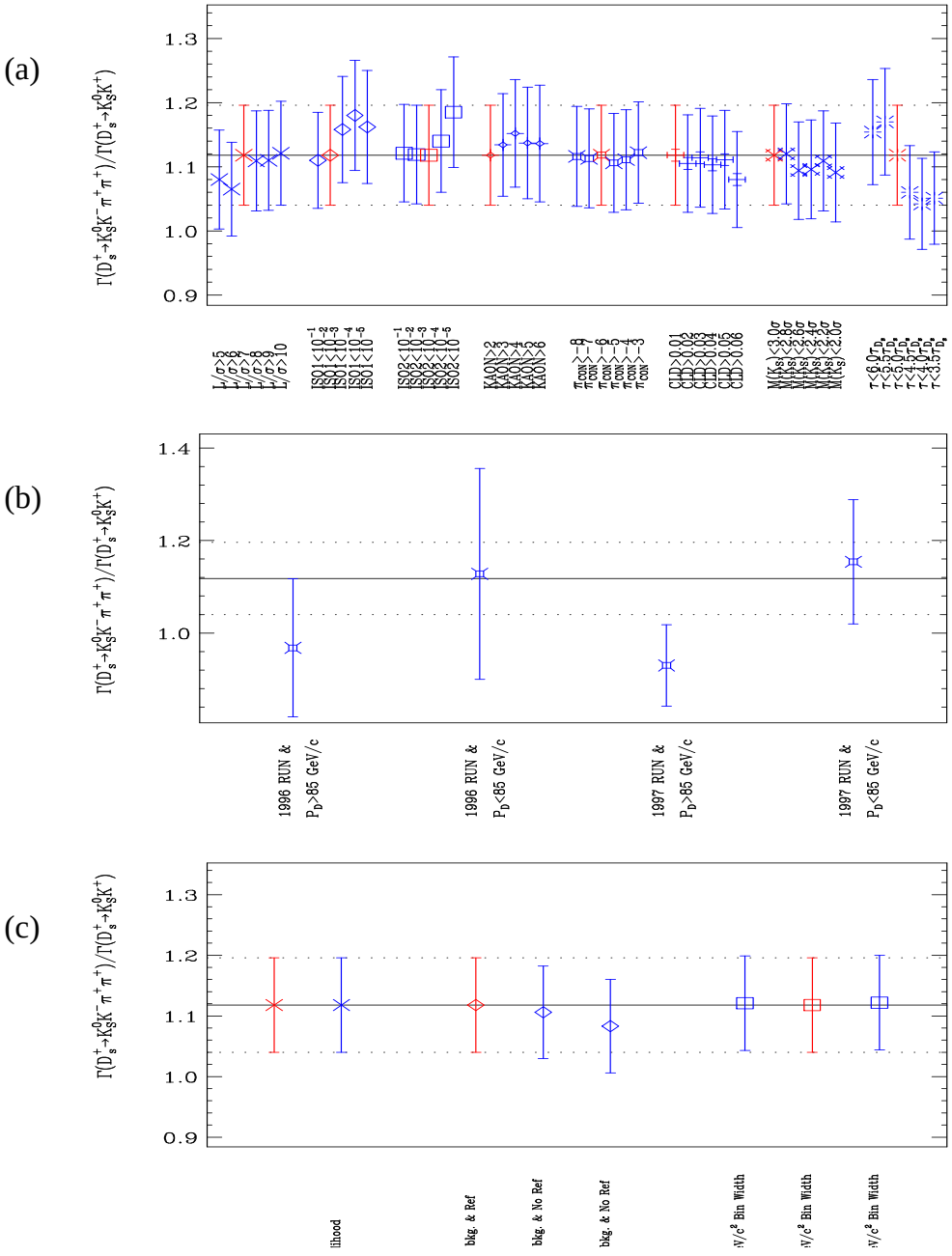

Figure B.8: Systematics for $D_s^+ \to K_S^0 K^- \pi^+ \pi^+$. (a) is relative branching ratios for cut variants, (b) is relative branching ratios for split sample and (c) is relative branching ratio for fit variants.

Source of error	$\delta_{\Gamma_{\rm rel}}$
$\mathcal{E}$ from resonant state	0.051
$\mathcal{E}$ from MC statistics	0.013
Cut variants	0.
Split sample	0.
Fit variants	0.013
Total	0.054

Table B.2: Summary of systematic errors for the $\Gamma(D_s^+ \to K_S^0 K^- \pi^+ \pi^+)/\Gamma(D_s^+ \to K_S^0 K^+)$.

We have investigated systematics for this relative branching ratio of $\Gamma(D_s^+ \to K_S^0 K^- \pi^+ \pi^+)/\Gamma(D_s^+ \to K_S^0 K^+)$ with same method used in other decay modes. Fig. B.8 shows relative branching ratios for several cuts and fit variants and split sample. We notice systematic biased from fit variants and estimated error of relative branching ratio is found to be 0.0008. Finally, we determined our final result of the relative branching ratio of $\Gamma(D_s^+ \to K_S^0 K^- \pi^+ \pi^+)/\Gamma(D_s^+ \to K_S^0 K^+)$ to be:

$$\frac{\Gamma(D_s^+ \to K_S^0 K^- \pi^+ \pi^+)}{\Gamma(D_s^+ \to K_S^0 K^+)} \;=\; 1.118 \pm 0.078 \pm 0.054 \tag{B.4}$$

and summarized systematic contributions in Table B.2. Assuming Eq. B.2 and using current world average of $\Gamma(D_s^+ \to \overline{K}^0 K^+) = (3.6 \pm 1.1)\%$ [1], we have measured the $D_s^+ \to K_S^0 K^- \pi^+ \pi^+$ to be:

$$\Gamma(D_s^+ \to K^0 K^- \pi^+ \pi^+) \;=\; (4.0 \pm 1.3)\% \tag{B.5}$$

where the error is combined error from PDGs error and our total error. Our measurement for $D_s^+ \to K_S^0 K^- \pi^+ \pi^+$ is consistent with current world average and supersede it.

B.3 $\Gamma(D_s^+ \to K_S^0 K^+\pi^+\pi^-)/\Gamma(D_s^+ \to K_S^0 K^+)$

We investigated systematics for this relative branching ratio. Fig. B.9 shows relative branching ratios for several cuts and fit variants and split sample. We saw systematic bias from fit variants and estimated error of relative branching ratio is 0.0008. Finally, we determined our final result of the relative branching ratio of $\Gamma(D_s^+ \to K_S^0 K^+\pi^+\pi^-)/\Gamma(D_s^+ \to K_S^0 K^+)$ to be:

$$\frac{\Gamma(D_s^+ \to K_S^0 K^+\pi^+\pi^-)}{\Gamma(D_s^+ \to K_S^0 K^+)} \;=\; 0.655 \pm 0.060 \pm 0.036 \tag{B.6}$$

and summarized systematic contributions in Table B.3. Assuming Eq. B.2 and using current world average of $\Gamma(D_s^+ \to \overline{K}^0 K^+) = (3.6\pm1.1)\%$ [1], our measurement of the $D_s^+ \to K_S^0 K^-\pi^+\pi^+$ to be:

$$\Gamma(D_s^+ \to \overline{K}^0 K^+\pi^+\pi^-) \;=\; (2.4 \pm 0.8)\% \tag{B.7}$$

where the error is combined error from PDGs error and our total error.

Source of error	$\delta_{\Gamma_{\rm rel}}$
$\mathcal{E}$ from resonant state	0.030
$\mathcal{E}$ from MC statistics	0.008
Cut variants	0.
Split sample	0.
Fit variants	0.019
Total	0.036

Table B.3: Summary of systematic errors for the $\Gamma(D_s^+ \to K_S^0 K^+\pi^+\pi^-)/\Gamma(D_s^+ \to K_S^0 K^+)$.

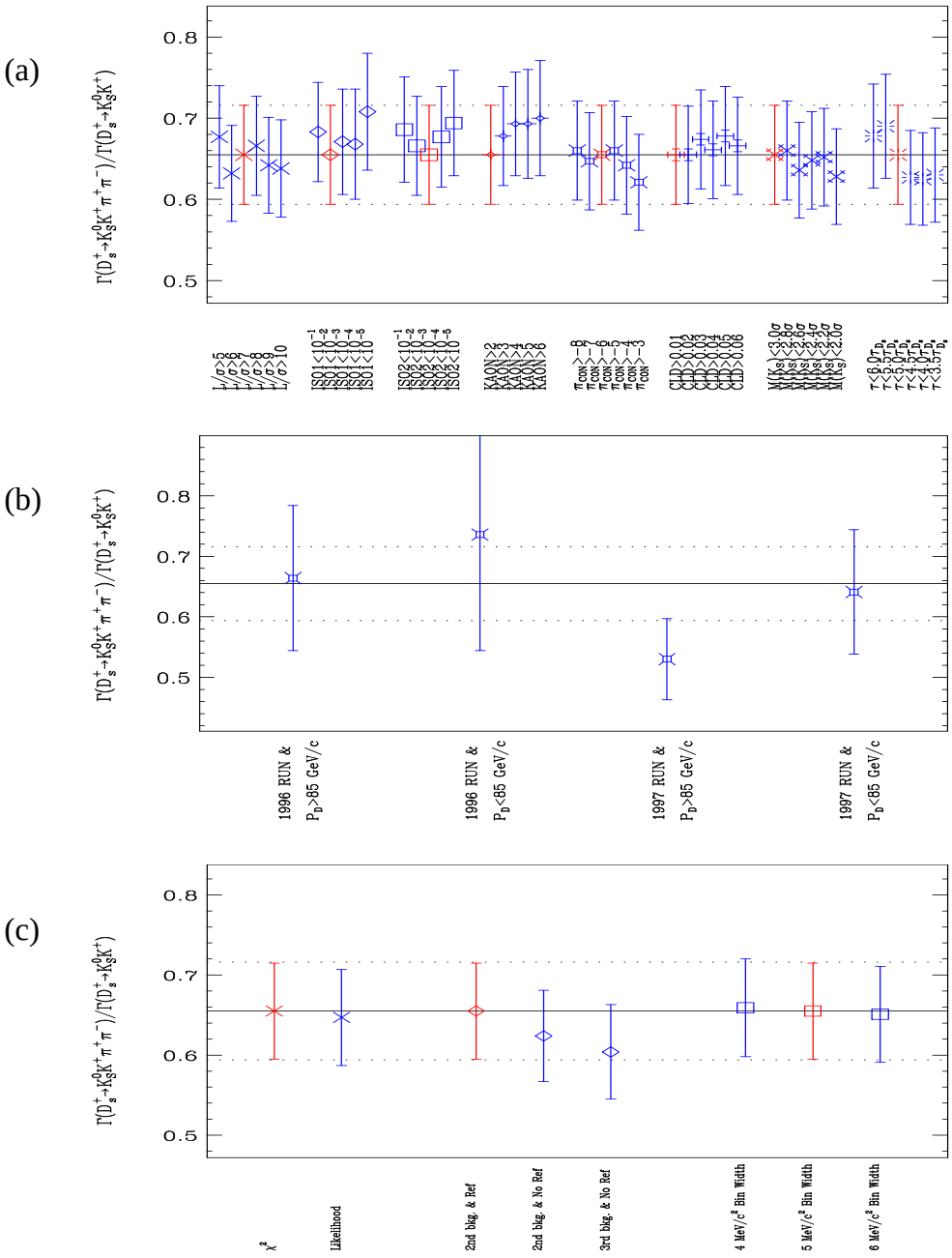

Figure B.9: Systematics for $D_s^+ \to K_S^0 K^+\pi^+\pi^-$. (a) is relative branching ratios for cut variants, (b) is relative branching ratios for split sample and (c) is relative branching ratio for fit variants.

B.4 Summary and Results

We summarize our final results in Table B.4. We quote the relative efficiency for each decay mode instead its absolute efficiency as in the Chapter 5. We calculate absolute branching ratios for these decay modes with current world average and compare our measurements with previous measurements in Table B.5.

Decay Mode	$\mathcal{N}_{\rm signal}$	$\mathcal{E}_{\rm rel}$	$\Gamma_{\rm rel}$
$D^+ \to K^0_S K^+$	1259±63	1.042±0.011	0.1042±0.0053±0.0019 †
$D^+ \to K^0_S \pi^+\pi^+\pi^-$	11590±121	1	1
$D^+_s \to K^0_S K^-\pi^+\pi^+$	837±38	0.669±0.010	1.118±0.078±0.054 †
$D^+_s \to K^0_S K^+\pi^+\pi^-$	476±36	0.649±0.010	0.655±0.060±0.036 ‡
$D^+_s \to K^0_S K^+$	1119±59	1	1

Table B.4: Summary of final results. $\mathcal{E}_{\rm rel}$ is the reconstruction efficiency relative to $D^+ \to K^0_S\pi^+\pi^+\pi^-$ for the D^+ modes and $D^+_s \to K^0_S K^+$ for the D^+_s modes, where its error contains Monte Carlo statistical error only. $\Gamma_{\rm rel}$ is the branching ratio relative to $D^+ \to K^0_S\pi^+\pi^+\pi^-$ for the D^+ modes and $D^+_s \to K^0_S K^+$ for the D^+_s modes. Marked mode with † is the new measurement and modes with ‡ are unseen decay modes previously. The errors on the branching ratios are statistical and systematic, respectively.

Branching Ratio	FOCUS	Others
$\Gamma(D^+ \to \overline{K}^0 K^+)$	$(7.3\pm1.0)\times10^{-3}$	$(7.4\pm1.0)\times10^{-3}$ [1]
$\Gamma(D^+_s \to K^0 K^-\pi^+\pi^-)$	(4.0±1.3)%	(4.3±1.5)% (@ 90% C.L.) ‡
$\Gamma(D^+_s \to \overline{K}^0 K^+\pi^+\pi^-)$	(2.4±0.8)%	$<$ 2.8% (@ 90% C.L.) ‡

Table B.5: Comparison with previous measurement. Marked modes with ‡ are measured by the ARGUS collaboration [23]. The error is combined by quadrature with our total error and PDGs error.

Bibliography

[1] Particle Data Group, D.E. Groom *et al.*, *Eur. Phys. J.* **C15**, 1 (2000).

[2] P. W. Higgs, *Phys. Lett.* **12**, 132 (1964).

[3] S. Weinberg, *Phys. Rev. Lett.* **19**, 1264 (1967).

[4] A. Salam, *Elementary Particle Theory*, ed. N. Savaratholm, 367 (1968).

[5] M. Kobayashi and T. Maskawa, *Prog. Theor. Phys.*, **49**, 652 (1973).

[6] F. Halzen and A. D. Martin, *Quark and Leptons*, New York: John Wiley & Sons, (1984).

[7] D. J. Bjorken and S. L. Glashow, *Phys. Lett.* **11**, 255 (1964).

[8] S. L. Glashow, J. Iliopoulos, and L. Maiani, *Phys. Rev.* **D 2**, 1285 (1970).

[9] P. Bloch *et al.*, *Phys. Lett.* **B 56**, 201 (1975);
C. Alliegro *et al.*, *Phys. Rev. Lett.* **68**, 278 (1992);
S. Adler *et al.*, *Phys. Rev. Lett.* **79**, 4756 (1997);
R. Appel *et al.*, *Phys. Rev. Lett.* **83**, 4482 (1999);
H. Ma *et al.*, *Phys. Rev. Lett.* **84**, 2580 (2000);
S. Adler *et al.*, *Phys. Rev. Lett.* **84**, 3768 (2000).

[10] J. J. Aubert *et al.*, *Phys. Rev. Lett.* **33**, 1404 (1974);
J. E. Augustin *et al.*, *Phys. Rev. Lett.* **33**, 1406 (1974).

[11] G. Goldhaber *et al.*, *Phys. Rev. Lett.* **37**, 255 (1976);
I. Peruzzi *et al.*, *Phys. Rev. Lett.* **37**, 569 (1976).

[12] C. E. Carlson and P. G. O. Freud, *Phys. Lett.* **B 39**, 349 (1972).

[13] M. K. Gaillard, B. W. Lee, and J. L. Rosner, *Rev. Mod. Phys.* **47**, 227 (1975).

[14] J. J. Sakurai, *Ann. Rev. Nucl. Part. Sci.* **11**, 1 (1960).

[15] L. M. Jones and H. W. Wyld, *Phys. Rev.* **D 17**, 759 (1978).

[16] J. E. Ramirez *et al.*, (FOCUS Collaboration), **"A High Statistics Measurement of Ξ_c Lifetimes"**, *International Journal of Modern Physics A, DPF 2000 Columbus, OH, U.S.A* (2000);
M. Artuso *et al.*, (CLEO Collaboration) `hep-ex/0107040` (2001);
J. M. Link *et al.*, (FOCUS Collaboration) `hep-ex/0110002` (2001).

[17] B. Guberina, S. Nussinov, R. D. Peccei, and R. Rückl, *Phys. Lett.* **B 89**, 111 (1979).

[18] M. K. Gaillard, B. W. Lee, *Phys. Rev. Lett.* **33**, 108 (1974);
G. Altarelli, L. Maiani, *Phys. Lett.* **B 52**, 351 (1974);
G. Altarelli, G. Corci, G. Martinelli, R. Petrarca, *Nucl. Phys.* **B187**, 461 (1981);
W. Bernreuther, *Z. Phy.* **C 29**, 245 (1985).

[19] M. Bauer, B. Stech, M. Wirbel, *Z. Phy.* **C 29** 637 (1985);
M. Bauer and M. Wirbel, *Z. Phy.* **C 42** 671 (1987);
M. Bauer, B. Stech, M. Wirbel, *Z. Phy.* **C 34** 103 (1987).

[20] E. M. Aitala *et al.*, *Phys. Lett.* **B 421**, 405 (1998);
P. L. Frabetti *et al.*, *Phys. Lett.* **B 321**, 295 (1994);
J. Alexander *et al.*, *Phys. Rev. Lett.* **65**, 1184 (1990).

[21] Thomas E. Browder, Klaus Honscheid and Daniele Pedrini, *Ann. Rev. Nucl. Part. Sci.* **46**, 395 (1997).

[22] S. Barlag *et al.*, *Z. Phy.* **C 48**, 361 (1990).

[23] H. Albrecht *et al.*, *Z. Phy.* **C 53**, 361 (1992).

[24] K. Cho, FOCUS internal memo, `http://utkhep.phys.utk.edu/~khcho/bgm_general.html` (199x).

[25] P. L. Frabetti *et al.*, *Phys. Lett.* **B 407**, 79 (1997).

[26] V. Arena *et al.*, *Nucl. Instru. & Meth.* **A434**, 271 (1999).

[27] A. Kreymer and F. Prelz, DAQ Architecture for E831, FOCUS Internal Memo (1997).

[28] C. Cawlfield, M. Ruesnink and J. Wiss, Muon Identification χ^2 Confidence Levels, FOCUS internal memo (1994).

[29] M. G. Hosack, Confidence Level for Outer Muons, FOCUS internal memo (1998).

[30] J. M. Link *et al.*, accepted for publication in *Nucl. Instru. & Meth.* **A** (2001); FERMILAB-Pub-01/243-E (2001);
J. M. Link *et al.*, (FOCUS Collaboration) `hep-ex/0108011` (2001).

[31] J. M. Link *et al.*, accepted for publication in *Nucl. Instru. & Meth.* **A** (2001); FERMILAB-Pub-01/244-E (2001);
J. M. Link *et al.*, (FOCUS Collaboration) `hep-ex/0109028` (2001).

[32] M. Fausey *et al.*, CPS and CPS Batch Reference Guide, Technical Report GA008, Fermilab (1998).

[33] J. P. Cumalat, Investigation of Kshorts and Arbitration, FOCUS internal memo, (1999).

[34] B. O'Reilly, Decays involving K^0_S, FOCUS internal memo, (1999).

[35] J. M. Link *et al.*, *Phys. Lett.* **B 488**, 218 (2000).

[36] J. M. Link *et al.*, *Phys. Lett.* **B 512**, 277 (2001).

[37] M. Bishai, *et al.*, *Phys. Rev. Lett.* **78**, 3261 (1997).

[38] B. O'Reilly, *et al.*, (FOCUS Collaboration), **"Direct CP violation searches at FOCUS"**, *International Journal of Modern Physics A, DPF 2000 Columbus, OH, U.S.A* (2000);
J. M. Link *et al.*, (FOCUS Collaboration) `hep-ex/0109022` (2001).

[39] I. I. Bigi and H. Yamamoto, *Phys. Lett.* **B 349**, 363 (1995).